Voltage Signalling in the Medial Superior Olive

Alexander R. Callan

Graduate School of
Systemic Neurosciences
LMU Munich

Dissertation der Graduate School of Systemic Neurosciences der
Ludwig-Maximilians-Universität München

7th March, 2019

Supervisor:
Prof. Dr. Christian Leibold
Computational Neuroscience
Department Biology II
Ludwig-Maximilians-Universität München

First Reviewer:	Prof. Dr. Christian Leibold
Second Reviewer:	Prof. Dr. Felix Felmy
External Reviewer:	Prof. Nace Golding

Date of submission:	7^{th} March, 2019
Date of oral defense:	10^{th} September, 2019

Summary

Voltage signalling is essential to neuronal function. Changes in cell membrane potential form the basis of the computations performed by single neurons. Throughout the nervous system, the physiological properties of neurons are adapted to the computations they perform. In sensory systems, neuronal voltage signalling is adapted to the demands of each sensory modality.

In the auditory system, neurons of the medial superior olive (MSO) compare the arrival time of sounds at the two ears. The difference in these arrival times, the interaural time difference (ITD), indicates the direction a sound is coming from. Utilising ITDs, which are only tens to hundreds of microseconds in duration, is a significant challenge for neurons. Nevertheless, animals are capable of differentiating sound sources which differ in their ITDs by only tens of microseconds. In order for animals to achieve such feats, MSO neurons are adapted for rapid membrane voltage signalling. Understanding the mechanisms that allow MSO neurons to compute ITDs was the aim of this thesis.

An essential property that shapes membrane voltage signalling is a neuron's complement of voltage-gated ion channels. Previous studies of the MSO have demonstrated the critical importance of low-threshold potassium channels. Here we show using immunohistochemistry that the complement of potassium channels in MSO neurons is richer than previously thought and includes voltage-gated potassium channel sub-units from several sub-families. Whole cell voltage clamp recordings, combined with pharmacology, support the presence of a variety of potassium channel sub-types, including high-threshold channels. Voltage and current clamp recordings suggest that these channels are, in fact, partially open at resting potential, and contribute to setting the passive properties of MSO neurons. Computational modelling using the measured potassium channel parameters suggests that a trade-off

between low- and high-threshold channels might contribute to setting the membrane electrophysiology of MSO neurons. By affecting the amplitude and timing of EPSPs, the balance of low- and high-threshold potassium channels can also influence ITD computation in MSO neurons.

Another essential component of neuronal computation is integration of excitatory postsynaptic potentials (EPSPs). MSO neurons receive excitatory synaptic innervation from both cochlear nuclei, which forms the basis of ITD detection. The location of excitatory synapses determines the extent of EPSP overlap at the soma, as each EPSP needs time to propagate to the soma from its dendritic site of initiation. Using anatomical techniques, we show that excitatory axons innervating MSO neurons tend to form large, distributed synapses along dendrites, but with terminal boutons clustered close to the soma. EPSPs that are initiated simultaneously by different input fibres are therefore likely to arrive at the soma at similar times. Computational modelling suggests that distributing synaptic conductance along a length of dendrite results in larger, but also faster somatic EPSPs. Distributed synapses in the model produced different ITD response curves to localised synapses, indicating they may also be relevant to ITD computation.

Both high-threshold potassium channels and distributed excitatory synapses affect synaptic integration and the response of MSO neurons to bilateral inputs. These properties represent ways this system is optimised for precise voltage signalling in order to perform ITD computation with microsecond precision.

Contents

Chapter 1

Introduction

Voltage signalling is essential to nervous system function. Changes in cell membrane potential form the basis of the computations performed by single neurons and the networks they constitute. Voltage signalling occurs at different levels in the nervous system. At electrical synapses, neurons can communicate using direct electrical contact to other neurons. Alternatively, a chemical signal from one neuron can initiate a voltage response in a second neuron via a chemical synapse. Voltage signals can propagate throughout individual cells, allowing neurons to integrate signals from multiple sources, and perhaps pass on information to other neurons by way of an action potential. Additionally, signals from outside the nervous system are converted to changes in the membrane potential of sensory cells, which then pass on sensory information to the brain.

In the auditory system, for example, mechanical oscillations are converted to voltage signals in the cochlea. Rapid changes in air pressure (i.e. sound waves) induce oscillations of the tympanic membrane. The movement of the tympanic membrane sets the middle ear bones into motion, and they pass on the oscillations to the fluid filled cochlea via the oval window. The pressure waves in the fluid of the cochlea cause the basilar membrane to oscillate. The primary sensory cells of the auditory system, the inner hair cells, are located on the basilar membrane and they transduce these mechanical oscillations to changes in membrane potential. These sensory cells relay the signal to neurons in the auditory pathway of the brain where, after many stages of processing, they are ultimately interpreted as sound. The neurons that receive direct input from the cochlea carry information concerning the intensity, frequency and

timing of sounds. By processing these features of sound stimuli, the central auditory system is able to construct detailed and dynamic acoustic scenery. Reconstructing the acoustic environment places particular demands on the neurons involved, which have therefore developed characteristic properties to optimise their voltage signalling and therefore their ability to interpret acoustic information.

One important feature of any sound in the acoustic environment is that it has an origin. In other words, the sound source has a particular location in space. The signals transduced by the cochlea provide only incomplete information about sound source location. In order to accurately determine the origin of a sound, central auditory neurons are therefore required to compute the location based on the limited information available to them.

Cues for sound source location are computed early in the auditory system, in the auditory brainstem. In mammals, one brainstem nucleus that plays an important role in sound source localisation is the Medial Superior Olive (MSO). The MSO utilises timing information contained in auditory signals to fulfil this role. Relevant timing information in auditory signals can vary on scales as low as tens of microseconds. Utilising this information therefore represents a significant challenge to neurons, which can typically be expected to vary their membrane potentials over time periods of hundreds of microseconds to several milliseconds. The neurons of the MSO therefore possess many specific adaptations to optimise the speed and precise timing of membrane signalling. In this thesis I will present results pertaining to voltage signalling in the MSO. To contextualise the results described in subsequent chapters, I will first describe how mammals localise sound sources. I will follow by describing the position of the MSO in the ascending auditory pathway and how it responds to auditory stimuli. Finally, I will describe the anatomical and physiological specialisations that allow MSO neurons to process auditory information with remarkable speed and precision.

1.1 Sound localisation

For most people, it is natural to identify the location in space from which a sound originates. But the auditory system does not directly sense the location of a sound source. It must be computed based on the information provided to the brain by the cochlea. The brain makes use of several cues in parallel

to determine the vertical and horizontal positions of a sound source (Grothe et al., 2010). In the vertical plane, the brain uses spectral cues to determine elevation and whether a sound is originating in front of or behind the listener. In the horizontal plane, the brain can utilise two distinct cues: interaural level differences and interaural time difference (see Figure 1.1).

Spectral cues in a sound stimulus are available thanks to the asymmetry of the outer ear. Sound waves reflect from the pinna resulting in frequency dependent resonance and interference (Musicant et al., 1990; Rice et al., 1992). The frequency specific changes in the energy of the sound stimulus across its spectrum are known as the head related transfer function. This function varies systematically depending on the angle of incidence of the incoming sound, and therefore on the position of the sound source. The spectral density of the sound can therefore provide information to the nervous system about the origin of a sound source in space (Oertel and Young, 2004). Spectral cues are monaural and are thus particularly useful for locating sound sources in the vertical plane, along which binaural cues provide no information.

Interaural level differences (ILDs) arise when a sound is attenuated by the head of the listener (Rayleigh, 1907). This head shadowing effect results in a reduced intensity of the sound at the ear farthest from the sound source. The relative sound level between the ears varies systematically with the horizontal position of the sound source; the minimum difference will be from sound sources directly in front of the listener, and the maximum will be induced by sound sources at 90° along the azimuth. Neural circuits in the brainstem are able to compare the sound level at each ear and thereby encode the horizontal position of the sound source (Grothe, 2000).

The utility of ILDs decreases as the frequency of the sound decreases. When the sound has a wavelength equal to or greater than the width of the listener's head, the sound waves can bend around the head, and no intensity reduction will occur (Rayleigh, 1907). At these lower frequencies, the brain can instead utilise interaural time differences (ITDs), the time it takes for sounds to travel from one ear to the other. Although ITDs allow a listener to localise the source of lower frequency sounds, they present a particular challenge for the nervous system on account of their brevity. ITDs are on the order of tens to hundreds of microseconds, orders of magnitude shorter than the one to two millisecond action potentials neurons use to encode information. The maximum possible ITD depends on the head size of the animal. For humans

this is up to about ±700 μs (Benichoux et al., 2016), while it can be as brief as ±120 μs for small rodents like Mongolian gerbils (Maki and Furukawa, 2005). Nevertheless, due to neuronal specialisations for rapid signal processing, both humans and some small rodents are capable of utilising ITDs in sound source localisation.

In the mammalian brain, the MSO contains neurons that are sensitive to ITDs. Neurons in this nucleus have evolved particular adaptations in their cellular and network properties to allow for sensitivity to these extremely rapid signals. MSO neurons exhibit systematically varying action potential output across the range of naturally occurring ITDs. The current knowledge of how they achieve this feat will be summarised in subsequent sections.

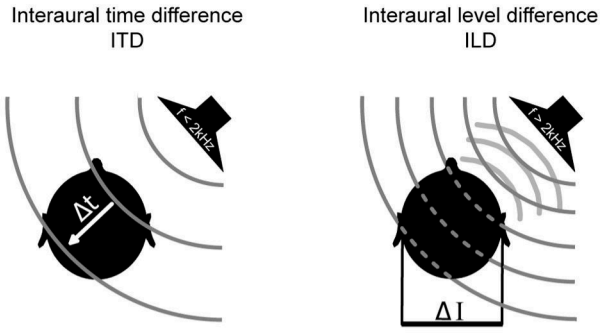

Figure 1.1: The two binaural cues used for sound localisation. **A.** Interaural time differences (ITDs) are effective for lower frequencies (e.g. <2 KHz). **B.** Interaural level differences (ILDs) are effective for higher frequencies (e.g. >2 KHz. The transition point depends on the size of the animal's head. Reproduced from Figure 2 of Grothe and Pecka (2014) in accordance with the Creative Commons Attribution License (CC BY).

1.2 Mongolian gerbils in hearing research

Before continuing with more details about the MSO, it important to clarify which MSO I will be describing. The MSO has been identified in most mammalian species investigated (Nothwang, 2016) but its function varies between species (Grothe, 2000). ITD sensitivity has been observed in MSO neurons of many species, including dogs (Goldberg and Brown, 1969), cats (Yin and Chan, 1990), and Mongolian gerbils (Spitzer and Semple, 1995).

Mongolian gerbils (*Meriones unguiculatus*) were used for all experiments described in this thesis. Additionally, computational modelling was based on data from experiments on gerbils. These rodents possess many qualities that make them ideal for hearing research.

The main advantage of Mongolian gerbils for studies of sound localisation is the extension of their hearing range into lower frequencies. Good low frequency hearing is not typical for mammals of this size. The natural habitat of Mongolian gerbils is the open and arid environments of Mongolia and surrouding areas (Lay, 1972). In such an environment, low frequency sounds travel well and can be important auditory cues for animals. Similar adaptations to low frequency hearing also arose independently in desert dwelling animals of North America, such as the kangaroo rat (Webster and Plassman, 1992). Their sensitivity to lower sound frequencies means gerbils can use ITDs as a cue for sound localisation. Gerbils therefore possess large, distinct MSOs, whose cells are highly sensitive to variations in ITDs. An MSO can be found in other small mammals, such as bats and mice, but in these animals it is involved in other aspects of auditory processing (Grothe, 2000; Fischl et al., 2016). Given the prominence and established function of the MSO in gerbils, this species is an ideal choice for studying how these neurons are specialised for their particular function.

In the following, I will refer to studies of the MSO in several different species. Where the species is not noted, the results are from studies of the Mongolian gerbil.

1.3 MSO in sound localisation

1.3.1 Circuit anatomy

The MSO is located in the brainstem and receives direct excitatory synaptic input and indirect inhibitory synaptic input from both cochlear nuclei (cat, Stotler, 1953; Cant and Hyson, 1992). It is one of the first stages in the auditory brainstem to receive binaural input, and the earliest stage of the auditory system that is sensitive to ITDs. A diagrammatic outline of the MSO circuit is shown in Figure 1.2. In the auditory system, sound stimuli are first transduced to neural signals by inner hair cells of the cochlea, which form synapses with neurons of the spiral ganglion located within the modiolus, the bony centre of the cochlea. The axons of the spinal ganglion neurons form the

auditory nerve, part of the eighth cranial nerve, which projects to the cochlear nucleus. The cochlear nucleus contains many types of neurons with different projection patterns (Cant and Benson, 2003) and intrinsic properties (Oertel, 1991). The most important for the MSO are the spherical bushy cells and the globular bushy cells, both of which are glutamatergic.

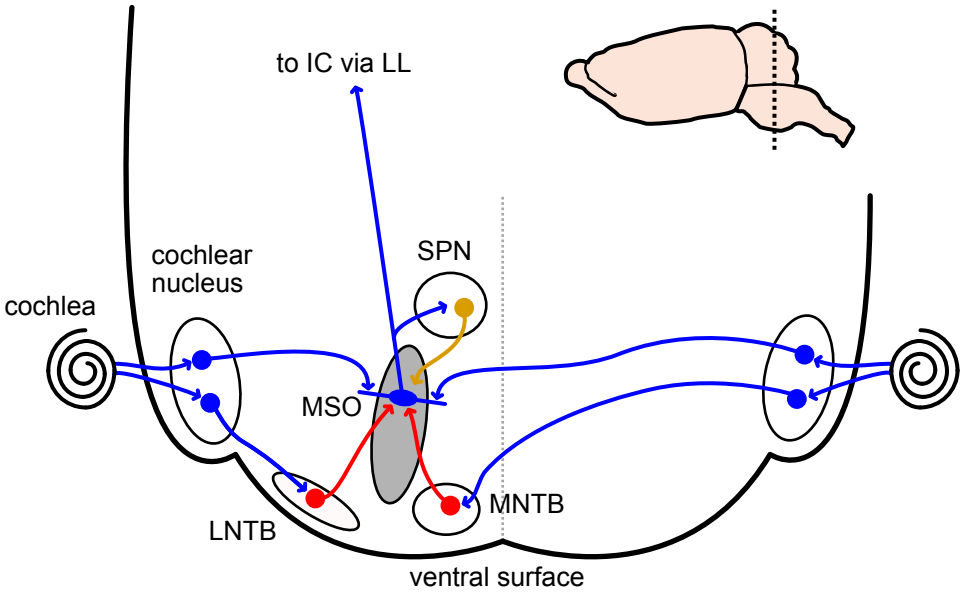

Figure 1.2: Axonal projections to and from the MSO, which is shown in grey, in the brainstem. MSO = medial superior olive, LNTB = lateral nucleus of the trapezoid body, MNTB = medial nucleus of the trapezoid body, SPN = superior periolivary nucleus, IC = inferior colliculus, LL = lateral lemniscus. Blue = glutamatergic projections, red = glycinergic projections, yellow = GABAergic projections. Inset: schematic of gerbil brain (lateral view) showing approximate location of section in main figure.

The spherical bushy cells provide excitatory input to the MSO, which is targetted to particular parts of the MSO neuron. A typical MSO neuron possesses two dendritic trees emerging from opposite poles of the cell soma (see Figure 1.3), one directed laterally and one directed medially towards the midline (Rautenberg et al., 2009). Excitatory synaptic inputs can be found on both dendritic trees and on the soma (Couchman et al., 2012), however they are most often segregated to just the dendritic tree nearest the input source (cat, Stotler, 1953). Therefore, excitatory inputs from the ipsilateral

cochlear nucleus target the lateral dendrites, while excitatory inputs from the contralateral cochlear nucleus target the medial dendrites.

In contrast to excitatory input, inhibitory input primarily targets the somata of MSO neurons (Kapfer et al., 2002; Couchman et al., 2012). The inhibitory pathway involves one more synapse than the excitatory pathway. In contrast to the spherical bushy cells, the globular bushy cells of the cochlear nucleus project to the ipsilateral lateral nucleus of the trapezoid body (LNTB), and to the contralateral medial nucleus of the trapezoid body (MNTB; Smith et al., 1991). Each of these nuclei make inhibitory, glycinergic projections to the MSO on the same side (Cant and Hyson, 1992; Kuwabara and Zook, 1992). Since the MNTB receives contralateral input, the MSO receives inhibitory inputs driven by each cochlear nucleus. Both sources of glycinergic input are targetted to cell somata.

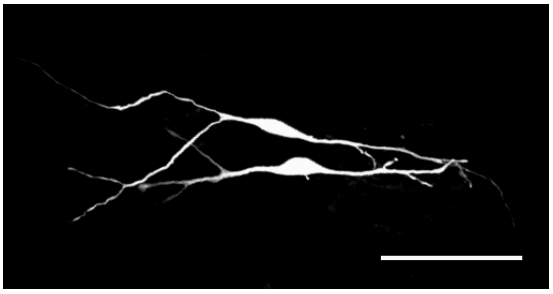

Figure 1.3: Two MSO neurons exhibiting characteristic bipolar morphology. Neurons were filled with fluorescent dye during patch clamp recording and imaged with a confocal microscope. Scale bar = 100 μm.

In addition to excitatory and inhibitory synaptic inputs, the MSO receives modulatory inputs. One of these is a feedback loop via the adjacent superior paraolivary nucleus (SPN). MSO neurons form excitatory synapses on GABAergic neurons in the SPN, which in turn send projections back to the MSO (Stange et al., 2013). These GABAergic projections appear to act on presynaptic terminals in the MSO nucleus via volume transmission, and cause a shift in the ITD response curve of MSO neurons (described in more detail below). Additionally, there are serotonergic inputs that modulate spike probability via hyperpolarisation-activated, cyclic nucelotide-gated (HCN) channels at the axon initial segment (Ko et al., 2016), although the precise role of these inputs in sound localisation is unclear.

MSO neurons themselves are glutamatergic and send excitatory projections to subsequent stations in the ascending auditory system. Axons from MSO neurons form part of the brainstem fibre bundle known as the lateral lemniscus (Glendenning et al., 1981). These axons terminate in the dorsal nucleus of the lateral lemniscus (DNLL; Glendenning et al., 1981) and in the inferior colliculus of the midbrain (Cant, 2013). Each MSO projects primarily to the ipsilateral DNLL, but there is also evidence for projections to the contralateral DNLL (Siveke et al., 2006). Neurons sensitive to ITDs can be found in both the DNLL (Siveke et al., 2006) and the inferior colliculus (cat, Rose et al., 1966; guinea pig, McAlpine et al., 1998). The response profiles of these neurons suggest that they inherit their ITD sensitivity from their MSO afferents—from one MSO neuron in the case of the DNLL, and from multiple convergent inputs in the case of the inferior colliculus (guinea pig, McAlpine et al., 2001).

1.3.2 ITD sensitivity of MSO neurons

The MSO is the earliest stage of the ascending auditory system that is sensitive to ITDs. Neurons in the MSO show clear modulation of their action potential firing rate in response to changing ITDs (dog, Goldberg and Brown, 1969; cat, Yin and Chan, 1990; gerbil, Spitzer and Semple, 1995; Brand et al., 2002). MSO neurons therefore generate a neural code for the ITD of a sound stimulus, which is passed on to subsequent stations in the auditory system and used for localising low frequency sound sources (Stecker and Middlebrooks, 2003).

Neurons in the MSO code for ITDs by varying spike output over a broad range of ITDs (Figure 1.4). Gradual changes in spiking output across the physiological range of ITDs has been observed in the MSO of the gerbil (Brand et al., 2002; Pecka et al., 2008) and the inferior colliculus of the gerbil (Lesica et al., 2010) and the guinea pig (McAlpine et al., 2001). In the MSO, neuronal ITD response functions typically peak for sounds that lead at the contralateral ear. This observation has been made in dogs (Goldberg and Brown, 1969), cats (Yin and Chan, 1990), and gerbils (Brand et al., 2002; Pecka et al., 2008; van der Heijden et al., 2013). In recordings from gerbil, the peak of the ITD function—the "best ITD"—often lies outside of the physiological range. This strongly suggests that the slope of the function, rather than the peak, is most important for ITD coding in the MSO.

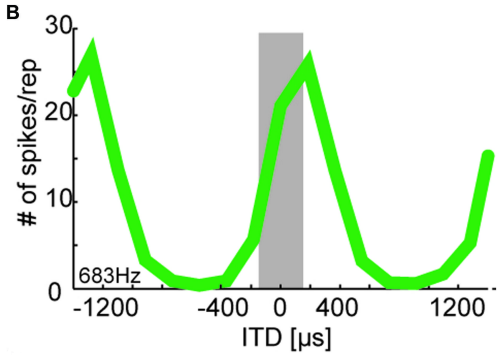

Figure 1.4: Action potential output of a gerbil MSO neuron in response to bilateral pure tone sound stimuli (683 Hz) with varying ITDs. The grey bar represents the physiologically relevant range of ITDs for a gerbil. Reproduced from figure 6 of Grothe and Pecka (2014) in accordance with the Creative Commons Attribution License (CC BY).

Although MSO neurons favour contralaterally leading sounds, their best ITDs also vary systematically with best frequency (the frequency of sound stimuli eliciting the greatest action potential output from a neuron). The MSO is arranged tonotopically, with neuronal best frequencies increasing along the dorsoventral axis (Franken et al., 2015). Best ITDs tend to be larger (i.e. at more contralaterally leading stimuli) for lower frequency neurons, and smaller (i.e. closer to zero ITD) for higher frequency neurons (gerbil, Brand et al., 2002; guinea pig inferior colliculus, McAlpine et al., 2001). Additionally, even within single neurons, the best ITD varies depending on the frequency of the stimulus (Pecka et al., 2008). Nevertheless, the best ITDs are almost exclusively contralaterally leading, and a large proportion occur outside the physiological range.

The preference of MSO neurons for certain best ITDs indicates that different ITD detection strategies are used by mammals and birds (Grothe et al., 2010). Bird possess an analogous structure to the mammalian MSO, the nucleus laminaris, in which individual neurons are tuned to a relatively narrow range of ITDs. These neurons show a sharp peak in spike rate at a particular ITD (the “best ITD”), which varies across the population. The action potential output of individual neurons can thereby indicate the ITD of the sound, with the nucleus as a whole generating a place code for ITDs.

How does ITD sensitivity arise within the MSO? ITD sensitivity in MSO neurons necessarily relies on integrating auditory information from both ears. At the most basic level, MSO neurons act as coincidence detectors. They will fire action potentials when excitatory post-synaptic potentials (EPSPs) from each dendrite integrate at the soma and excite the membrane above threshold. The more the binaural EPSPs overlap, the greater the membrane depolarisation and the greater the probability of an action potential. EPSPs arriving at the soma at the same time are most likely to elicit an action potential.

Given that MSO neurons are sensitive to differences in EPSP timing, they should be extremely sensitive to variations in the lengths of afferent axons. Differences in spherical bushy cell axonal lengths between the ipsilateral and contralateral sides could set the best ITD of an MSO neuron (Jeffress, 1948). This phenomenon is, in fact, used by birds to encode ITDs in the nucleus laminaris (barn owl, Carr and Konishi, 1988). Systematic variations in axonal length along the nucleus—from shorter to longer path lengths—results in a concomitant variation of best ITD. Birds can thereby encode ITDs using the peak of the ITD functions of nucleus laminaris neurons, and in vivo neuronal recordings show that best ITDs cover the full physiological ITD range of barn owls and chickens (Sullivan and Konishi, 1986; Köppl and Carr, 2008). In mammals, there is little evidence for such systematic variation in afferent axon lengths (cat, Karino et al., 2011). The prevalance of contralateral leading best ITDs could arise simply owing to the extra length of the contralateral pathway, which would compensate for the ITD. This does not, however, explain the correlation between best ITDs and best frequency, and other sources of internal delay have been proposed for MSO neurons (Grothe et al., 2018).

Another possible source of internal delay could be that the excitatory inputs to an MSO neuron are tuned to slightly different frequencies. A difference in activation time of inner hair cells in the cochlea occurs naturally as a result of the travelling waves in the basilar membrane. This time difference could be exploited by the brain to tune the ITD function of MSO neurons. No evidence has been found, however, of a systematic difference between the ipsilateral and contralateral inputs that would be useful for ITD coding. Other possible sources of internal delay have been proposed based on neuronal morphology, membrane properties and synaptic physiology, and these will be

discussed in the next section. There could, of course, be many mechanisms of internal delay occurring simultaneously in the brainstem.

Regardless of the source of internal delays, MSO neurons must be able to respond quickly to synaptic inputs. Since they are broadly tuned, each MSO neuron modulates its spike rate to changes in ITD of tens of microseconds (Franken et al., 2015). MSO neurons must therefore possess physiological specialisations to prevent temporal integration of postsynaptic potentials outside of the physiological range of ITDs. These physiological specialisations are described in the next section.

1.4 MSO neuron properties

Irrespective of the precise coding strategy used to localise sounds using ITDs, the neurons of the MSO must respond to extremely fine variations in input timing. MSO neurons are adapted to their role as ITD detectors. They exhibit rapid membrane voltage signalling with respect to both the synaptic input they receive, and the way they integrate that input. In this section, I will describe some of the features of MSO neuron physiology, anatomy and synaptic connectivity that contribute to their rapid voltage signalling.

The cellular physiology of neurons in the MSO has been extensively studied in the gerbil. In vitro studies of MSO physiology have also been conducted using a number of other species, including some in which the MSO is sensitive to ITDs (guinea pig, Smith, 1995; Remme et al., 2014), and others in which it serves other functions (mouse, Fischl et al., 2016; rat, Smith et al., 2000). Here I will focus on studies of the gerbil.

1.4.1 Membrane physiology

Distinguishing features of MSO neurons include notably large ionic currents, especially potassium currents, and extremely short membrane time constants. The input resistance of these neurons in mature animals is typically estimated at between 5 and 10 MΩ, while the membrane time constant is typically estimated at 300 to 800 μs (Scott et al., 2005; Magnusson et al., 2005; Couchman et al., 2010; estimates based on mean values from these studies). In contrast, these parameters in a layer 2/3 cortical pyramidal neuron would be expected to be about an order of magnitude larger (e.g. input resistance about 160 MΩ and time constant about 30 ms as recorded by Salling and

Harrison, 2014). The large ionic currents in MSO neurons rapidly return the membrane to its resting potential following synaptic input, resulting in a very brief time window for synaptic integration compared to other neuronal types (Scott et al., 2005; Mathews et al., 2010).

The leaky membranes of MSO neurons result in minimal back propagation of action potentials, leading to measured somatic amplitudes as low as 10 mV (Scott et al., 2005; Scott et al., 2007). Although they appear small and graded at the soma, they are all-or-none, are tetrodotoxin sensitive, and most likely overshoot in the axon (Scott et al., 2007). These properties indicate that MSO neurons generate typical neuronal action potentials in their axons. It therefore appears that large membrane conductances electrically isolate the soma from the axon. It has been proposed that this is an adaptation to fast firing rates, and prevents back propagating action potentials from interfering with subsequent EPSPs arriving in rapid succession at the soma and dendrites (Golding and Oertel, 2012). This electrical isolation should be expected to impair the MSO neuron's ability to fire action potentials at all. A computational study has indicated that, for high frequency inputs, action potential generation can fail in the axon initial segment, but can instead occur further down the axon, in proximal nodes of Ranvier (Lehnert et al., 2014).

The passive properties of MSO neurons are usually attributed to two main ionic currents, namely a low voltage-activated potassium current (I_{KLT}) and a hyperpolarisation-activated "h"-current (I_h). These currents are conveyed by Kv1 and HCN channels, respectively. Evidence suggests that both of these currents are crucial in setting the resting membrane potential, input resistance and time constant (Scott et al., 2005; Khurana et al., 2012; Baumann et al., 2013). Blocking either of these currents with specific drugs causes increases in both input resistance and time constant (and a positive or negative shift in membrane potential upon blocking either I_{KLT} or I_h, respectively).

Both I_{KLT} and I_h also contribute to the dynamic behaviour of voltage signalling in MSO neurons. Pharmacological block of I_h broadens the time window for coincidence detection by MSO neurons (Khurana et al., 2012). Membrane depolarisation during synaptic excitation rapidly leads to activation of I_{KLT}, which pulls the membrane potential back towards resting levels. In addition, I_{KLT} actively shapes EPSPs as they propagate throughout the neuron. MSO neurons receive excitatory inputs to their dendrites, which

would broaden as they propagated towards the soma if the dendrite behaved as a passive cable. The I_{KLT}, which activates due to the EPSP, "sharpens" the propagating EPSP, effectively cutting it short and bringing the membrane back towards resting potential (Mathews et al., 2010). This effect is greater for larger EPSPs, which recruit more I_{KLT}, and has been termed "voltage-dependent sharpening". Measurements of I_{KLT} show a bias in its intracellular distribution such that conductance is highest at the soma and lowest in the distal dendrites (Mathews et al., 2010).

A voltage-activated sodium current has also been observed in MSO neurons with a somatic bias in channel expression. Scott et al. (2010) observed that somatically biased sodium current has the effect of amplifying EPSPs as they arrive at the dendrite, with the effect that binaural summation of single EPSPs is linear rather than sublinear. This current also had the effect of reducing the action potential voltage threshold when accompanied by preceding inhibition, which is known to occur in MSO neurons (Grothe and Sanes, 1993; Roberts et al., 2013). Inhibition relieves inactivation of the sodium channels, so that small changes in membrane potential elicit larger sodium currents, and therefore greater membrane depolarisation (Scott et al., 2010).

Neither the presence nor the role of other potassium channel subtypes has been thoroughly investigated in MSO neurons. Evidence from other rodents suggests Kv3 channels are likely present in gerbil MSO. In situ hybridisation experiments suggest the presence of Kv3.3 subunits (a tetraethylammonium (TEA) sensitive, high threshold channel) in the MSO of mice (Grigg et al., 2000) and rats (Li et al., 2001). A physiological study of the juvenile mouse MSO demonstrated the presence of TEA sensitive Kv3 channels, which play a role in sharpening action potentials (Fischl et al., 2016). However, the MSO neurons recorded in that study showed larger somatic action potential amplitudes compared to mature gerbil MSO, as well as larger input resistance and slower time constants. The role of high voltage-activated potassium channels in gerbil MSO has not been investigated. Even though action potential back propagation is minimal in MSO neurons (Scott et al., 2007), it is possible that higher input resistance in the thinner distal dendrites could result in sufficiently large EPSPs to recruit high threshold currents (Rautenberg et al., 2009). One aim of this thesis was therefore to investigate the presence and role of potassium currents in MSO neurons.

1.4.2 Morphology

Gerbil MSO neurons exhibit a characteristic bipolar morphology, with two dendritic trees emerging from opposite sides of a fusiform soma (Scott et al., 2005; Rautenberg et al., 2009; see Figure 1.3). Similar morphology is seen in the MSO of many mammals, including the guinea pig (Smith, 1995), mouse (Fischl et al., 2016), rat (Smith et al., 2000), cat (Stotler, 1953; Kiss and Majorossy, 1983), and ferret (Brunso-Bechtold et al., 1990). Superficially similar morphology has also been observed in the nucleus laminaris (the MSO analogue) of some birds, including chickens (Smith and Rubel, 1979), and emus (MacLeod et al., 2006), as well as in crocodilians (Carr et al., 2009). In both chickens and emus, dendritic morphology varies across the tonotopic axis, with higher frequency neurons having shorter dendrites and more dendrites emerging from each side of the soma. Lower frequency neurons more closely resemble mammalian MSO neurons. It is important to note here that the frequency range used for ITD detection by birds can include considerably higher frequencies than those used by mammals (barn owl, Carr and Konishi, 1990). The lower frequency end of the nucleus laminaris is therefore sensitive to a similar range of frequencies to the mammalian MSO. No variation in neuronal morphology along the tonotopic axis has been observed in the MSO in mammals.

The occurrence of bipolar cellular morphology across species, especially across species that independently evolved tympanic hearing (Grothe and Pecka, 2014), suggests it might have some functional relevance. Computational modelling of bipolar neurons suggests this dendritic architecture can enhance coincidence detection (Agmon-Snir et al., 1998). With inputs from each ear confined to separate dendrites, the opposite dendrite can act as a current sink, which reduces the likelihood of suprathreshold EPSPs arising from unilateral synaptic activity.

The geometry of MSO dendrites simplifies during development (Rautenberg et al., 2009). Neurons lose many collateral branches, while main branches thicken. The overall effect is a simplified dendritic tree, with reduced cell surface area but increased cell volume. Rautenberg (2012) conducted computational simulations using the precise morphology of MSO neurons at different ages. He observed reduced attenuation of synaptic inputs in the dendrites, and a consequent reduction in the synaptic conductance required to excite the neuron, concomitant with the changes in dendritic morphology

during development. Together, these morphological and computational studies indicate that bipolar dendritic morphology likely represents one adaption to the challenges associated with submillisecond binaural coincidence detection.

Another morphological feature that has attracted attention is the position of the axon, which in some cases emerges from a proximal dendritic location rather than the soma (Scott et al., 2005; Rautenberg et al., 2009). Although this has been proposed as another possible source of internal delay that could influence ITD tuning (Zhou et al., 2005), no evidence has been found of a systematic variation in axonal position, and the vast majority of axons emerge from the soma (Scott et al., 2005; Rautenberg et al., 2009).

1.4.3 Synaptic input

Glutamatergic excitation

Bilateral excitatory synaptic inputs form the basis of ITD detection in MSO neurons. Each MSO neuron receives glutamatergic synaptic inputs, which are located both on the soma and throughout the dendrites. Inputs are lateralised, so that inputs from the ipsilateral cochlear nucleus form synapses on the lateral dendrite, while inputs from the contralateral cochlear nucleus form synapses on the medial dendrite (Stotler, 1953). Two individually subthreshold EPSPs, one arising from each dendrite, can coincide at the soma to produce a suprathreshold somatic response, resulting in an action potential. If two such EPSPs are offset in time, the second will miss the brief integration time window, and an action potential is unlikely. Partially overlapping EPSPs are associated with varying probabilities of action potential generation, giving rise to the characteristic ITD function of MSO neurons (shown in Figure 1.4).

AMPA receptor mediated excitatory postsynaptic currents in MSO neurons are extremely brief, lasting approximately 250 μs (Couchman et al., 2010). Studies in the rat suggest that MSO neurons express the flop splice variants of glutamate receptors subtypes 3 and 4, which exhibit rapid inactivation (Schmid et al., 2000). The extremely low membrane potentials and time constants of MSO neurons ensure that the subsequent EPSPs are also brief (Mathews et al., 2010). These extremely brief synaptic events contribute to the exquisite time sensitivity of MSO neurons.

EPSPs in MSO dendrites attenuate as they propagate towards the soma (Mathews et al., 2010). This could mean that the neuron is less sensitive to distal dendritic inputs than to more proximal inputs. However MSO neurons also exhibit amplitude normalisation, whereby EPSPs are larger at distal dendritic locations, resulting in more uniform somatic responses, regardless of the synapse location (Winters et al., 2017). In combination with the voltage-dependent sharpening described above, MSO neurons should be expected to be relatively insensitive to the locations of excitatory synapes on their dendrites.

An additional problem arises, however, when considering that excitatory synapses are located along the full extent of the dendrites (Couchman et al., 2012). EPSPs take time to propagate to the soma. This means that even if two dendritic EPSPs occur simultaneously on opposite dendrites, if they differ in their respective distances from the soma, they might not overlap sufficiently to induce an action potential. Even though MSO dendrites are only approximately 150 μm in length (Rautenberg et al., 2009; compare to apical dendrites of layer V cortical pyramidal neurons, which can measure over 1000 μm, e.g. Larkman, 1991), and the propagation time is most likely less than 200 μs even for the most distal synapses (Winters et al., 2017), the extreme sensitivity of MSO neurons to input timing means that these differences could have functional relevance. This would most likely be the case, however, only for certain arrangements of excitatory synapses on MSO dendrites. They could, in principle, be arranged in such a way that distance dependent time discrepancies are minimal. The precise arrangement of synaptic inputs is, however, unknown. Therefore, another aim of this thesis was to determine this arrangement.

A clue about the arrangement of excitatory inputs comes from an in vitro study of synaptic strength (Couchman et al., 2010). In this study, excitatory inputs to the MSO were found to be large and the authors estimated that only two to four active excitatory fibres were required to induce an action potential. This estimate was, however, made based on experiments where inhibitory glycinergic inputs were blocked. Since excitatory inputs are accompanied by glycinergic inhibtory inputs (Roberts et al., 2013), which have the opposite effect on the membrane potential, the minimum required number of excitatory inputs is likely to be greater. Nevertheless, given the magnitude of EPSCs recorded by Couchman et al. (2010), the minimum number of excitatory fibres required to reach threshold is still likely to be few.

Anatomical evidence indicates the presence of excitatory synapses throughout the dendritic tree (Stotler, 1953). Additionally, stimulation of glutamate receptors by neurotransmitter uncaging indicates a uniform distribution of active receptors along the length of the dendrites (Couchman et al., 2012). Together with the large synaptic conductance induced by activating individual fibres, it is likely that excitatory axons projecting to the MSO form many active zones, which could extend along the dendrite. It is already known that inhibitory axons projecting to the MSO form multiple varicosities and active zones on the somata of MSO neurons (Couchman et al., 2010; Werthat et al., 2008). Excitatory inputs could form similar distributed synapses, only spread over a larger area along the dendrites.

Glycinergic inhibition

Synaptic inhibition in MSO neurons is also bilateral. Neurons of the MNTB and LNTB in one hemisphere of the brainstem project glycinergic axons to the ipsilateral MSO. The MNTB is excited by globular bushy cells of the contralateral cochlear nucleus, while the LNTB is excited by globular bushy cells of the ipsilateral cochlear nucleus. The MSO thereby receives inhibitory synaptic input in response to stimulation of either ear. Inhibitory inputs from both nuclei are localised to the somata of MSO neurons in adult animals (gerbil, Kapfer et al., 2002; cat, Clark, 1969). In juvenile gerbils, glycinergic synapses are also found throughout the dendrites, but are refined to the soma following the onset of hearing. (Kapfer et al., 2002; Couchman et al., 2012). Given this developmental profile, the somatic localisation of glycinergic inhibition likely has distinct functional relevance.

In vitro studies have clearly demonstrated the presence of bilateral glycinergic inhibition in the MSO (Grothe and Sanes, 1993; Grothe and Sanes, 1994). Additionally, glycinergic IPSPs driven by auditory nerve stimulation in vitro occur earlier than EPSPs (Roberts et al., 2013). This result is counterintutive given the extra synapse involved in the inhibitory pathway, whereby the MNTB is excited by the cochlear nucleus, and in turn inhibits the MSO. The excitatory pathway consists of direct projections to the MSO from the cochlear nucleus. Evidence suggests that preceding inhibition is made possible by specialisations in the morphology and myelination of globular bushy cell axons (Ford et al., 2015). These adaptations were not observed in mice, which do not utilise ITDs for sound localisation, suggesting that

preceding inhibition could be an important adaptation for ITD processing in the gerbil (Stange-Marten et al., 2017).

Glycinergic inhibition has been shown to modulate the shape and timing of EPSPs in MSO neurons, as well as to reduce the amplitude of the summated synaptically-induced membrane depolarisation. In vitro simulation of glycinergic inhibition using conductance clamp caused changes in EPSP peak times and halfwidths, depending on the magnitude and timing of the inhibition (Roberts et al., 2013). In the study by Roberts et al. (2013), inhibition was estimated to precede excitation by approximately 300-400 μs. For this time difference, EPSP peaks were advanced by a small amount (less than 50 μs), while halfwidths increased slightly (by less than 10%). Another study using conductance clamp found similar EPSP peak advances with preceding inhibition (Myoga et al., 2014). Although Roberts et al. (2013) found no effect of inhibition on the peak of a simulated ITD function, Myoga et al. (2014) found that the right combination of preceding contralateral inhibition and lagging ipsilateral inhibition could shift the peak of the function to prefer contralateral leading excitation. This corresponds to shifting the best ITD of the neuron to a contralaterally leading stimulus (i.e. as observed in vivo, Brand et al., 2002). Synaptic inhibition could therefore be used to set the ITD response function of MSO neurons.

In vivo recordings suggest precisely timed glycinergic inhibition contributes to setting the ITD tuning of MSO neurons (Brand et al., 2002; Pecka et al., 2008). Inhibition of glycine receptors with strychnine in these studies caused a shift in best ITD from contralateral leading to about zero. The shift to zero suggests that axonal propagation times are equal for ipsilateral and contralateral afferents, although other factors could be at play, and it is likely there are mutliple, simultaneously active sources of internal delay, as stated above. A more recent in vivo patch clamp study has shown clear evidence of precisely timed inhibition, at least in some neurons (Franken et al., 2015). Other experiments in the same study show contradictory results to Brand et al. (2002) and Pecka et al. (2008), and the authors suggest a modulatory role for glycine occurring over a longer time period than on a cycle by cycle basis. The precise effect of glycinergic inhibition therefore remains controversial.

GABAergic modulation

In addition to the precisely localised glycinergic inputs, the MSO is innervated by GABAergic axon terminals projecting from the adjacent SPN (Kuwabara and Zook, 1999). These projections form part of a feedback loop whereby MSO neurons send excitatory axonal collateral branches to neurons of the SPN, whose axons release GABA extrasynaptically in the MSO (Stange et al., 2013). GABA receptors in the MSO are found on the presynaptic terminals of glutamatergic inputs from each cochlear nucleus, as well as on the glycinergic inputs from the ventral and medial nuclei of the trapezoid body (Hassfurth et al., 2010). Release of GABA from SPN axons inhibits these synapses and causes an overall reduction in synaptic activity. The ITD response properties of MSO nerons are thereby adjusted to maintain sensitivity to the full range of ITDs over a range of sound intensities (Fischl et al., 2012). Additionally, the modulation of MSO activity dynamically alters the population coding of sound location in the brainstem, resulting in improved spatial resolution at the momentarily most relevant location (Stange et al., 2013).

1.5 Aims

ITD coding by MSO neurons arises through the interaction of excitatory glutamatergic inputs, is shaped by precisely timed inhibitory glycinergic inputs, and is modulated by activity-dependent GABAergic inhibition. Synaptic integration is modulated by large voltage-gated conductances, which set the membrane properties of these neurons. MSO neurons are exquisitely sensitive to input timing as a result of their particular adaptations. One particular adaptation is the expression of a large, low voltage-activated potassium current. Due to the importance of this potassium current, previous studies have neglected the presence and role of other potassium currents. One aim of this thesis was to measure these currents and model their effect on the membrane of MSO neurons. The second aim of this thesis was to investigate the pattern of excitatory synaptic innervation of MSO neurons. As MSO neurons compare submillisecond variations in excitatory input timing, and dendrites impose an additional source of delay on the system, this pattern could represent another specialisation of MSO neurons in their role as ITD detectors.

Chapter 2

Potassium channels in the dendrites and somata of MSO neurons

2.1 Author contributions

Nabel, A. L.*, Callan, A. R.*, Gleiss, S. A., Kladisios, N., Leibold, C. and Felmy, F. **Distinct distribution patterns of potassium channel subunits in somato-dendritic compartments of neurons of the medial superior olive.** (2019) *Frontiers in Cellular Neuroscience*, Volume 13, Article 38.

**these authors contributed equally*

Author contributions: ALN and SAG performed immunofluorescence, ARC, NK and FF performed electrophysiology, ARC and CL performed computational modelling, ALN, ARC, FF and CL analysed and interpreted data, SAG, CL and FF devised experiments, and ALN, ARC, CL and FF wrote the manuscript.

frontiers in Cellular Neuroscience

ORIGINAL RESEARCH
published: 19 February 2019
doi: 10.3389/fncel.2019.00038

Distinct Distribution Patterns of Potassium Channel Sub-Units in Somato-Dendritic Compartments of Neurons of the Medial Superior Olive

Alisha L. Nabel[1,2†], Alexander R. Callan[1,2†], Sarah A. Gleiss[1,2], Nikolaos Kladisios[3], Christian Leibold[4] and Felix Felmy[1,3]*

[1] Division of Neurobiology, Department Biology II, Ludwig-Maximilians-Universität München, Planegg-Martinsried, Germany, [2] Graduate School for Systemic Neurosciences, Ludwig-Maximilians-Universität München, Munich, Germany, [3] Institute of Zoology, University of Veterinary Medicine Hannover, Hanover, Germany, [4] Computational Neuroscience, Department Biology II, Ludwig-Maximilians-Universität München, Planegg-Martinsried, Germany

Coincidence detector neurons of the medial superior olive (MSO) are sensitive to interaural time differences in the range of a few tens of microseconds. The biophysical basis for this remarkable acuity is a short integration time constant of the membrane, which is achieved by large low voltage-activated potassium and hyperpolarization-activated inward cation conductances. Additional temporal precision is thought to be achieved through a sub-cellular distribution of low voltage-activated potassium channel expression biased to the soma. To evaluate the contribution of potassium channels, we investigated the presence and sub-cellular distribution profile of seven potassium channel sub-units in adult MSO neurons of gerbils. We find that low- and high voltage-activated potassium channels are present with distinct sub-cellular distributions. Overall, low voltage-activated potassium channels appear to be biased to the soma while high voltage-activated potassium channels are more evenly distributed and show a clear expression at distal dendrites. Additionally, low voltage-activated potassium channel sub-units co-localize with glycinergic inputs while HCN1 channels co-localize more with high voltage-activated potassium channels. Functionally, high voltage-activated potassium currents are already active at low voltages near the resting potential. We describe a possible role of high voltage-activated potassium channels in modulating EPSPs in a computational model and contributing to setting the integration time window of coincidental inputs. Our data shows that MSO neurons express a large set of different potassium channels with distinct functional relevance.

Keywords: medial superior olive, potassium channel, potassium currents, sub-cellular localization, postsynaptic integration

OPEN ACCESS

Edited by:
Josef Bischofberger, Universität Basel, Switzerland

Reviewed by:
Maarten H. P. Kole, Netherlands Institute for Neuroscience (KNAW), Netherlands
Jan M. Schulz, Universität Basel, Switzerland
Karl Daniel Murray, University of California, Davis, United States

***Correspondence:**
Felix Felmy
felix.felmy@tiho-hannover.de

[†]These authors have contributed equally to this work

Received: *21 June 2018*
Accepted: *23 January 2019*
Published: *19 February 2019*

Citation:
Nabel AL, Callan AR, Gleiss SA, Kladisios N, Leibold C and Felmy F (2019) Distinct Distribution Patterns of Potassium Channel Sub-Units in Somato-Dendritic Compartments of Neurons of the Medial Superior Olive. Front. Cell. Neurosci. 13:38. doi: 10.3389/fncel.2019.00038

INTRODUCTION

Neurons in the medial superior olive (MSO) detect interaural time differences (ITDs) in the microsecond time range by an exquisitely precise integration mechanism (Grothe et al., 2010). The temporal precision of this postsynaptic integration depends on the interaction of dendritic excitation with somatic inhibition (Couchman et al., 2012; Myoga et al., 2014) under the control of voltage-activated ion channels (Scott et al., 2005, 2010; Mathews et al., 2010; Baumann et al., 2013; Roberts et al., 2013; Myoga et al., 2014).

So far only a small number of voltage-gated ion channels have been described in MSO neurons. Pharmacological and immunohistochemical evidence have shown the presence of Kv1.1 (Scott et al., 2005; Mathews et al., 2010; Roberts et al., 2013), HCNs (Khurana et al., 2011; Baumann et al., 2013), Kv3.3 (Grigg et al., 2000; Li et al., 2001) and perisomatic Nav (Scott et al., 2010). HCN1 channels set the membrane potential, contribute to the low input resistance of MSO neurons, counteract inhibitory summation (Baumann et al., 2013), and sharpen the coincidence detection window (Khurana et al., 2012). Koch et al. (2004) show that these channels are expressed in the somatic and dendritic compartments of MSO neurons. Block of Kv3 channels broadens the large action potentials in mice (Fischl et al., 2016). As action potentials in adult gerbil MSO neurons are very small, the presence and function of high voltage-activated potassium channels is unclear. Kv1.1 channels appear to be expressed with a sub-cellular gradient, decreasing toward the distal dendrites (Mathews et al., 2010). These channels generate low voltage-activated currents, whose expression profile indicates a functional relevance in reducing the coincidence detection window (Scott et al., 2005; Mathews et al., 2010) and in interacting with local inhibition to achieve microsecond precise ITD detection (Myoga et al., 2014).

The restriction of Kv1.1 channel expression to the soma and proximal dendrite indicates that other voltage-activated potassium channels might be cooperating at distal dendrites to generate the required outward currents, counteracting the presence of hyperpolarization-activated cation channels (HCN). Furthermore, dendritic excitatory postsynaptic potentials (EPSPs) are likely to reach high voltage levels (Mathews et al., 2010) suited to gate different sets of higher voltage-activated potassium channels. Therefore, we hypothesize that additional voltage-activated potassium channels are likely to be present in neurons of the mature MSO.

Below, we describe the somato-dendritic distribution of seven potassium channel sub-units in the mature MSO. Each of these compartments expresses both low and high voltage-activated potassium channels, yet with different combinations of channel sub-units. In contrast, the counter-balancing HCN1 channel is expressed evenly throughout MSO neurons. Thus, ultra-fast coincidence detection most likely relies on the interplay between synaptic input and a variety of potassium currents expressed at distinct cellular compartments.

MATERIALS AND METHODS

All animal procedures were in accordance with the guidelines of the Regierung of Oberbayern and the Deutsches Tierschutzgesetz and were approved by the local authority's ethics committee (55.2-1-54.2531.8-211-10).

In vitro Slice Preparation and Electrophysiology

Slices were prepared from Mongolian gerbils (*Meriones unguiculatus*) of either sex of postnatal day (P) 45–65. Animals were anesthetized with isoflurane and decapitated. Brains were removed in dissection solution containing (in mM) 50 sucrose, 25 NaCl, 25 $NaHCO_3$, 2.5 KCl, 1.25 NaH_2PO_4, 3 $MgCl_2$, 0.1 $CaCl_2$, 25 glucose, 0.4 ascorbic acid, 3 *myo*-inositol and 2 Na-pyruvate (pH 7.4 when bubbled with 95% O_2 and 5% CO_2). Subsequent to brain removal, 120 μm horizontal slices were taken with a VT1200S vibratome (Leica). Slices were incubated in recording solution (same as slice solution but with 125 mM NaCl, no sucrose and 1.2 mM $CaCl_2$ and 1 mM $MgCl_2$ at 36°C for 15–45 min, bubbled with 5% CO_2 and 95% O_2).

After incubation, slices were transferred to a recording chamber attached to a microscope (BX50WI; Olympus) equipped with gradient contrast illumination and continuously perfused with recording solution. Cells were visualized and imaged with a TILL Photonics system composed of an Imago Retica DC2000 camera, a monochromator and its control unit. Whole-cell recordings were performed using an EPC10/2 amplifier (HEKA Elektronik) on visually identified MSO neurons at 34–36°C. Data were acquired at 50 kHz and low-pass filtered at 3 kHz. For voltage clamp recordings, the access resistances were compensated to a residual of 2 MΩ (access resistance ranged between 4.3 and 8.9 MΩ with the appropriate compensation ranging between 54 and 78%). Whole-cell potassium currents were pharmacologically isolated by SR95531 (SR; 10 μM), strychnine (Stry; 0.5 μM), DNQX (20 μM), DAP5 (50 μM), ZD7288 (50 μM), Cd^{2+} (100 μM), and TTX (1 μM). The intracellular solution was (in mM): 65 *K*-gluconate, 80 Na-gluconate, 4.5 KCl, 15 HEPES, 2 Mg-ATP, 2 K_2-ATP, 0.3 Na_2-GTP, 7.5 Na_2-Phospocreatine, 5 Na-EGTA and 20–50 μM Alexa Fluor 568 (pH adjusted with NaOH to 7.3) leading to a calculated liquid junction potential of ∼14 mV and a calculated potassium reversal of −89 mV (**Figure 6**). For recordings in **Figure 5** the external KCl concentration was raised to 5 mM leading to a calculated potassium reversal of −70.5 mV. Single somatic (**Figure 6**) and dual recordings from soma and dendrite were performed in current clamp with an internal solution containing in mM: 145 *K*-gluconate, 4.5 KCl, 15 HEPES, 2 Mg-ATP, 2 K_2-ATP, 0.3 Na_2-GTP, 7.5 Na_2-phosphocreatine, 5 K-EGTA and 50 μm Alexa Fluor 488 or 568 (LJP ∼16 mV, pH adjusted with KOH to 7.25). For single recordings the electrode resistance was ∼4 MΩ; for somatic and dendritic recordings, electrode resistance in bath was 7–10 MΩ. Series resistance was below 20 MΩ in both somatic and dendritic recording sites used for analysis. For all electrophysiological data the liquid junction potential was corrected offline.

Immunofluorescence and Confocal Microscopy

Immunofluorescence was carried out on free floating slices taken from animals of P50 to 100. Animals were anesthetized (Narcoren, Pentobarbital-Natrium, 20 mg/kg) and perfused with phosphate-buffered saline (PBS) containing 0.1% Heparin and 155 mM NaCl for about 3 min before switching the perfusion to 4% paraformaldehyde. After 25–30 min of perfusion the brains were removed and post-fixed for 3 h or overnight. Brains were washed 3 times in PBS at room temperature for 5 min each and

slices of 60 μm thickness were taken with a VT1000S vibratome (Leica, Wetzlar, Germany). The slices were washed four times in PBS at room temperature for 5 min each. Consequently, they were blocked in 1 ml blocking solution (0.3% Triton, 1% Saponin, 0.1% BSA) for 1 h. After blocking, the slices were incubated in primary antibodies (AB, **Table 1**) diluted in 500 μl blocking solution for 48 h at 4°C on a shaker and subsequently washed 8 times in PBS at room temperature for 5 min each. Additional information regarding the primary ABs is given below. Slices were incubated in secondary ABs (**Table 2**) diluted in 500 μl blocking solution at room temperature for 4 h. Then the slices were mounted in Vectashield medium (H-1000, Vector Laboratories Inc., AXXORA, Lörach, Germany) and sealed with nail polish. Confocal scans were taken with a Leica TCS SPL System (Leica, Wetzlar, Germany). MSO overview images were obtained with a 63× objective (1.32 NA) leading to a pixel size of 481.47 nm * 481.47 nm. Importantly, the images shown represent maximal intensity projections of a 7 image stack with an inter-image distance of 290 nm. Therefore, the displayed dendrites correspond to a 2 μm optical section. Since the radius of MSO dendrites ranges from 1 to 2.5 μm thickness at the investigated locations (Rautenberg et al., 2009) most of the radial extent of a dendrite is collapsed into a single image. High magnification images were generated from scanned stacks with a 63× objective with a 2× zoom, leading to a voxel size of 241.03 nm * 241.03 nm * 293.73 nm. Images used to extract single MSO neurons off-line were acquired with a 63× objective using 1.7× zoom, leading to a voxel size of 282 nm * 282 nm * 293.73 nm. Scan intensity and gain were kept constant for all images regarding a given Kv sub-unit. The intensity of gray scale Kv images and images with blocking peptide are scaled equally to compare the impact of the blocking peptide. Consecutive dual or triple wavelength line scans were always averaged 5 times. Z-chromatic shift between color channels was corrected for red–green–blue (RGB) stacks in ImageJ. Montages of RGB optical sections and maximum-intensity projections were assembled into tables by using custom-written ImageJ plugins and Adobe Photoshop CS software.

Antibody information: The Kv1.1 antibody used here was verified by Zhou et al. (1998) in knock-out mice. We used the same dilution as these authors. The Kv1.2 antibody is knock-out verified by the company NeuroMab. The specificity of this antibody in gerbils can be derived from its precise labeling in the hemi-nodes of MSO axons (Lehnert et al., 2014). Kv2.2 was knock-out verified by Johnston et al. (2008) and Tong et al. (2013). In these studies the presence of Kv2.2 was shown in medial nucleus of the trapezoid body (MNTB) neurons of mice. Kv3.1b and Kv3.2 were also knock-out verified by Kudo et al. (2011) and Barry et al. (2013), respectively. The antibody used to detect Kv1.6 was illustrated to selectively label cells that were also positive for Kv1.6 mRNA (Smart et al., 1997), indicating high specificity. For the antibody directed against Kv2.1 no knock-out verification has been demonstrated so far. To further test the antibody's specificity we included an additional control with a low dilution and also tested the expression in cells that are known to be Kv2.1 positive. Despite our effort to use validated antibodies, standard staining procedures and blocking peptides, we are aware of the limitations and cannot fully rule out off-target protein detection in the Mongolian gerbil.

TABLE 1 | Primary antibodies used in this study.

Antigen	Host	Type	Amino acid residues	Use with secondary AB conjugate with	Dilution	Company	Cat#
HCN1 N70/28	Mouse	Monoclonal	778–910	AMCA	1:500	NeuroMab	75-110
Kv1.1	Rabbit	Polyclonal	416–495	Cy3/A488	1:200	Alomone labs	APC-009
Kv1.2	Mouse	Polyclonal	428–499	DyLight 549	1:500	NeuroMab	75-008
Kv1.6	Rabbit	Polyclonal	463–530	Cy3	1:200	Alomone labs	APC-003
Kv2.1	Rabbit	Polyclonal	841–857	Cy3	1:200, 1:1000	Alomone labs	APC-012
Kv2.2	Rabbit	Polyclonal	859–873	Cy3	1:200	Alomone labs	APC-120
Kv3.1b	Rabbit	Polyclonal	567–585	Cy3	1:200	Alomone labs	APC-014
Kv3.2	Rabbit	Polyclonal	184–204	Cy3	1:200	Alomone labs	APC-011
MAP2	Chicken	Polyclonal		AMCA/A488	1:1000	Neuromics ACRIS	CH22103
S100β	Rabbit	Polyclonal		A488	1:1000	Swant	37
SV2	Mouse	Monoclonal		A488	1:500	DSHB	SV-a1 SV2c
GlyT2	Rabbit	Polyclonal	1–229	Cy3	1:1000	Synaptic Systems	272003

TABLE 2 | Secondary antibodies used in this study.

Antigen	Conjugate	Host	Dilution	Company	Cat#
Anti-mouse	AMCA	Donkey	1:100	Dianova	
Anti-mouse	Alexa488	Donkey	1:200	Invitrogen	A21202
Anti-mouse	DyLight 549	Goat	1:500	Dianova	115-505-207
Anti-rabbit	Cy3	Donkey	1:400	Dianova	711-165-152
Anti-rabbit Fab	Alexa488	Donkey	1:100	Dianova	711-547-003
Anti-chicken	AMCA	Donkey	1:200	Dianova	703-156-155
Anti-chicken	Alexa488	Donkey	1:300	Dianova	703-546-155

Data Analysis

Data were analyzed using Igor Pro (Wavemetrics), ImageJ and Excel. The intensity distribution profiles for Kvs, HCN1, glycine transporter 2 (GlyT2) and microtubule associated protein 2 (MAP2) were extracted by performing line scans (line width: 100 pixels) orthogonally to the MSO dorso-ventral axis on low magnification, maximum intensity projection images using ImageJ. Line scans were taken in the central third of the MSO dorso-ventral extent. These line scans were then fitted with a Gaussian function (IgorPro) and their half-widths were collected. Since the neurons in the MSO are mainly bipolar shaped (Rautenberg et al., 2009) and aligned into a columnar arrangement in gerbils, a Gaussian fit most adequately captures the profile of the fluorescence distribution. The average ratios of Kvs, HCN1 or GlyT2 to MAP2 half-widths were then calculated. A value close to one indicates a distribution largely biased to the somatic/perisomatic region, since MAP2 shows highest expression at the soma and proximal dendrites. Values larger than one indicate a broad, dendritic distribution profile.

For the single cell analysis, MSO neurons were manually labeled using the paintbrush tool in ImageJ to carefully follow the cell through each optical section of the confocal stack. Subsequently, the region outside the paintbrush label was deleted (digital extraction). Then a line scan (width: 9 pixels) was performed along the longitudinal axis of each of these neurons. The average intensity of the first ten pixels from the edge of the cell's nucleus was used for normalization. Only dendrites of at least 75 μm length were taken into account. This dendritic length covers the previous immunofluorescent data in Couchman et al. (2010), and the distance of dendritic recordings (Mathews et al., 2010; Winters et al., 2017) and approximates about two thirds of the overall average length (Rautenberg et al., 2009). Results are presented as mean ± SEM.

Compartmental Modeling

We simulated a minimal multi-compartmental model where a somatic compartment of 30 μm length was sandwiched between two dendrites, each having a total length of 150 μm and consisting of 10 compartments (**Figure 7B**). Each compartment was cylindrical, with somatic diameter 15 μm and tapered dendrites such that the most proximal dendritic compartments had diameter 4.4 μm and the most distal 1.7 μm. The specific axial resistance connecting the compartments was taken as 200 Ωcm, and the specific membrane capacitance as C = 0.9 μF/cm^2 (Gentet et al., 2000). Geometry was adjusted such that the total cell capacitance was approximately 40 pF as previously reported (Rautenberg et al., 2009).

The membrane potential of each compartment was modeled according to a Hodgkin–Huxley type equation:

$$C_m \frac{dV}{dt} = -\sum I_{\text{ionic}}$$

Where I_{ionic} includes axial current between compartments (Lehnert et al., 2014) and transmembrane currents.

In addition to a leak current with 0.05 mS/cm^2 conductance, all compartments were equipped with three active transmembrane currents: (1) A low-threshold potassium current (KLT) modeled according to Mathews et al. (2010). (2) An HCN current modeled according to Baumann et al. (2013) using the parameters for dorsal MSO neurons. (3) A high-threshold potassium current (KHT) modeled based on parameters measured in this study (**Figure 6**). This modeled current is supposed to comprise all molecular sub-types of high voltage-activated potassium channels that we have detected by immunofluorescence.

KHT was modeled as

$$I(V) = g_{\text{KHT},\,peak}\, X^2\, (V - E_K)$$

where the gating variable X, followed the equation

$$\frac{dX}{dt} = \frac{X_\infty - X}{\tau_X}$$

with

$$X_\infty(V) = \frac{1}{1 + e^{\frac{-(V+44.9)}{30}}}$$

(voltage in mV). The square of the activation function was fitted to the measured peak activation function (filled circles in **Figure 6B**), thereby accounting for the exponent 2 in the conductance term. As time constants, we used τ_x = 0.8 ms or 1.5 ms as specified in the results section.

Three variants of the model were tested, with peak channel conductance as outlined in **Table 3**.

The peak channel conductance of KLT was implemented as distance dependent according to

$$g_{\text{KLT}}(X) = g_{\text{KLT},\,peak}(1 + 1.5e^{\frac{-X}{22}})$$

while the conductance was equal in all compartments for HCN and KHT.

The conductance amplitudes were chosen to fit the physiological resting potential and the input resistance recorded at the soma. The reversal potential of potassium was taken as −90 mV, of the HCN current as −35 mV, and of the leak current as −70 mV.

RESULTS

The expression profiles of seven voltage-activated potassium channel sub-units were investigated in neurons of the MSO in adult Mongolian gerbils. The classification of sub-units that contribute to the different types of potassium currents was based on Gutman et al. (2005). To quantify the sub-units' sub-cellular distribution, sections were co-stained with the cellular

TABLE 3 | Peak conductances, in mS/cm^2, for each variant of the model.

Model variant	KLT	KHT	HCN
KLT only	63.4	0	1.265
KHT only	0	1.152	2.58
KLT and KHT	29.9882	0.5449	1.91

marker MAP2. The MAP2 staining was used to delineate the somato-dendritic extent of MSO neurons and to evaluate distribution patterns.

Low Voltage-Activated Potassium Channels

All three low voltage-activated potassium channel sub-units tested were present in MSO neurons (**Figure 1**). Kv1.1 expression appeared biased to the somatic region of MSO neurons and restricted to the postsynaptic membrane surface (**Figure 1A**). The quality and specificity of the Kv1.1 staining was verified by the application of the specific control blocking peptide (**Figure 1A**). In a first gross analysis the expression patterns of MAP2 and Kv1.1 were compared. Toward this aim, line scans orthogonal to the dorso-ventral axis of the MSO were performed on co-stained images. The spatial intensity distribution (arbitrary units, a.u.) of the Kv1.1 and MAP2 line scans was fitted with a Gaussian function to obtain the distribution half-width (**Figure 1A**). From these half-widths the Kv-to-MAP2 ratio was calculated. The average Kv1.1 to MAP2 ratio was 0.92 ± 0.07 (n = 14, **Figure 1D**). A ratio of one indicated that expression profiles of MAP2 and Kv1.1 were similar. Since MAP2 expression was biased to the soma and proximal dendrites of neurons, this therefore indicated that Kv1.1 expression was more prominent at the soma, confirming previous electrophysiological evidence (Mathews et al., 2010).

Kv1.2 staining was more broadly distributed (**Figure 1B**) compared to Kv1.1. The higher magnification image indicates somatic and dendritic expression in the postsynaptic membrane domain, and also a possible contribution of presynaptic elements (**Figure 1B**). The blocking peptide strongly suppressed the Kv1.2 antibody staining, although a weak background of unspecific staining remained (**Figure 1B**). Irrespective of a possible presynaptic bias, line scans were performed from the co-stained image and their intensity distributions fit with a Gaussian (**Figure 1B**). Calculating the Kv1.2 to MAP2 ratio yielded an average value of 1.37 ± 0.12 (n = 5, **Figure 1D**). This indicated that Kv1.2 showed relatively higher dendritic expression with respect to the soma when compared to Kv1.1 sub-units.

Kv1.6 is another DTX-sensitive, low voltage-activated potassium channel (Gutman et al., 2005). Kv1.6 staining was more prominent at the soma but also indicated some expression at the dendrite (**Figure 1C**). The specificity of this staining pattern was supported by the nearly complete loss of fluorescence induced by the blocking peptide (**Figure 1C**). The somatically biased staining was quantitatively verified by the line scan analysis (**Figures 1C,D**) yielding an average ratio of 1.01 ± 0.03 (n = 8; **Figure 1D**). Therefore, Kv1.6 and Kv1.1 appeared locally co-expressed toward the soma, while Kv1.2 covered a larger part of the dendritic extent.

So far, our line scan analysis was based on images of the entire MSO and took all cellular components within this nucleus into account. To restrict the expression analysis to the postsynaptic somato-dendritic compartment, single MSO neurons were digitally extracted from the image stacks [(Couchman et al., 2010); **Figure 1E**]. This allowed a line scan analysis exclusively of the somato-dendritic compartment (**Figures 1E,F**), from which the region of the nucleus of an MSO neuron could be determined (**Figure 1F**). The borders of the nucleus were then used to align the spatial extent of line-scans from different dendrites. By this alignment the somatic region covered only about 8 μm (**Figures 1G–I**). The normalized Kv1.1 (dendrites: n = 19, **Figure 1G**) and Kv1.6 (n = 10, **Figure 1I**) fluorescence decayed rapidly from the soma to 50% at a dendritic distance of 35 and 24 μm, respectively. Kv1.2 (n = 7, **Figure 1H**) expression, however, remained above 50% of the somatic intensity for the entire dendritic distance measured here. Thus, different low voltage-activated potassium channels were expressed with distinct spatial profiles in MSO neurons, and were present in both the soma and the dendrite.

Distribution of Kv1.1 With HCN1 and GlyT2

Low voltage-activated currents have been proposed to interact with I_h currents (Khurana et al., 2011) mediated by HCN1 and HCN2 sub-units (Koch et al., 2004; Khurana et al., 2012; Baumann et al., 2013). To detect overlapping distribution profiles where these channels can directly interact for compartmentalized voltage signaling, we stained cells for Kv1.1, HCN1 and MAP2 (**Figure 2B**). The HCN1 sub-unit was broadly distributed (**Figure 2A**). The line scan analysis of these triple labeled samples (**Figure 2A**) leads to an average HCN1 to MAP2 ratio of 2.13 ± 0.44 and Kv1.1 to MAP2 ratio of 0.86 ± 0.05 (n = 8, **Figure 2C**). Moreover, low voltage-activated potassium currents have been suggested to interact with the voltage signaling of glycinergic inhibition (Myoga et al., 2014). Therefore, we also co-stained for GlyT2 and MAP2 proteins (**Figure 2B**). For GlyT2 and MAP2 the gross line scan analysis revealed a ratio of 0.82 ± 0.05 (n = 11, **Figure 2C**). Therefore, as demonstrated before (Clark, 1969; Kapfer et al., 2002; Couchman et al., 2010, 2012), inhibitory inputs are constrained to the soma and proximal dendrite (**Figure 2A**), and thus they localize exquisitely well with Kv1.1, indicative of a functional interaction between glycinergic inhibition and Kv1.1 activation (Myoga et al., 2014), whereas HCN channels were evenly distributed and only partially overlapped with Kv1.1. The dichotomy between Kv1.1 and HCN1 distribution was verified by single cell analysis (**Figures 2D,E**). On average, the normalized Kv1.1 fluorescence reached half maximum at 31.1 μm distance from the nucleus, whereas HCN1 fluorescence remained stable over the entire dendritic extent (n = 12). Thus, the differential distribution of HCN1 and Kv1.1 indicates that their proposed interplay (Khurana et al., 2011) is limited to the somatic region and that at distal dendrites HCN1 contributes to voltage signaling decoupled form Kv1.1.

High Voltage-Activated Potassium Channels

Kv2.x and Kv3.x activate at higher voltage levels compared to Kv1.x channels (Gutman et al., 2005; Johnston et al., 2008).

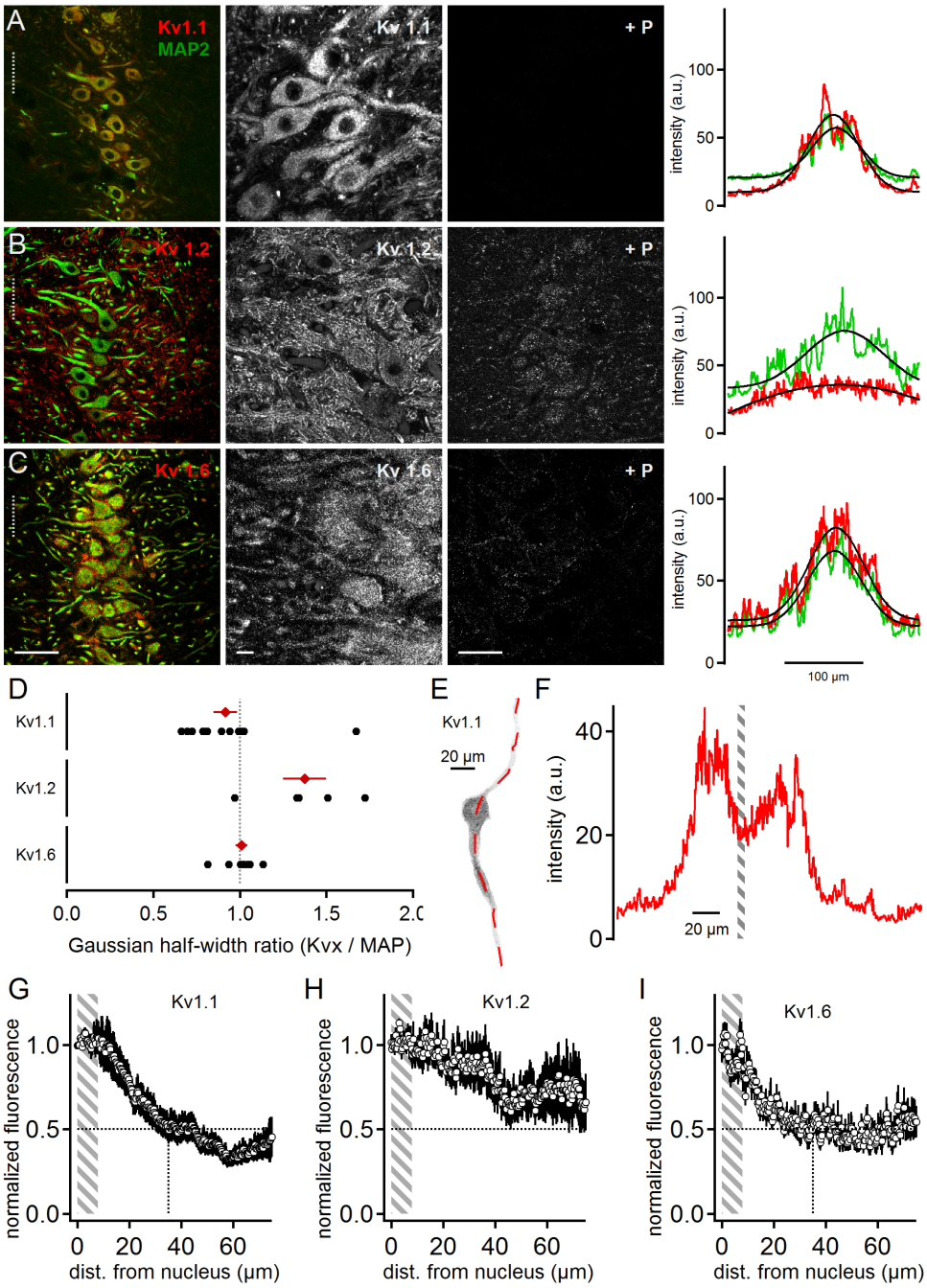

FIGURE 1 | Low voltage-activated potassium channels in medial superior olive (MSO) neurons. **(A)** Immunofluorescent staining of Kv1.1, MAP2 (co-staining left, magnified Kv1.1 image middle) and Kv1.1 blocking peptide (+P, right). Intensity scaling of the gray scaled images is identical, to indicate the effect of the blocking peptide. Line scan intensity profiles are shown as arbitrary units (a.u.) on the right. The line scan was taken from the left image at the position of the gray dotted line. Colors match the color code in the left image. The black line indicates a Gaussian fit on the intensity distributions. Scale bars: left 50 µm, middle 10 µm, right 50 µm. **(B)** Same as in **(A)** but for Kv1.2 sub-unit staining. **(C)** Same as in **(A)** but for Kv1.6 sub-unit staining. **(D)** Quantification of the intensity distributions shown in **(A–C)**. The half width of the Gaussian fit was used to calculate the potassium channel to MAP2 ratio for Kv1.1 (n = 14), Kv1.2 (n = 5), and Kv1.6 (n = 8). Black symbols represent single images, red symbols represent average values. The gray dotted line indicates distribution profile equivalent to that of MAP2. Large values indicate a broader, more dendritic distribution profile. **(E)** Single, digitally extracted MSO neuron stained for Kv1.1. The position of the line scan is given by the red dotted line. **(F)** Intensity profile of the line scan shown in **(E)**. Gray area indicates the region of the cell's nucleus. **(G)** Normalized intensity distribution of Kv1.1 (n = 19) in single MSO neurons. The edge of the nucleus was defined as zero position. Gray area indicates the region of the soma. Dotted horizontal line indicates the half decay of the normalized intensity. Dotted vertical line indicates the position the intensity reached half of its initial value. **(H)** Same as in **(G)** but for Kv1.2 (n = 7) sub-unit staining. **(I)** Same as in **(G)** but for Kv1.6 (n = 10) sub-unit staining.

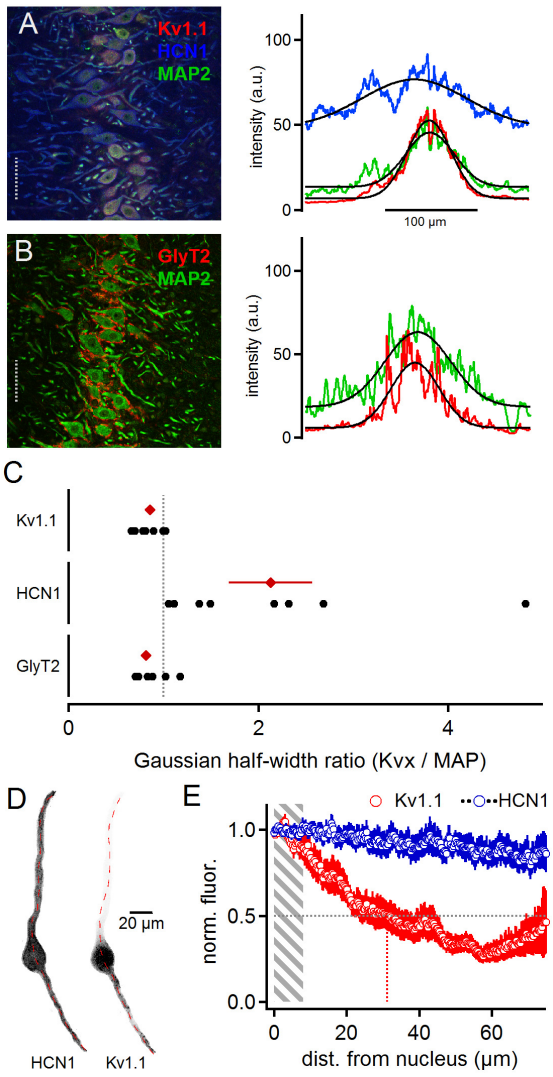

FIGURE 2 | Matching distributions of Kv1.1 and GlyT2 but not HCN1. Panel **(A)** shows HCN1, KV1.1, and MAP2 co-staining (left). The lines scan intensity profiles are shown as arbitrary units (a.u.) on the right. The line scan was taken from the left image at the position of the gray dotted line. Colors match the color code of the left image. The black line indicates a Gaussian fit on the intensity distributions. Scale bar equals 50 µm. Panel **(B)** shows GlyT2 and MAP2 co-staining. **(C)** Quantification of the intensity distributions shown in **(A,B)**. The half width of the Gaussian fit was used to calculate the GlyT2 (n = 11), HCN1/KV1.1 (n = 8) to MAP2 ratio. Black symbols represent single images, red symbols represent average values. The gray dotted line indicates a distribution profile equivalent to that of MAP2. Larger values indicate a broader, more dendritic distribution profile. **(D)** Single, digitally extracted, MSO neuron co-stained for HCN1 and Kv1.1. The position of the line scan is given by the red dotted line. **(E)** Normalized intensity distribution of HCN1 and the co-stained Kv1.1 (n = 12) in single MSO neurons. The edge of the nucleus was defined as zero position. Gray area indicates the region of the soma. Gray dotted line indicates the half decay of the normalized intensity. Colored dotted line indicates the position the intensity reached half of its initial value.

In MSO neurons, dendritic depolarizations might reach such voltage levels (Mathews et al., 2010) and therefore, potentially activate high voltage-activated potassium channels. We therefore stained for four high voltage-activated potassium channel sub-units to determine whether they could potentially contribute to voltage signaling in MSO neurons.

Both Kv2.1 and Kv2.2 could be detected all along the MSO neurons from the soma to the distal dendrite (**Figures 3A,B**). This expression pattern was apparent in the overview and the high magnification images. For both antibodies the blocking peptide prevented all staining (**Figures 3A,B**), indicating high specificity. The line scan analysis for the presented overview images indicated a broader intensity profile compared to the MAP2 staining (**Figures 3A,B**). The average Kv2.1 and Kv2.2 to MAP2 ratio was 1.46 ± 0.15 (n = 6) and 1.48 ± 0.20 (n = 7), respectively (**Figure 4C**). Since Kv2.x expression is rather unusual in auditory brainstem neurons and found to be restricted to medial (MNTB) and ventral nucleus of the trapezoid body (VNTB) neurons in mouse (Johnston et al., 2008; Tong et al., 2013) we used additional Kv2.1 staining to confirm antibody specificity. First, the same staining pattern was observed for a fivefold lower antibody concentration (**Figure 3C**). Second, the antibody detected Kv2.1 in moto-neurons, cortical neurons (**Figures 3D,E**) and the cerebellum, all of which are known to express these channel types (Escoubas et al., 2002; Guan et al., 2007; Zhuang et al., 2012; Bishop et al., 2015, 2018). Particularly for cortical pyramidal neurons, the patched staining obtained here in gerbils (**Figure 3E**) matches the staining pattern in mice (Bishop et al., 2015, 2018). Thus, we conclude that the high voltage-activated potassium channels Kv2.1 and 2.2 are distributed rather uniformly in MSO neurons.

Positive immunostainings were also obtained for the high voltage-activated potassium channel sub-units Kv3.1b and Kv3.2 (**Figure 4**). This contrasts earlier reports (Li et al., 2001) that have detected Kv3.3 but not Kv3.1b expression in neurons of the rat MSO. Kv3.1b sub-units were detected in overview and magnified images in the soma and dendrites in addition to strong nuclear labeling (**Figure 4A**). All labeling appeared specific as indicated by the fluorescence loss by the addition of the blocking peptide (**Figure 4A**). Despite the strong nuclear labeling, the line scan analysis indicated a broad distribution of Kv3.1b throughout the MSO (**Figure 4A**). The average line scans led to a Kv3.1b to MAP2 ratio of 1.25 ± 0.13 (n = 7, **Figure 4C**). This Kv3.1b expression profile contrasted with the expression of Kv3.2, which appeared more localized to the soma (**Figure 4B**). In the higher magnification images weaker dendritic staining was also apparent (**Figure 4B**). The gross quantification by the line scans of the overview images (**Figure 4B**) yields a Kv3.2 to MAP ratio of 0.71 ± 0.06 (n = 8, **Figure 4C**). Thus, our data showed that high voltage-gated potassium channels were present in MSO neurons with distinct expression patterns (**Figure 4C**).

Line scan analysis of digitally extracted single cells was carried out for the high voltage-gated sub-units Kv2.1, Kv3.1b, and Kv3.2 (**Figures 4D,E**). The images and the line scans were again used to detect the edges of the nucleus (**Figure 4E**). The normalized and spatially aligned fluorescence values corroborated the somatic and dendritic expression patterns of Kv2.1 and Kv3.1b (**Figures 4F,G**). In contrast, Kv3.2 expression dropped below 50%

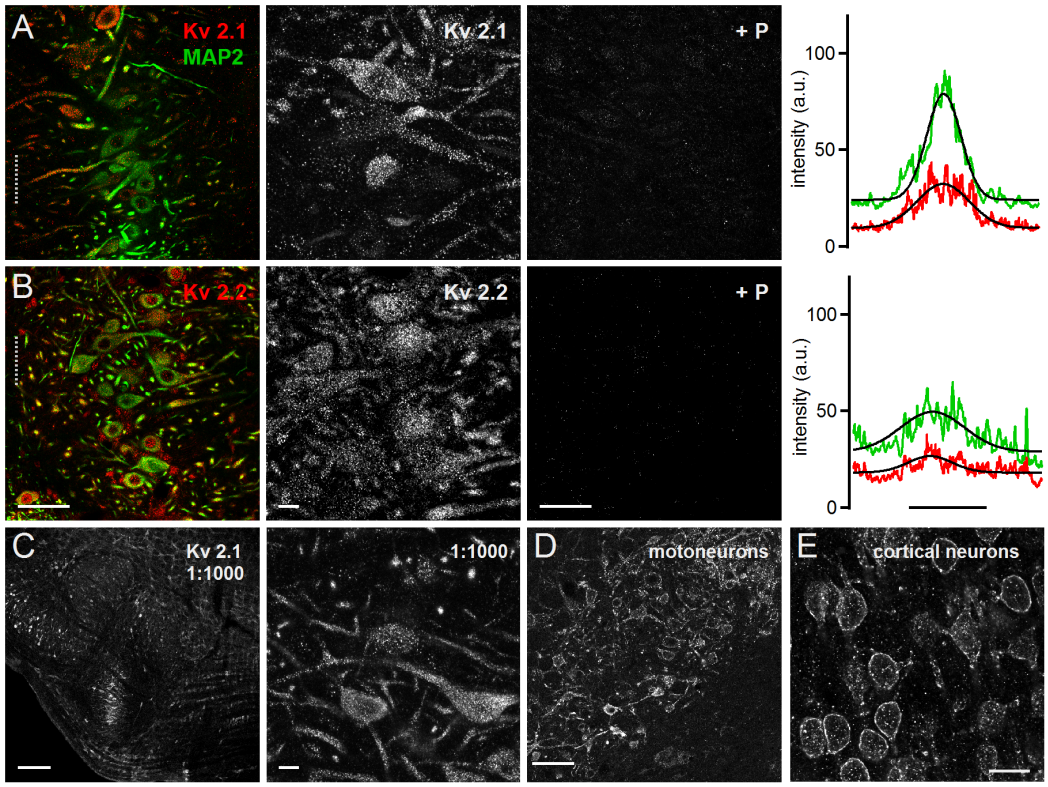

FIGURE 3 | Medial superior olive neurons express Kv2.1 and Kv2.2. **(A)** Immunofluorescent staining of Kv2.1, MAP2 (co-staining left, magnified Kv2.1 image middle) and Kv2.1 blocking peptide (+P, right). Intensity scaling of the gray scaled images is identical, to indicate the effect of the blocking peptide. Line scan intensity profiles are shown as arbitrary units (a.u.) on the right. The line scan was taken from the left image at the position of the gray dotted line. Colors match the color code in the left image. The black line indicates a Gaussian fit on the intensity distributions. Scale bars: left 50 μm, middle 10 μm, right 50 μm. **(B)** Same as in **(A)** but for Kv2.2 sub-unit staining. **(C)** Control staining of higher Kv2.1 antibody dilution of the superior olivary complex (left) and in the MSO (right). Scale bars equal 200 μm (left) and 10 μm (right). **(D,E)** Control images of brain regions of well documented Kv2.1 expression. **(D)** Moto-neurons in the brainstem of the facial nerve. Standard antibody dilution of 1:200 was used. **(E)** Pyramidal neurons in cortex. Scale bars equal 100 μm.

of somatic expression at a distance of only 25 μm from the nucleus rim (**Figure 4H**).

Pharmacological Verification of Expression of Multiple Potassium Channels

Diverse potassium channels could be pharmacologically identified during voltage clamp recordings. We used subsequent application of low concentrations of tetraethylammonium (TEA 1 mM) and 4-aminopyridine (4-AP 2 mM, **Figure 5**) on a background of dendrotoxin (DTX) to directly demonstrate the presence of Kv3 and Kv4 type potassium channels, leaving Kv2 channels as a predominant remaining current (Gutman et al., 2005; Johnston et al., 2010). As the presence of a large low voltage-activated potassium current has been demonstrated before using DTX (Scott et al., 2005; Mathews et al., 2010; Roberts et al., 2013), we conducted this pharmacological assay on a background of 100 nM α-DTX, which blocks Kv1.1, Kv1.2, and Kv1.6.

Despite the presence of α-DTX, MSO neurons (n = 6) generated a large inactivating outward current (**Figure 5A**). This current shows peak and steady state values of about 6.17 ± 0.77 nA and 2.57 ± 0.38 nA, respectively, at 1 mV holding potential (**Figure 5B**). The resulting current shows a large fraction of inactivation (**Figure 5C**). Additional bath application of 1 mM TEA reduced the overall peak and steady state MSO potassium current (**Figure 5B**), leaving a remaining inactivating potassium current (**Figures 5B,C**). To corroborate that under the α-DTX and α-DTX/TEA conditions different currents types remain, we analyzed their inactivating time course. The weighted decay time constant was faster after the addition of TEA (**Figure 5D**). The subtraction of the TEA sensitive current itself is consistent with the presence of a Kv3.x driven potassium current (Gutman et al., 2005). In agreement with the presence of Kv3.x channels in auditory brainstem (Wang et al., 1998; Li et al., 2001; Chang et al., 2007; Kulesza, 2014) this TEA sensitive current had average peak and steady state values of 3.76 ± 0.48 nA and 1.42 ± 0.29 nA at a holding potential of 1 mV, respectively (**Figure 5E**). Thus, this TEA sensitive current showed a substantial fractional inactivation (**Figure 5E**). The subsequent application of 4-AP reduced the potassium current further, indicating the presence of inactivating A-type potassium current based on Kv1.4 and/or Kv4.x channels (Gutman et al., 2005;

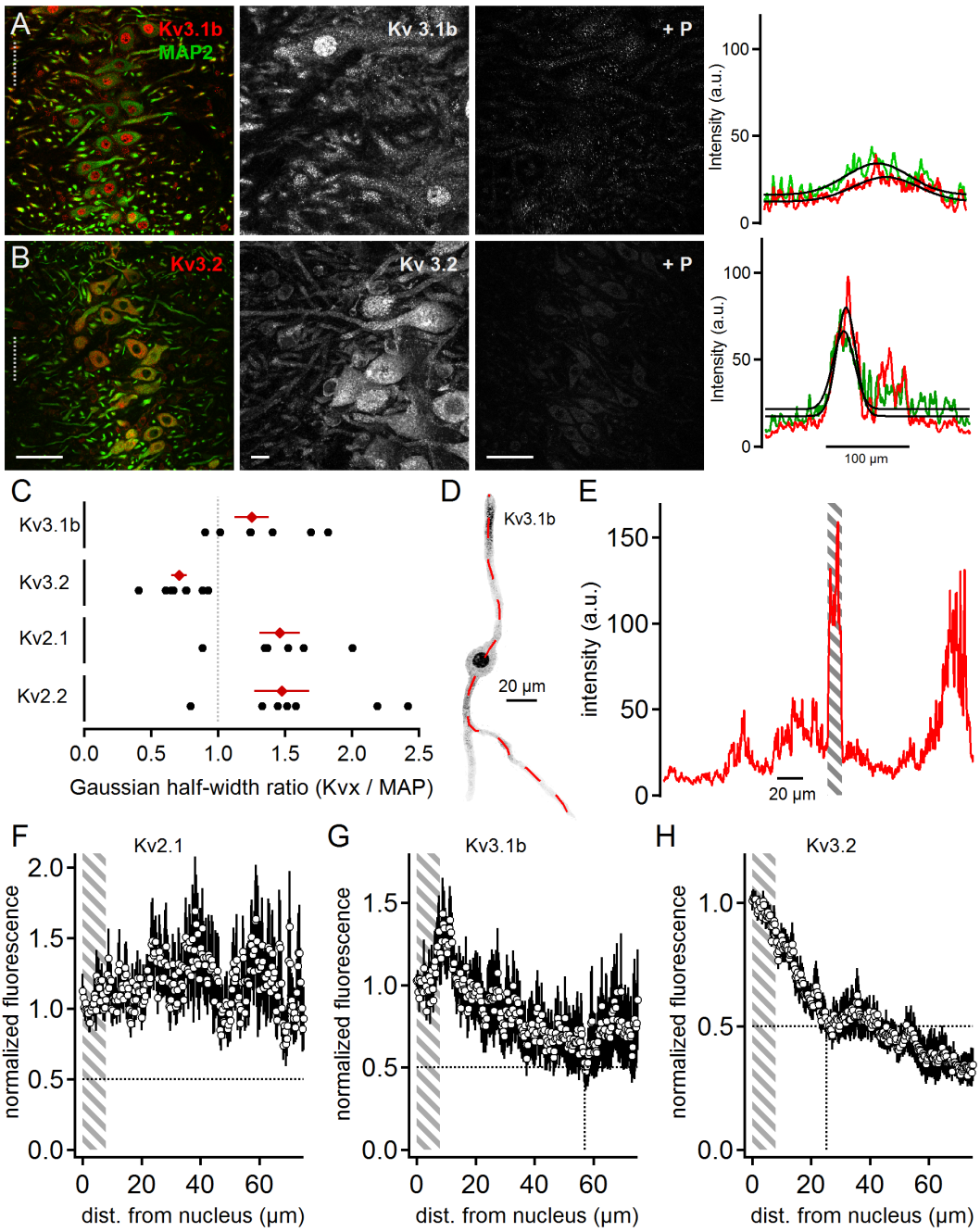

FIGURE 4 | High voltage-activated potassium channels in MSO neurons. **(A)** Immunofluorescent staining of Kv3.1b, MAP2 (co-staining left, magnified Kv3.1b image middle) and Kv3.1b blocking peptide (+P, right). Intensity scaling of the gray scaled images is identical, to indicate the effect of the blocking peptide. Line scan intensity profiles are shown as arbitrary units (a.u.) on the right. The line scan was taken from the left image at the position of the gray dotted line. Colors match the color code in the left image. The black line indicates a Gaussian fit on the intensity distributions. Scale bars: left 50 µm, middle 10 µm, right 50 µm. **(B)** Same as in **(A)** but for Kv3.2 sub-unit staining. **(C)** Quantification of the intensity distributions shown in **(A,B)** and for Kv2.1 and Kv2.2 staining shown in **Figure 2**. The half width of the Gaussian fit was used to calculate the potassium channel to MAP2 profile for Kv3.1b (n = 7), Kv3.2 (n = 8), Kv2.1 (n = 6), and Kv2.2 (n = 7). Black symbols represent single images, red symbols represent average values. The gray dotted line indicates a distribution profile equivalent to that of MAP2. Larger values indicate a broader, more dendritic distribution profile. **(D)** Single, digitally extracted MSO neuron stained for Kv3.1b. The position of the line scan is given by the red dotted line. **(E)** Intensity profile of the line scan shown in **(D)**. Gray area indicates the region of the cell's nucleus. **(F)** Normalized intensity distribution of Kv2.1 (n = 13) in single MSO neurons. The edge of the nucleus was defined as zero position. Gray area indicates the region of the soma. Dotted horizontal line indicates the half decay of the normalized intensity. **(G)** Same as in **(F)** but for Kv3.1b (n = 6) sub-unit staining. Dotted vertical line indicates the position the intensity reached half of its initial value. **(H)** Same as in **(F)** but for Kv3.2 (n = 9) sub-unit staining. Dotted vertical line indicates the position the intensity reached half of its initial value.

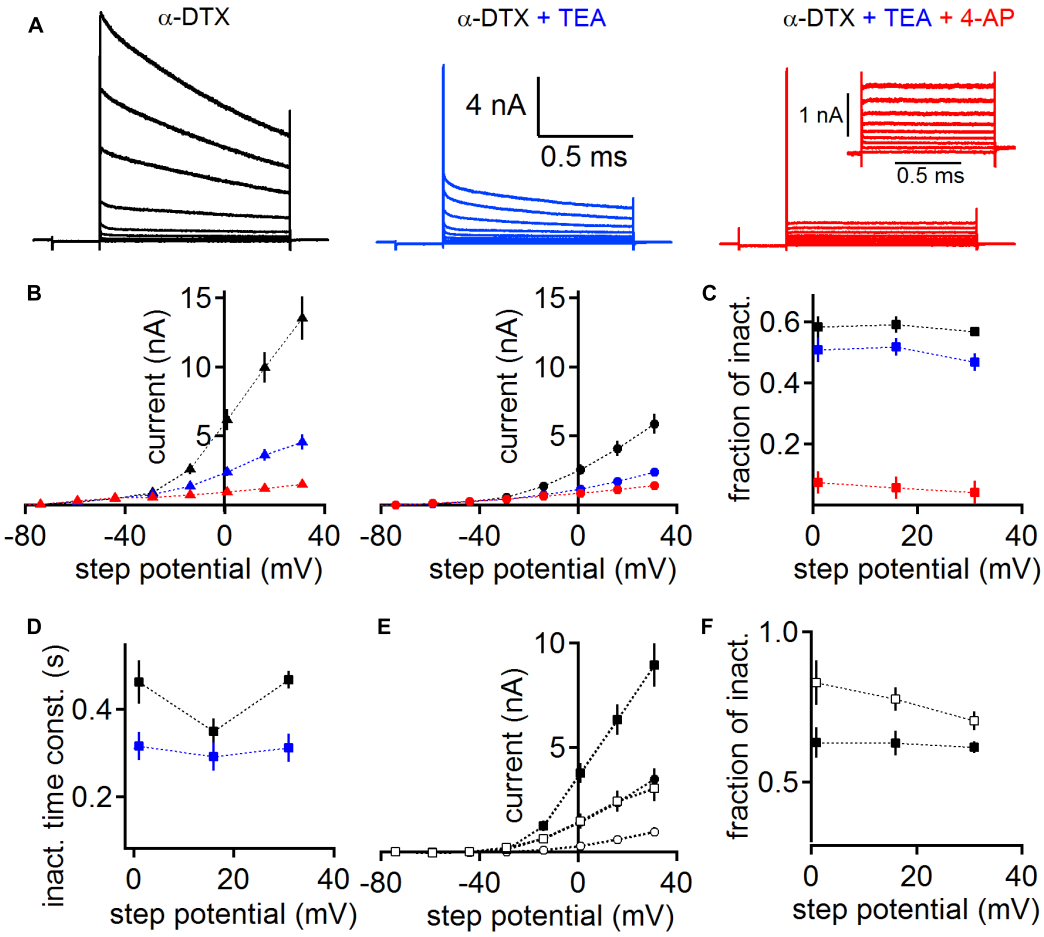

FIGURE 5 | Pharmacological verification of different classes of voltage-activated potassium channels. **(A)** MSO whole-cell currents in the presence of 100 nM α-DTX (left), after the addition of 1 mM TEA (middle) and 2 mM 4-AP (right). Inset (right) shows the magnified remaining potassium current in the presence of α-DTX, TEA, and 4-AP. **(B)** The potassium peak (left) and steady state (right) current as a function of step potential. Colors represent the different pharmacological conditions: black: α-DTX; blue: α-DTX + TEA; red: α-DTX + TEA + 4-AP. The steady state current was determined at the end of the step potential. **(C)** Fraction of inactivation (peak – steady state/peak) for the potassium currents under the pharmacological conditions described in **(B)**. **(D)** Weighted decay time course of inactivation of the currents recorded under α-DTX (black) or α-DTX + TEA (blue). **(E)** The peak (square symbols) and steady state (round symbols) current of the TEA (black symbols) and 4-AP (open symbols) sensitive currents gained after subtraction. **(F)** The fractional inactivation of the TEA and 4-AP sensitive current. Symbols as in **(D)**.

Johnston et al., 2010). The 4-AP sensitive current had an average peak amplitude of 1.47 ± 0.36 nA and a steady state amplitude of 0.28 ± 0.11 nA at a holding potential of 1 mV, and inactivated by about 50% (**Figure 5E**). The final remaining potassium current had an average peak amplitude of 0.93 ± 0.11 nA and a steady state amplitude of 0.86 ± 0.1 nA for a holding potential of 1 mV (**Figure 5B**), and hence showed little inactivation (**Figure 5C**). Therefore its inactivation time course was not analyzed. The pharmacological profile and the low fractional inactivation suggested that the remaining potassium current was driven by Kv2.x channels (Gutman et al., 2005; Johnston et al., 2010). Taken together, we pharmacologically verified the presence of the low and high voltage-activated potassium currents, which we have identified with immunofluorescence. In addition, our pharmacological analysis suggests the presence of further A-type potassium channel sub-units that underlie 4-AP sensitivity.

So far our data show that mature MSO neurons express many low and high voltage-activated and possibly A-type potassium channel sub-units. On the sub-cellular level each sub-unit showed expression along the full length of the cell, albeit with a somatic or dendritic bias. Each potassium current type is therefore likely to be present at each cellular compartment, yet with low voltage-activated potassium currents localized more somatically and high voltage-activated potassium currents located more dendritically. Next, we aimed to obtain functional insights into the presence of high voltage-activated potassium currents.

In order to obtain functional insights from a computational model we first quantified the biophysical characteristics of the overall whole-cell high voltage-activated potassium current. Toward this aim we recorded potassium currents in the presence of DTX and pre-depolarized (to 0 mV for 1 s) the cells to inactivate possible A-type currents before using step commands between −84 and 36 mV to activate

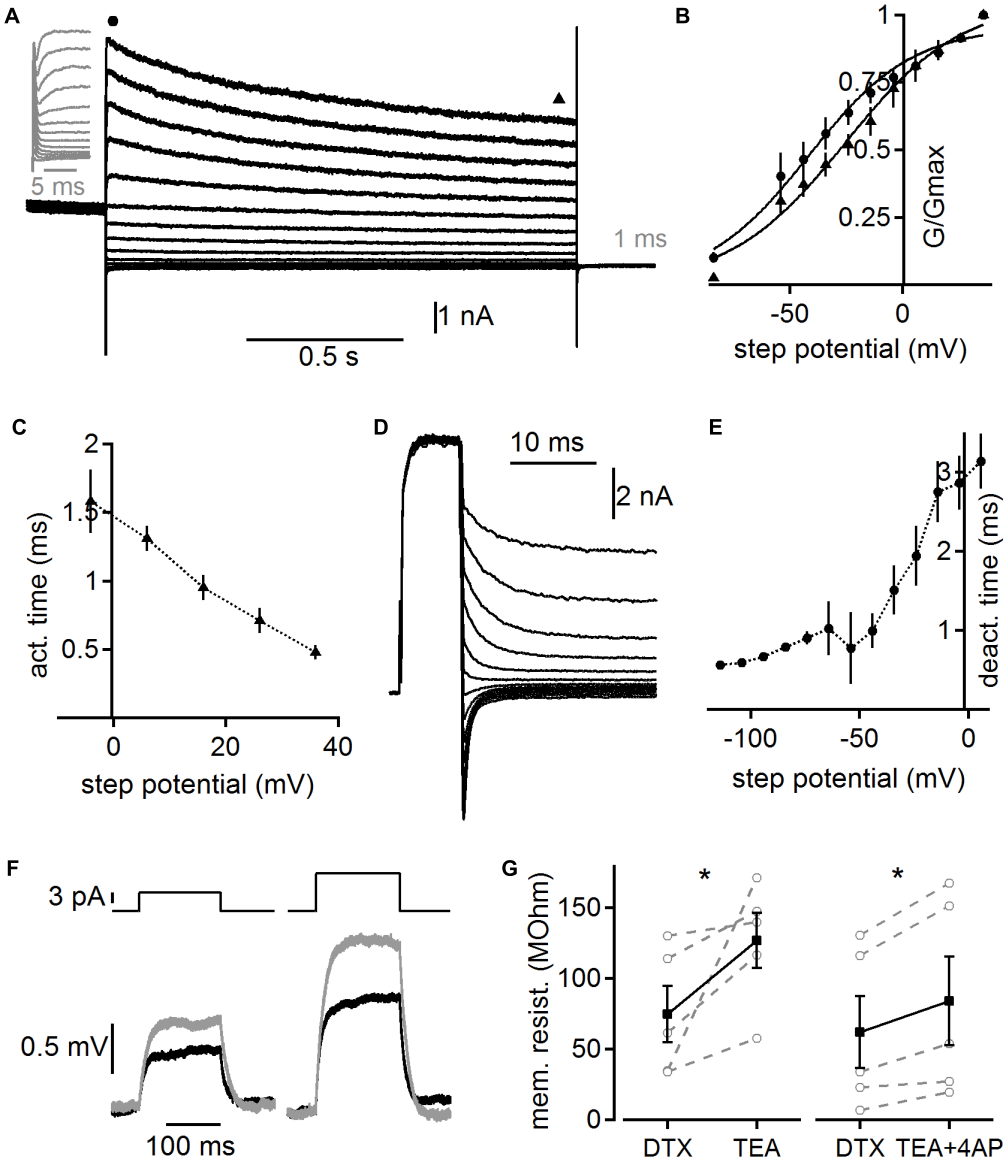

FIGURE 6 | Voltage dependent kinetics of high voltage-activated potassium currents. **(A)** Potassium currents evoked by step potentials between 36 and –84 mV after a 1 s long pre-depolarization to 0 mV to pre-inactivate possible remaining low voltage-activated and A-type potassium currents. Currents recorded in the presence of 100 nM DTX. Gray inset magnifies the onset of the current. Circle and triangle highlight regions of the onset and steady state current used for further analysis shown in **(B)**. **(B)** Voltage dependent activation of potassium currents as shown in **(A)**. Circle and triangle correspond to the onset and steady state current, respectively. **(C)** Activation time constants derived from exponential fits to the onset of the potassium currents as shown in **(A)**. **(D)** High voltage-activated potassium tail currents recorded in the presence of 100 nM DTX. A 7 ms long depolarization to 36 mV was followed with step potentials between 6 and –114 mV. **(E)** Deactivation time was derived from the rapid component of a bi-exponential fit to the deactivation currents as shown in **(D)**. **(F)** Membrane deflections in response to a 5 and 10 pA current injection. Black trace depicts control recorded in the presence of DTX (100 nM), ZD7288 (50 μM), and TTX (1 μM). Gray trace shows the response following under the addition of TEA (1 mM). **(G)** Membrane resistance after additional application of TEA (1 mM) and TEA plus 4-AP (2 mM) derived from experiments illustrated in **(F)**. Asterisk indicates significance (paired *T*-Test, $p < 0.05$).

high voltage-activated potassium currents (**Figure 6**). The voltage dependent activation of the peak and steady state conductance indicates that high voltage-activated potassium currents are already activated at low voltages in adult MSO neurons (n = 6). Fitting the voltage dependent activation indicates rather shallow voltage dependence, which is in accord with the presence of several channel sub-types with distinct but overlapping kinetics. The activation time of this lumped whole-cell high voltage-activated potassium current was determined by exponential fits to the rising phase of the current following the artifact. Step potentials to above -10 mV yielded fits appropriate for further analysis. The average activation time constant was voltage dependent and was below 1.5 ms above 0 mV (**Figure 6C**). To determine

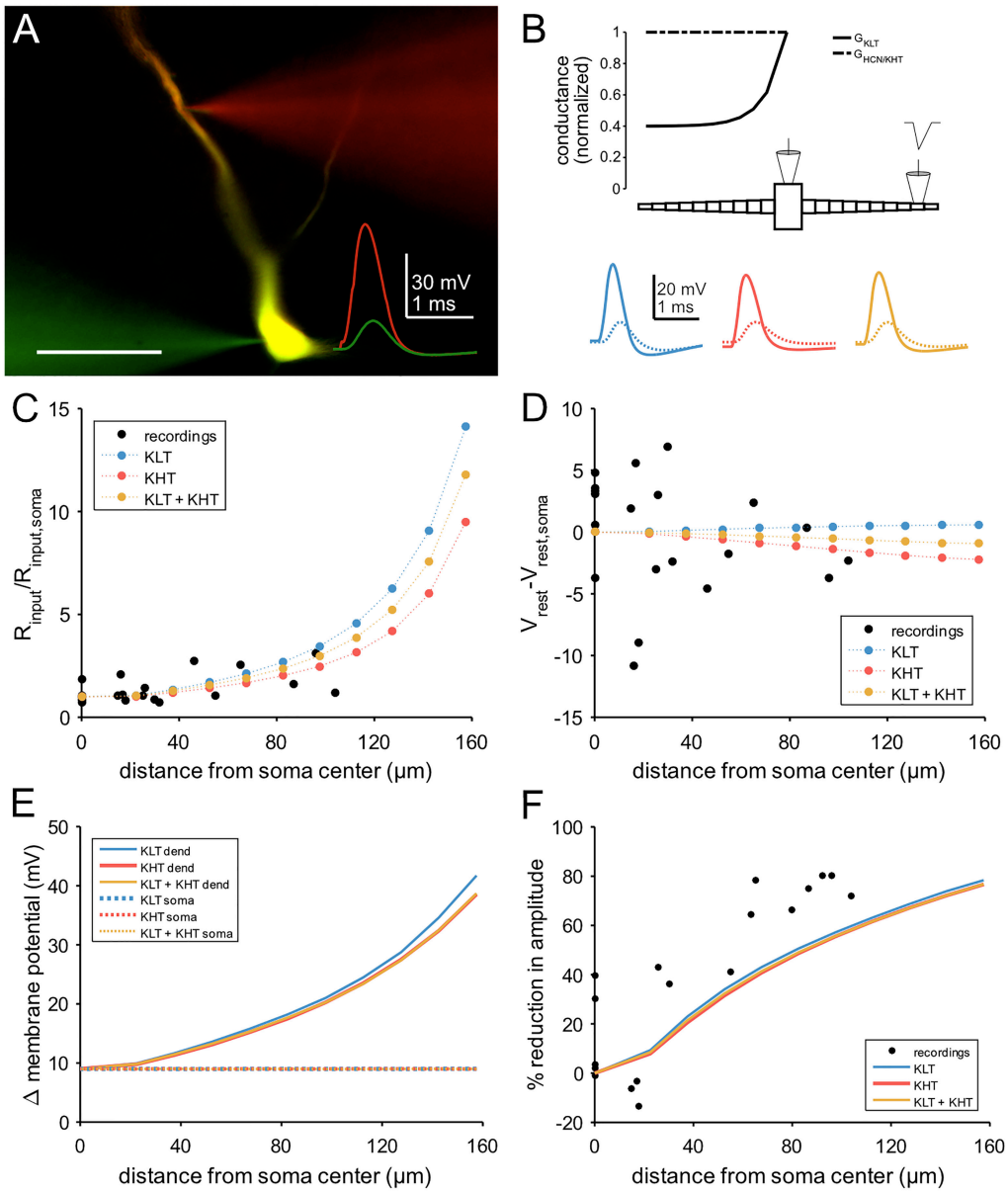

FIGURE 7 | Compartmental model of an MSO neuron incorporating KHT. **(A)** Dual patch clamp in MSO. Traces show response to a triangular current pulse injected at the somatic electrode. Scale bar = 50 µm. **(B)** Schematic of compartmental model, showing spatial distribution of active conductances. Below: membrane potential of each model variant in response to the same triangular current pulse used for dual recordings, injected into a single distal dendritic compartment. Blue = KLT, red = KHT, and yellow = KLT + KHT. Solid line = dendritic compartment, dotted line = somatic compartment. **(C)** Input resistance divided by the somatic value with respect to distance from soma. **(D)** Resting membrane potential less the somatic value with respect to distance from soma. **(E)** Peak membrane voltage change in the model in response to the triangular current pulse used in recordings. Current amplitude set to produce a somatic voltage change of approximately 9 mV. **(F)** Attenuation of EPSP amplitude with respect to distance of stimulation site from soma.

the deactivation time constant a depolarization for 7 ms to 36 mV was followed by a step command between 6 and −114 mV (**Figure 6D**). The resulting tail current was best fit by a double exponential function, of which the fast time constant was attributed to the high voltage-activated potassium channel's deactivation. This analysis showed that voltage dependent deactivation ranged from 3.14 ± 0.348 ms to 0.56 ± 0.003 ms (**Figure 6E**). This time course is in the range with fits obtained from the tail currents to the holding command potential of −74 mV (0.532 ± 0.47 ms) of the stimulation paradigm shown in **Figure 6A**. Thus, our data indicate a broad voltage activation range of fairly rapidly activating high voltage-activated potassium currents with low activation thresholds that allow some of these channels to be open at the resting potential of adult MSO neurons. The broad voltage dependent activation range is

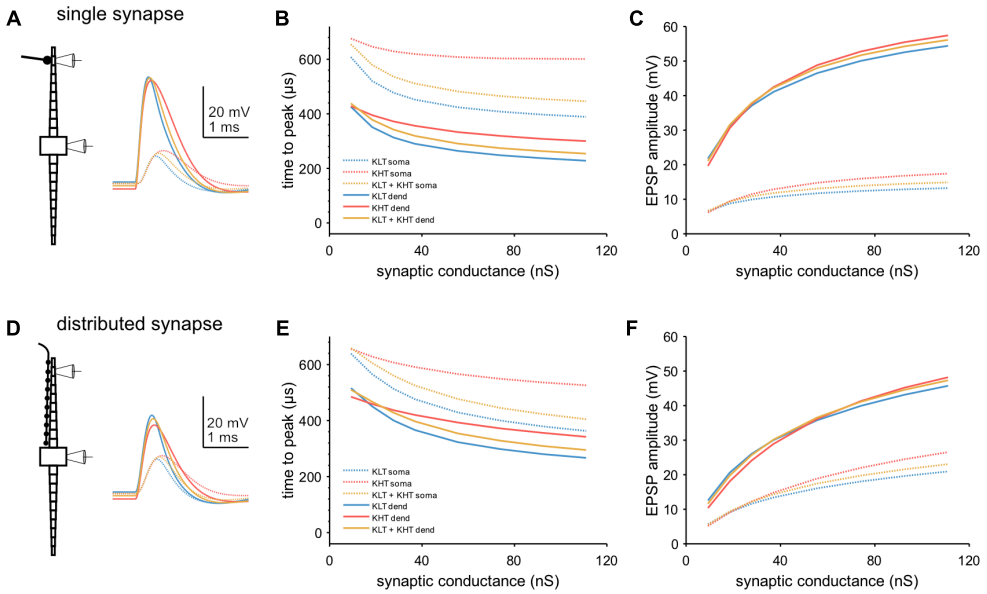

FIGURE 8 | Model response to simulated synaptic stimulus. **(A)** Example model responses to EPSG of 37 nS at a single dendritic site. Traces from stimulated dendritic (solid lines) and somatic (dotted lines) compartments as indicated by pipette icons. Blue = KLT, red = KHT, and yellow = KLT + KHT. **(B)** EPSP peak times relative to EPSG onset for a single, distal dendritic input. **(C)** Amplitude of EPSPs with respect to peak synaptic conductance for a single, distal dendritic input. Legend same as **(B)**. **(D)** Same as **(A)**, but with synaptic input spread evenly across all compartments of one dendrite. **(E)** EPSP peak times relative to EPSG onset for synaptic input distributed across the full dendrite. **(F)** Amplitude of EPSPs with respect to peak synaptic conductance for distributed synaptic input. Legend same as **(E)**.

likely due to the overlap of several different high voltage-activated potassium channel sub-types, consistent with our immunofluorescence.

To verify the low voltage activation of the non-DTX sensitive high voltage-activated potassium channel, we determined its impact on the membrane resistance close to resting potentials. A step current between 5 and 50 pA was applied 30 times and the average voltage deflection (**Figure 6F**) was used to determine the membrane resistance from the steady state level according to Ohm's law. Cells were kept at similar potentials before (-55.8 ± 1.68 mV) and after (-57.0 ± 1.04 mV) the application of high voltage-activated potassium blockers by current injections. After DTX, TTX, and ZD7288 were present for ~10 min in the bath TEA (1 mM) or TEA plus 4-AP (2 mM) were additionally applied. The input resistance significantly increased for both conditions from an average of 74.6 ± 20.1 to 126.5 ± 19.8 ($n = 5$; $p = 0.04$; **Figure 6G**) and from 62.0 ± 25.4 to 83.8 ± 31.4 MΩ ($n = 5$; p = 0.013; **Figure 6G**) for TEA alone and TEA plus 4-AP, respectively. Thus, high voltage-activated potassium channels contribute significantly to the resting input resistance of adult MSO neurons.

Modeling the Impact of High Voltage-Activated Potassium Currents on Postsynaptic Integration

To investigate a possible role for high voltage-activated potassium channels, we constructed a conductance-based compartmental model based on dual somatic and dendritic patch clamp recordings (**Figures 7A,B**). We constrained the model with the measured cellular parameters somatic input resistance (6 MΩ) and resting membrane potential (−68 mV). Both parameters were consistent between the recordings and the model (**Figures 7C,D**). The modeled morphology represents a simplified version of the adult MSO dendrite (Rautenberg et al., 2009) and consisted of a single somatic compartment and two tapering dendrites (see section "Materials and Methods"). In the following, three versions of the model were tested, one with only low voltage-activated potassium channels ("KLT"), one with only the DTX insensitive potassium currents we measured ("KHT"), and one with a mix of both ("KLT + KHT"). For the mixed model, we reduced the maximum conductance of each potassium current to maintain the passive membrane properties. Both conductances were reduced by an equal percentage from the values in their respective single potassium current models. This necessitated an adjustment of the HCN peak conductance as indicated in the section "Materials and Methods." Although both potassium conductances activate at resting potential their main distinction is the steeper activation curve of the KLT. We repeated all simulations with two different time constants for the KHT gating variable (see section "Materials and Methods"). We found no qualitative difference between the simulations using either time constant. All results reported in this section are from simulations using the faster time constant of 0.8 ms for activation and deactivation.

The passive properties varied along the dendrite to a different extent between models. The KLT model showed a greater increase in input resistance compared to the KHT model, with the

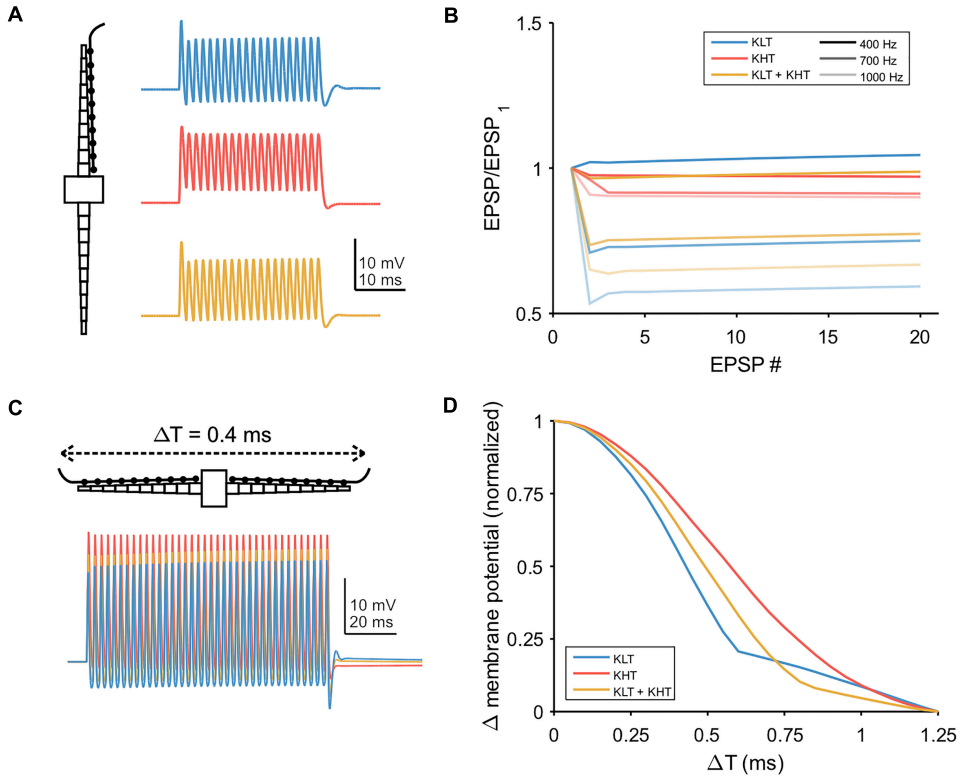

FIGURE 9 | Temporal integration in model. **(A)** Example traces showing the somatic response to a train of twenty EPSPs at 700 Hz, with synaptic conductance distributed across one dendrite. Blue = KLT, red = KHT, and yellow = KLT + KHT. **(B)** EPSP amplitude divided by the amplitude of the first EPSP for each EPSP in the train at three different frequencies. **(C)** Simulations of 100 ms trains of EPSGs distributed along the length of each dendrite. Somatic voltage response shown. EPSP frequency = 400 Hz, time difference of EPSG onset between dendrites = 0.4 ms. **(D)** Peak membrane potential depolarization with respect to the difference in input timing between dendrites (ΔT). Measured at the end of the EPSP train. Peak membrane potential depolarizations (ΔV_m) for each model version were normalized to the range 0–1 according to the following equation: Normalized $\Delta V_m = [\Delta V_m - \min(\Delta V_m)]/[\max(\Delta V_m) - \min(\Delta V_m)]$.

mixed model intermediate between the two. Nevertheless, as these differences were greatest in the distal dendrite, all models appear consistent with measured values (**Figure 7C**). Resting membrane potential varied only minimally along the dendrite, consistent with the recorded values, which showed no trend (linear regression, $p = 0.38$; **Figure 7D**).

We compared the attenuation of membrane potential deflections between recordings and each version of the model. For both patch clamp recordings and model simulations we used a triangular current pulse injected through the dendritic electrode (**Figures 7A,B**). The peak current magnitude used for simulations was adjusted to give an approximately 9 mV voltage change at the soma. The change in dendritic membrane potential required to produce a 9 mV somatic deflection increased with greater distance from the soma, but did not differ noticeably between model variants (**Figure 7E**). Attenuation therefore did not differ between model variants (**Figure 7F**). Attenuation was somewhat less than the recorded values from patch clamp experiments, most likely due to the absence of dendritic branching in our model, which artificially increases dendritic diameter for a fixed cell surface area.

We next looked at EPSP kinetics and observed a difference in peak timing between variants of the model when we simulated single EPSGs [peak conductance = 37 nS; (Couchman et al., 2010)] at a single distal dendritic compartment (**Figure 8A**). We found that peak time was latest in the KHT only model and earliest in the KLT only model over a range of synaptic conductances (**Figure 8B**). The mixed model peak times at the soma were consistently just under 60 μs later than the KLT model over the range of synaptic conductance. Somatic EPSP amplitudes were highest for the KHT only model, which were up to 4 mV larger than in the KLT only model, although the differences were smaller for smaller synaptic strengths (**Figure 8C**). Amplitudes in the mixed model were generally intermediate between the other two variants.

We repeated these simulations with the synaptic conductance distributed among all compartments along the dendrite (**Figure 8D**). Total synaptic conductance was the same as for stimulation at a single synaptic site. With this synaptic configuration, both peak timing and amplitude showed the same qualitative trend between each model variant (**Figures 8E,F**). Differences in somatic peak times were somewhat closer between variants with this synaptic configuration, with 40–50 μs between the KLT only and mixed models for most synaptic strengths. In summary, KHT channels seem to trade latency for amplitude, where latency and amplitude are reduced the

less KHT is in the model, due to the consequently larger amount of KLT.

We also simulated trains of synaptic input, with the synaptic conductance distributed throughout the dendrite (**Figure 9A**). We first simulated a train of EPSGs (peak total conductance = 37 nS) on one dendrite and looked at how the peak membrane potential varied throughout the train (**Figure 9B**). For a lower input frequency (400 Hz) each model variant showed minimal change in EPSP amplitude throughout the train. For higher frequencies, models containing KLT responded with an initial larger EPSP followed by a reduction in amplitude for the remaining EPSPs, by up to about 40% for the KLT only model at 1000 Hz. The mixed model followed this trend, with somewhat smaller amplitude reductions, while the KHT only model did not.

Finally, we simulated bilateral synaptic inputs (400 Hz, 100 ms, peak total conductance per dendrite = 37 nS) and varied the relative timing of inputs between each dendrite (example in **Figure 9C**). We measured the peak membrane potential depolarization from rest at the end of the EPSG train and plotted the normalized response relative to the peak at zero time difference (**Figure 9D**). The half-width of the response function was smallest for the KLT only model (0.43 ms) and largest for the KHT only model (0.61 ms), with the mixed model again falling in between the other variants (0.51 ms). These results corroborate our previous conclusion that the benefit of KHT channels is mostly reflected by the increase in the response amplitude (**Figure 9C**), but reduces the temporal resolution of the coincidence curve.

DISCUSSION

Here we show the diversity of spatial distribution profiles of potassium channels expressed in MSO neurons of mature gerbils. MSO neurons express low and high voltage-activated potassium channel sub-units in distinct spatial patterns. Sub-units for each of these current types are present in each dendro-somatic compartment of the MSO neuron, yet in different combinations and weights. Low voltage-activated potassium channels are more biased toward the soma, whereas high voltage-activated potassium channels also exhibit strong dendritic contributions. The presence of these types of channels and their contribution to the resting input resistance was verified pharmacologically. Computational modeling based on current kinetics indicated that high voltage-activated ion channels can modulate EPSP timing and amplitude, thereby directly affecting the binaural coincidence detector mechanism.

Low Voltage-Activated Potassium Channels

We show that, in addition to Kv1.1, the low voltage-activated potassium channel sub-units Kv1.2 and 1.6 are expressed in neurons of the mature MSO, similar to neurons of the medial nucleus of the trapezoid body (Dodson et al., 2002; Brew et al., 2003). These sub-units show different expression profiles along the dendro-somatic axis. Kv1.1 and 1.6 are predominantly localized to the soma and proximal dendrites. Conversely, Kv1.2 localization was also present at the dendrite. Overall, low voltage-activated potassium channels appeared localized more to the soma and proximal dendrite. This expression profile agrees with pharmacological data (Mathews et al., 2010). Since Kv1.x sub-units can form heteromultimers (Sheng et al., 1993), our data indicate that the low voltage-activated potassium current is most likely a heteromultimer based on at least Kv1.1, Kv1.2 and Kv1.6 sub-units, as in the medial nucleus of the trapezoid body (Dodson et al., 2002; Brew et al., 2003) and octopus cells (Cao and Oertel, 2017).

Functionally, as indicated by the application of DTX, the low voltage-activated potassium channel mediated currents decrease the input resistance, the membrane time constant, and the EPSP half width, and shorten action potential and IPSP duration in MSO neurons (Scott et al., 2005; Mathews et al., 2010; Baumann et al., 2013; Myoga et al., 2014). Besides the somatic bias, some low voltage-activated potassium channels were also located distal to the soma. Therefore, low voltage-activated potassium currents might possess additional functions at more distal dendrites where they could directly interact with distal rapid AMPA-receptor mediated synaptic excitation (Couchman et al., 2010). Moreover, our present data support the functional role of low voltage-activated potassium channels, especially Kv1.1 and Kv1.6, in reducing the time course of IPSPs (Baumann et al., 2013; Myoga et al., 2014). This support is based on the matching expression profiles of these channel sub-units with GlyT2, a marker for inhibitory synapses, suggesting local interactions during voltage signaling.

High Voltage-Activated Potassium Channels

We demonstrate here, pharmacologically and by immunofluorescence, the expression of high voltage-activated potassium channels in mature MSO neurons. The presence of Kv2.x and Kv3.x is consistent with a TEA sensitive current and the remaining DTX, TEA and 4-AP insensitive current (Johnston et al., 2010). Such a current has also been recently documented in MSO neurons of juvenile mice (Fischl et al., 2016). In mice this current supports the repolarization of a large action potential not present in gerbil MSO neurons. Kv2.x expression is less well documented in the auditory brainstem and was only recently found to be particularly strong in the medial and ventral nucleus of the trapezoid body (Johnston et al., 2008; Tong et al., 2013). While labeling was predominant in the axonal initial segments of MNTB neurons it was found somatically in the VNTB. Here we now present dendritic labeling of Kv2.x in the MSO of adult gerbils. Our Kv3.1b stainings indicate a species difference to rats, where expression of Kv3.1 RNA was not found in the MSO (Li et al., 2001). On the other hand, our pharmacological data indicating the presence of KV3.x in adult MSO neurons of gerbils matches the reported presence of Kv3 in juvenile MSO neurons of mice (Fischl et al., 2016). In regard to the distribution profiles, Kv2.1, Kv2.2 and Kv3.1b were predominantly expressed at the dendrite and only Kv3.2 was biased strongly to the soma of adult MSO neurons. The similar distribution pattern of Kv2.1 and Kv2.2 in the MSO might indicate that these sub-units form

heteromultimers (Blaine and Ribera, 1998). Furthermore, speed of the activation and deactivation kinetics recorded at the soma is more in line with Kv3.x than Kv2.x channels. It can be speculated that the rapid kinetics at the soma are due to the differential distribution patterns of the distinct high voltage-activated potassium channels.

The expression of high voltage-activated potassium channels is unexpected in neurons that are well known to have only very little action potential backpropagation and small action potential amplitudes *in vitro* (Scott et al., 2005, 2007; Chirila et al., 2007; Lehnert et al., 2014). Yet our electrophysiological data suggest that these channels contribute to the resting input resistance, consistent with activation at low voltages. As our data is based on insensitive DTX currents our interpretation might be slightly contaminated if DTX insensitive low voltage-activated potassium channel subunits such as Kv1.3, Kv1.4 or Kv1.5 were present in MSO neurons. Now with the assumption that DTX blocks all low voltage-activated potassium channels in MSO neurons, our computational model indicates that, even at resting levels, high voltage-activated potassium channels contribute to setting the membrane potential, as they were in competition with a low amount of low voltage-gated potassium channels. Nevertheless, due to their steeper activation curve, low voltage-activated potassium channels dominated the dynamics of the mixed KLT + KHT model membrane potential.

The addition of KHT, and concomitant reduction of KLT, appears to slightly "worsen" the performance of our model neuron in measures commonly considered important for MSO neurons (Scott et al., 2005; Mathews et al., 2010). KHT induces a peak delay of up to 60 μs, which is a relevant time delay for ITD processing (Lesica et al., 2010). It is not clear, however, whether this additional latency is detrimental for ITD processing. Indeed, *in vitro* recordings using conductance clamp suggest that slower EPSGs can allow the cell to more effectively modulate the timing of peak membrane depolarization (Myoga et al., 2014). Given that MSO neurons operate at an extreme in terms of the magnitude of membrane conductances and the brevity of time constants, KHT may help counterbalance the effects of the large DTX-sensitive KLT currents, and modulate the neuronal excitability to bilateral inputs.

Our study shows that voltage signaling in MSO neurons is based on many different potassium channels with distinct spatial expression profiles in the somato-dendritic compartments. As the focus of this study was on the somato-dendritic compartments, which carry out the voltage signaling underlying ultrafast coincidence detection, their expression and contribution to the voltage signaling in the axonal compartment and therefore to action potential generation remains unanswered. In spite of the lack of overshooting action potentials in the somato-dendritic compartments of these neurons, they still possess a full set of voltage-activated potassium channels whose full function we have just started to disentangle.

AUTHOR CONTRIBUTIONS

AN and SAG performed immunofluorescence. AC, NK, and FF performed electrophysiology. AC and CL performed computational modeling. AN, AC, NK, FF, and CL analyzed and interpreted data. SAG, CL, and FF devised experiments, AN, AC, CL, and FF wrote the manuscript.

FUNDING

This work was supported by the Elisabeth and Helmut Uhl Foundation and the DFG: CRC870.

ACKNOWLEDGMENTS

We thank Benedikt Grothe for generous support and discussion.

REFERENCES

Barry, J., Xu, M., Gu, Y., Dangel, A. W., Jukkola, P., Shrestha, C., et al. (2013). Activation of conventional kinesin motors in clusters by Shaw voltage-gated K+ channels. *J. Cell Sci.* 126, 2027–2041. doi: 10.1242/jcs.122234

Baumann, V. J., Lehnert, S., Leibold, C., and Koch, U. (2013). Tonotopic organization of the hyperpolarization-activated current (Ih) in the mammalian medial superior olive. *Front. Neural Circ.* 7:117. doi: 10.3389/fncir.2013.00117

Bishop, H. I., Cobb, M. M., Kirmiz, M., Parajuli, L. K., Mandikian, D., Philp, A. M., et al. (2018). Kv2 Ion channels determine the expression and localization of the associated AMIGO-1 cell adhesion molecule in adult brain neurons. *Front. Mol. Neurosci.* 11:1. doi: 10.3389/fnmol.2018.00001

Bishop, H. I., Guan, D., Bocksteins, E., Parajuli, L. K., Murray, K. D., Cobb, M. M., et al. (2015). Distinct cell- and layer-specific expression patterns and independent regulation of Kv2 channel subtypes in cortical pyramidal neurons. *J. Neurosci.* 35, 14922–14942. doi: 10.1523/JNEUROSCI.1897-15.2015

Blaine, J. T., and Ribera, A. B. (1998). Heteromultimeric potassium channels formed by members of the Kv2 subfamily. *J. Neurosci.* 18, 9585–9593. doi: 10.1523/JNEUROSCI.18-23-09585.1998

Brew, H. M., Hallows, J. L., and Tempel, B. L. (2003). Hyperexcitability and reduced low threshold potassium currents in auditory neurons of mice lacking the channel subunit Kv1.1. *J. Physiol.* 548, 1–20. doi: 10.1113/jphysiol.2002.035568

Cao, X. J., and Oertel, D. (2017). Genetic perturbations suggest a role of the resting potential in regulating the expression of the ion channels of the KCNA and HCN families in octopus cells of the ventral cochlear nucleus. *Hear. Res.* 345, 57–68. doi: 10.1016/j.heares.2017.01.001

Chang, S. Y., Zagha, E., Kwon, E. S., Ozaita, A., Bobik, M., Martone, M. E., et al. (2007). Distribution of Kv3.3 potassium channel subunits in distinct neuronal populations of mouse brain. *J. Comp. Neurol.* 502, 953–972. doi: 10.1002/cne.21353

Chirila, F. V., Rowland, K. C., Thompson, J. M., and Spirou, G. A. (2007). Development of gerbil medial superior olive: integration of temporally delayed excitation and inhibition at physiological temperature. *J. Physiol.* 584, 167–190. doi: 10.1113/jphysiol.2007.137976

Clark, G. M. (1969). The ultrastructure of nerve endings in the medial superior olive of the cat. *Brain Res.* 14, 293–305. doi: 10.1016/0006-8993(69)90111-5

Couchman, K., Grothe, B., and Felmy, F. (2010). Medial superior olivary neurons receive surprisingly few excitatory and inhibitory inputs with balanced strength and short-term dynamics. *J. Neurosci.* 30, 17111–17121. doi: 10.1523/JNEUROSCI.1760-10.2010

Couchman, K., Grothe, B., and Felmy, F. (2012). Functional localization of neurotransmitter receptors and synaptic inputs to mature neurons of the medial superior olive. *J. Neurophysiol.* 107, 1186–1198. doi: 10.1152/jn.00586.2011

Dodson, P. D., Barker, M. C., and Forsythe, I. D. (2002). Two heteromeric Kv1 potassium channels differentially regulate action potential firing. *J. Neurosci.* 22, 6953–6961. doi: 10.1523/JNEUROSCI.22-16-06953.2002

Escoubas, P., Diochot, S., Celerier, M. L., Nakajima, T., and Lazdunski, M. (2002). Novel tarantula toxins for subtypes of voltage-dependent potassium channels in the Kv2 and Kv4 subfamilies. *Mol. Pharmacol.* 62, 48–57. doi: 10.1124/mol.62.1.48

Fischl, M. J., Burger, R. M., Schmidt-Pauly, M., Alexandrova, O., Sinclair, J. L., Grothe, B., et al. (2016). Physiology and anatomy of neurons in the medial superior olive of the mouse. *J. Neurophysiol.* 116, 2676–2688. doi: 10.1152/jn.00523.2016

Gentet, L. J., Stuart, G. J., and Clements, J. D. (2000). Direct measurement of specific membrane capacitance in neurons. *Biophys. J.* 79, 314–320. doi: 10.1016/S0006-3495(00)76293-X

Grigg, J. J., Brew, H. M., and Tempel, B. L. (2000). Differential expression of voltage-gated potassium channel genes in auditory nuclei of the mouse brainstem. *Hear. Res.* 140, 77–90. doi: 10.1016/S0378-5955(99)00187-2

Grothe, B., Pecka, M., and McAlpine, D. (2010). Mechanisms of sound localization in mammals. *Physiol. Rev.* 90, 983–1012. doi: 10.1152/physrev.00026.2009

Guan, D., Tkatch, T., Surmeier, D. J., Armstrong, W. E., and Foehring, R. C. (2007). Kv2 subunits underlie slowly inactivating potassium current in rat neocortical pyramidal neurons. *J. Physiol.* 581, 941–960. doi: 10.1113/jphysiol.2007.128454

Gutman, G. A., Chandy, K. G., Grissmer, S., Lazdunski, M., McKinnon, D., Pardo, L. A., et al. (2005). International Union of Pharmacology. LIII. Nomenclature and molecular relationships of voltage-gated potassium channels. *Pharmacol. Rev.* 57, 473–508. doi: 10.1124/pr.57.4.10

Johnston, J., Forsythe, I. D., and Kopp-Scheinpflug, C. (2010). Going native: voltage-gated potassium channels controlling neuronal excitability. *J. Physiol.* 588, 3187–3200. doi: 10.1113/jphysiol.2010.191973

Johnston, J., Griffin, S. J., Baker, C., Skrzypiec, A., Chernova, T., and Forsythe, I. D. (2008). Initial segment Kv2.2 channels mediate a slow delayed rectifier and maintain high frequency action potential firing in medial nucleus of the trapezoid body neurons. *J. Physiol.* 586, 3493–3509. doi: 10.1113/jphysiol.2008.153734

Kapfer, C., Seidl, A. H., Schweizer, H., and Grothe, B. (2002). Experience-dependent refinement of inhibitory inputs to auditory coincidence-detector neurons. *Nat. Neurosci.* 5, 247–253. doi: 10.1038/nn810

Khurana, S., Liu, Z., Lewis, A. S., Rosa, K., Chetkovich, D., and Golding, N. L. (2012). An essential role for modulation of hyperpolarization-activated current in the development of binaural temporal precision. *J. Neurosci.* 32, 2814–2823. doi: 10.1523/JNEUROSCI.3882-11.2012

Khurana, S., Remme, M. W., Rinzel, J., and Golding, N. L. (2011). Dynamic interaction of Ih and IK-LVA during trains of synaptic potentials in principal neurons of the medial superior olive. *J. Neurosci.* 31, 8936–8947. doi: 10.1523/JNEUROSCI.1079-11.2011

Koch, U., Braun, M., Kapfer, C., and Grothe, B. (2004). Distribution of HCN1 and HCN2 in rat auditory brainstem nuclei. *Eur. J. Neurosci.* 20, 79–91. doi: 10.1111/j.0953-816X.2004.03456.x

Kudo, T., Loh, D. H., Kuljis, D., Constance, C., and Colwell, C. S. (2011). Fast delayed rectifier potassium current: critical for input and output of the circadian system. *J. Neurosci.* 31, 2746–2755. doi: 10.1523/JNEUROSCI.5792-10.2011

Kulesza, R. J. Jr. (2014). Characterization of human auditory brainstem circuits by calcium-binding protein immunohistochemistry. *Neuroscience* 258, 318–331. doi: 10.1016/j.neuroscience.2013.11.035

Lehnert, S., Ford, M. C., Alexandrova, O., Hellmundt, F., Felmy, F., Grothe, B., et al. (2014). Action potential generation in an anatomically constrained model of medial superior olive axons. *J. Neurosci.* 34, 5370–5384. doi: 10.1523/JNEUROSCI.4038-13.2014

Lesica, N. A., Lingner, A., and Grothe, B. (2010). Population coding of interaural time differences in gerbils and barn owls. *J. Neurosci.* 30, 11696–11702. doi: 10.1523/JNEUROSCI.0846-10.2010

Li, W., Kaczmarek, L. K., and Perney, T. M. (2001). Localization of two high-threshold potassium channel subunits in the rat central auditory system. *J. Comp. Neurol.* 437, 196–218. doi: 10.1002/cne.1279

Mathews, P. J., Jercog, P. E., Rinzel, J., Scott, L. L., and Golding, N. L. (2010). Control of submillisecond synaptic timing in binaural coincidence detectors by K(v)1 channels. *Nat. Neurosci.* 13, 601–609. doi: 10.1038/nn.2530

Myoga, M. H., Lehnert, S., Leibold, C., Felmy, F., and Grothe, B. (2014). Glycinergic inhibition tunes coincidence detection in the auditory brainstem. *Nat. Commun.* 5:3790. doi: 10.1038/ncomms4790

Rautenberg, P. L., Grothe, B., and Felmy, F. (2009). Quantification of the three-dimensional morphology of coincidence detector neurons in the medial superior olive of gerbils during late postnatal development. *J. Comp. Neurol.* 517, 385–396. doi: 10.1002/cne.22166

Roberts, M. T., Seeman, S. C., and Golding, N. L. (2013). A mechanistic understanding of the role of feedforward inhibition in the mammalian sound localization circuitry. *Neuron* 78, 923–935. doi: 10.1016/j.neuron.2013.04.022

Scott, L. L., Hage, T. A., and Golding, N. L. (2007). Weak action potential backpropagation is associated with high-frequency axonal firing capability in principal neurons of the gerbil medial superior olive. *J. Physiol.* 583, 647–661. doi: 10.1113/jphysiol.2007.136366

Scott, L. L., Mathews, P. J., and Golding, N. L. (2005). Posthearing developmental refinement of temporal processing in principal neurons of the medial superior olive. *J. Neurosci.* 25, 7887–7895. doi: 10.1523/JNEUROSCI.1016-05.2005

Scott, L. L., Mathews, P. J., and Golding, N. L. (2010). Perisomatic voltage-gated sodium channels actively maintain linear synaptic integration in principal neurons of the medial superior olive. *J. Neurosci.* 30, 2039–2050. doi: 10.1523/JNEUROSCI.2385-09.2010

Sheng, M., Liao, Y. J., Jan, Y. N., and Jan, L. Y. (1993). Presynaptic A-current based on heteromultimeric K+ channels detected in vivo. *Nature* 365, 72–75. doi: 10.1038/365072a0

Smart, S. L., Bosma, M. M., and Tempel, B. L. (1997). Identification of the delayed rectifier potassium channel, Kv1.6, in cultured astrocytes. *Glia* 20, 127–134. doi: 10.1002/(SICI)1098-1136(199706)20:2<127::AID-GLIA4>3.0.CO;2-6

Tong, H., Kopp-Scheinpflug, C., Pilati, N., Robinson, S. W., Sinclair, J. L., Steinert, J. R., et al. (2013). Protection from noise-induced hearing loss by Kv2.2 potassium currents in the central medial olivocochlear system. *J. Neurosci.* 33, 9113–9121. doi: 10.1523/JNEUROSCI.5043-12.2013

Wang, L. Y., Gan, L., Forsythe, I. D., and Kaczmarek, L. K. (1998). Contribution of the Kv3.1 potassium channel to high-frequency firing in mouse auditory neurones. *J. Physiol.* 509(Pt 1), 183–194.

Winters, B. D., Jin, S. X., Ledford, K. R., and Golding, N. L. (2017). Amplitude normalization of dendritic EPSPs at the soma of binaural coincidence detector neurons of the medial superior olive. *J. Neurosci.* 37, 3138–3149. doi: 10.1523/JNEUROSCI.3110-16.2017

Zhou, L., Zhang, C. L., Messing, A., and Chiu, S. Y. (1998). Temperature-sensitive neuromuscular transmission in Kv1.1 null mice: role of potassium channels under the myelin sheath in young nerves. *J. Neurosci.* 18, 7200–7215. doi: 10.1523/JNEUROSCI.18-18-07200.1998

Zhuang, J. L., Wang, C. Y., Zhou, M. H., Duan, K. Z., and Mei, Y. A. (2012). TGF-beta1 enhances Kv2.1 potassium channel protein expression and promotes maturation of cerebellar granule neurons. *J. Cell. Physiol.* 227, 297–307. doi: 10.1002/jcp.22735

Conflict of Interest Statement: The authors declare that the research was conducted in the absence of any commercial or financial relationships that could be construed as a potential conflict of interest.

The reviewer JS and the handling Editor declared their shared affiliation

Chapter 3

Arrangement of excitatory synaptic inputs on MSO neurons

3.1 Author contributions

Callan, A. R., Leibold, C. and Felmy, F. **Arrangement of excitatory synaptic inputs on neurons of the medial superior olive.** Manuscript in preparation.

Author Contributions: ARC performed experiments, data analysis, and computational modelling. CL advised computational modelling. FF advised data anlysis. ARC wrote the manuscript with help from FF and CL.

Arrangement of excitatory synaptic inputs on neurons of the medial superior olive

Alexander R. Callan, Christian Leibold & Felix Felmy

Abstract

Neurons of the medial superior olive (MSO) are sensitive to microsecond differences in the arrival time of sound at the two ears. Propagation time of excitatory postsynaptic potentials from distal dendrites to the soma can be long enough to interfere with this process. The propagation times that occur in vivo depend on the position of excitatory synapses on the dendrites. To determine the pattern of excitatory inputs to MSO, we filled axons with biocytin and measured the positions of synaptic boutons on MSO neuron dendrites. Individual axons tended to form multiple boutons, which were distributed along the dendrite. The terminal boutons of these distributed synapses were strongly biased towards the soma. Computational modelling suggested that distributed synapses produce larger but briefer somatic membrane depolarisations than single, localised synapses. Our data show that excitatory inputs to the MSO are organised to minimise the effects of propagation delay, and additionally are beneficial for rapid, high fidelity synaptic signalling.

Introduction

Neurons in the medial superior olive (MSO) can detect variations in auditory stimulus timing with submillisecond resolution (Goldberg and Brown, 1969; Yin and Chan, 1990; Spitzer and Semple, 1995). To pinpoint the source of a low frequency sound, these neurons compute the interaural time difference (ITD)—the difference between the arrival times of a sound at each ear (Grothe et al., 2010). Humans can detect differences in ITDs as low as 10 μs (Klumpp and Eady, 1956). Here we show the pattern of innervation of MSO neurons by excitatory axons contributes to the ability of these cells to detect submillisecond ITDs.

The dendritic trees of MSO neurons typically exhibit a bipolar morphology, with two main dendrites emerging from opposite sides of the cell soma (Rautenberg et al., 2009). Each MSO neuron receives excitatory glutamatergic input from each cochlear nucleus. These excitatory inputs are segregated by side, with the lateral dendrite receiving inputs from the ipsilateral cochlear nucleus, and the medial dendrite receiving inputs from the contralateral cochlear nucleus (Stotler, 1953). In addition, there are inhibitory glycinergic inputs from the lateral and medial nuclei of the trapezoid body, but these inputs are confined to the soma and proximal dendrites (Clark, 1969; Kapfer et al., 2002; Couchman et al., 2012). Detecting the coincidence of the excitatory inputs to each dendrite forms the basis of ITD computation in MSO neurons, although with significant modulation by inhibitory glycinergic inputs (Brand et al., 2002; Pecka et al., 2008; Myoga et al., 2014).

The location of a synaptic input on a neuron can affect the somatic response to that input. Dendritic EPSPs attenuate as they propagate towards the soma, and dendritic filtering causes EPSP halfwidths to increase (Rinzel and Rall, 1974). To counteract attenuation, EPSPs in MSO dendrites tend to be larger the further from the soma they are initiated, so that the somatic response is relatively unaffected by input location (Winters et al., 2017). To counteract dendritic filtering, a process of "voltage-dependent sharpening" actively reduces the halfwidth of propagating EPSPs by means of a somatically biased expression of low-voltage gated potassium channels (Mathews et al., 2010). This process serves to enhance the temporal sensitivity of MSO neurons by reducing the time window available for coincidence detection.

In spite of these adaptations, MSO neurons must nevertheless contend with delays in propagation along the dendrite. Dendritic delays have been demonstrated theoretically for passive dendritic trees by Rall (1967), and have been observed experimentally in MSO neurons in particular by Winters et al. (2017). Bilateral stimulation of an MSO neuron by axons that terminate at different locations on their respective dendrites (a proximal ipsilateral input with a distal contralateral input, for example) would introduce an additional delay into the system.

The impact of EPSP propagation delay would likely depend on the pattern of axonal innervation of MSO dendrites. Previous axonal tracing studies have determined the axonal branching patterns of cochlear nucleus neurons in the MSO, but have not shown how these axons innervate individual MSO neurons (Smith et al., 1993; Beckius et al., 1999) In this study we investigated the pattern of excitatory innervation of MSO neurons by individual axonal branches. We used biocytin filling of cochlear nucleus neurons combined with immunohistochemistry, allowing simultaneous visualisation of pre- and post-synaptic neurons. Additionally, we evaluated the physiological impact of input arrangement in a computational model.

By measuring bouton numbers and positions we show that individual axons typically form multiple synaptic boutons along the dendrites of MSO neurons. Most axons therefore innervate a length of dendrite rather than a specific point. Although boutons are distributed evenly throughout the dendrite, most axons terminate with a synaptic site relatively close to the MSO cell soma. Computational modelling indicates that innervation by distributed synapses could enhance ITD sensitivity in MSO neurons.

Methods

Animals

All experiments were conducted with tissue taken from male and female Mongolian gerbils (*Meriones unguiculatus*). Animal ages are specified for each experiment. All experiments were conducted according to institutional guidelines and regional and national laws. Animal protocols were reviewed and approved by the Regierung of Oberbayern according to the Deutsches Tierschutzgesetz. Prior to experiments, animals were housed with littermates and non-littermates of the same sex and age in temperature controlled rooms with a 12 hour light-dark cycle.

Slice preparation

Animals were anaesthetised with isoflurane (Zoetis) and then decapitated. Brains were quickly removed in dissecting solution at room temperature. Dissecting solution contained (in mM) 65 sucrose, 25 NaCl, 27 $NaHCO_3$, 1.25 NaH_2PO_4, 2.5 KCl, 25 glucose, 0.4 ascorbic acid, 3 myo-inositol, 2 Na-

pyruvate, 3 $MgCl_2$, and 0.1 $CaCl_2$. The solution was bubbled with carbogen consisting of 95% oxygen-5% carbon dioxide to saturate with oxygen and to bring the pH to 7.4. The brainstem was isolated and submerged in dissecting solution, and 100-120 μm horizontal sections (i.e. parallel to ventral surface) were taken with a VT1200S vibratome (Leica). Slices were transferred to recording solution bubbled with carbogen and warmed in a water bath to 36°C. Recording solution contained (in mM) 125 NaCl, 25 $NaHCO_3$, 1.25 NaH_2PO_4, 2.5 KCl, 25 glucose, 0.4 ascorbic acid, 3 myo-inositol, 2 Na-pyruvate, 1 $MgCl_2$, and 1.2 $CaCl_2$. After 30 minutes, the slice incubation chamber was removed from the water bath, and slices were kept at room temperature until use.

Dual somatic and dendritic recordings

Male and female gerbils aged postnatal day (P) 43–65 were used for dual whole cell somatic and dendritic current clamp experiments. Slices were placed in a recording chamber and constantly perfused with carbogenated recording solution maintained at 34–36°C with both in-line and bath heating (Warner Instruments). MSO neurons were visualised with a 60x water-immersion objective with an upright microscope (BX51W1, Olympus). The MSO itself was first identified with a 4x water-immersion objective. The microscope was equipped with gradient contrast illumination, a 1.4 NA oil-immersion condenser, and a TILL Photonics imaging system (FEI Munich GmbH) consisting of a charged-coupled device camera (Retiga 2000DC) and a monochromator.

Electrodes were pulled from filamented, borosilicate glass capillaries (0.86 mm inner diameter, 1.50 mm outer diameter, BioMedical Instruments) using a horizontal puller (DMZ Universal Electrode Puller, Zeitz Instruments) and heat polished. Recording electrodes were back-filled with internal recording solution containing, (in mM) 145 K-gluconate, 4.5 KCl, 15 HEPES, 2 Mg-ATP, 2 K_2-ATP, 0.3 Na_2-GTP, 7.5 NA_2-phosphocreatine, 5 K-EGTA, 0.05 Alexa Fluor 488/568/594. The pH was adjusted to 7.25 with KOH. The liquid junction potential of approximately 16 mV was corrected offline.

Recordings were made using an EPC 10/2 patch clamp amplifier (HEKA Elektronik) and the associated Patch Master acquisition software. Data were acquired at 100 Hz and low-pass filtered at 3 KHz. After estimating the series resistance, the bridge balance was set to 100%. For all data reported here, the series resistance was below 20 MΩ during the recordings.

Neurons with at least one visible dendrite were patched first with an electrode at the soma, and subsequently at the dendrite. Alexa Fluor dyes of sufficiently difference emmission wavelengths were used for the somatic and dendritic electrodes respectively. This allowed for visual confirmation that both electrodes had access to the same cell. For some neurons, the second recording site was also at the soma. For all recordings, electrode tip resistance in bath was 7–10 MΩ. Electrodes of similar tip resistance were used for both somatic and dendritic recordings because one of the aims was to compare the membrane time constant between the two recording sites. The capacitance of glass microelectrodes leads to filtering of the signal recorded from the neuron. So that measurements of the membrane time constant could be compared between recording sites, the capacitance of the two electrodes should be similar. Electrodes with similar resistance that are made on the same puller should have comparable geometry and therefore comparable capacitance.

Axon filling and immunohistochemistry

Axon filling with biocytin was performed following Seidl and Rubel (2016). Male and female gerbils aged P21 to P30 were used for axon tracing and immunohistochemistry. Animals were anaesthetised with isoflurane (Zoetis) and brains were quickly removed in ice cold artificial cerebrospinal fluid (ACSF). ACSF contained (in mM) 125 NaCl, 25 $NaHCO_3$, 1.25 NaH_2PO_4, 2.5 KCl, 25 glucose, 0.4 ascorbic acid, 3 myo-inositol, 2 Na-pyruvate, 1 $MgCl_2$, and 2 $CaCl_2$. Brains were affixed to a cold sylgard-based dish by pins through the cerebrum, and submerged in ice-cold ACSF. Brains were positioned so that one cochlear nucleus nucleus faced upwards. Under a dissecting microscope, a crystal of biocytin was placed directly on the cochlear nucleus. The brain was then removed to an incubation chamber containing ACSF bubbled with carbogen, and left to incubate at room temperature for 2–2.5 hours.

Following incubation, brains were immediately submerged in 4% paraformaldehyde (PFA) in 0.02 M phosphate-buffered saline (PBS) for 12–14 hours. Brains were subsequently washed three times for at least 10 minutes in PBS. Slices of thickness 120 or 160 μm were made with a VT1200S Vibratome (Leica).

Free floating slices were incubated in blocking solution containing 0.1% v/v saponin, 1% w/v bovine serum albumin, and 1 or 1.5% v/v Triton X-100 in 0.02% PBS. Subsequent to blocking, slices were incubated in Alexa Fluor 488 conjugated streptavadin (Sigma) at 1:500 dilution along with primary antibodies for 46 to 72 hours. See Table 1 for details of all primary antibodies used. All primary and secondary antibodies were diluted in blocking solution. Slices were subsequently washed three times for 30 minutes each time in blocking solution, then incubated for 48 to 72 hours in fluorophore-conjugated secondary antibodies. See Table 2 for the list of all secondary antibodies used. Following incubation in secondary antibodies, slices were washed twice for 20 minutes in blocking solution then three times for twenty minutes in 0.02 mM PBS. Washed slices were mounted on gelatine-coated glass slides with Vectashield mounting medium (Vector Laboratories) under glass coverslips sealed with nail polish.

Table 1: Primary antibodies

Antigen	Host	Type	Dilution	Company	Cat. No.
MAP2	Chicken	Polyclonal IgY	1:500	Acris	TA336617
VGluT1	Guinea Pig	Polyclonal	1:2000	Synaptic Systems	135 304
GlyT2	Rabbit	Polyclonal	1:1000	Synaptic Systems	272 003

Table 2: Secondary antibodies

Antigen	Conjugate	Host	Dilution	Company	Cat. No.
Chicken	Cy3	Donkey	1:200	Dianova	703-166-155
Guinea Pig	Alexa 647	Donkey	1:100	Dianova	706-605-148
Rabbit	AMCA	Donkey	1:100	Dianova	711-155-152

Microscopy and image analysis

Staining of axons and other targets was initially assessed using an upright epifluorescence microscope (Eclipse 60i, Nikon, or Axio Imager.M1, Zeiss) with 10x, 0.3 NA and 20x, 0.5 NA air objectives. Successfully stained sections containing one or both MSO nuclei were subsequently used for confocal imaging.

Images of stained tissue were acquired using a Leica TCS SP5 confocal microscope system. For line scan analysis of staining in the MSO, single images were acquired using a 20x, 0.7 NA generalist immersion objective, adjusted for use with glycerol. Images were averaged 6 to 8 times by row of the image. Higher magnification images were acquired with a 63x, 1.3 NA glycerol immersion objective. Image stacks were acquired with a distance between sections approximately equal to the the width of one pixel of a section. Typically, images of 1024 x 1024 pixels were created, giving a pixel size of 240.50 nm with a distance of 251.77 nm between sections. All images in stacks were averaged 4 to 6 times by row. The number of images in a stack was chosen based on the depth of histological staining and positions of dendrites and axons, and so was different for each stack. These stacks were used for following the path of axons in brain slices. Chromatic abberations in image stacks were corrected using custom scripts in ImageJ.

Initial image processing to generate image stacks by accquisition channel was conducted using ImageJ. Line scan analysis was conducted using Igor Pro (WaveMetrics). Measurements of axons and dendrites were obtained using MetaMorph image analysis software (Molecular Devices). Measurements were initially recorded in Microsoft Excel and were subsequently analysed with Python. Details of analysis are provided where relevant in the results section.

Computational modelling

A minimal, multi-compartmental model of an MSO neuron was simulated using MATLAB. The model consisted of a somatic compartment sandwiched between 10 dendritic compartments on each side. Each compartment was cylindrical with a length of 30 μm for the somatic compartment and 15 μm for each dendritic compartment to approximate the length or MSO dendrites (Rautenberg et al., 2009). The somatic compartment had diameter 15 μm

and the dendrites tapered linearly, with the most proximal compartment having diameter 4.4 μm, and the most distal 1.7 μm. The specific axial resistance connecting the compartments was taken as 200 Ωcm, and the specific membrane capacitance as $C_m = 0.9$ μF/cm^2 (Gentet et al., 2000). The resulting total cell capacitance was approximately 40 pF.

The membrane potential, V, of each compartment was modelled following a Hodgkin-Huxley type equation as follows:

$$C_m \frac{dV}{dt} = -(I_{\mathrm{KLT}} + I_{\mathrm{HCN}} + I_{\mathrm{leak}} + I_{\mathrm{axial}} + I_{\mathrm{syn}})$$

where I_{KLT} is a low threshold potassium current modelled according to Mathews et al. (2010), I_{HCN} is a HCN channel current modelled according to Baumann et al. (2013), using the parameters for dorsal MSO neurons, and $I_{leak} = 0.05$ mS/cm^2. The axial current, I_{axial}, was determined as follows:

$$I^i_{\mathrm{axial}} = \frac{V_{i-1} - V_i}{R^{i-1,i}_{\mathrm{axial}}} + \frac{V_{i+1} - V_i}{R^{i+1,i}_{\mathrm{axial}}}.$$

Excitatory post-synaptic current, I_{syn} was modelled according to Lehnert et al. (2014) as an Ohmic current with the time course of synaptic conductance modelled as the following double exponential function:

$$G_{\mathrm{exc}}(t) = g_{\mathrm{exc,max}} \frac{(1 - e^{-t/1.0})^{1.3} e^{-t/0.27}}{\max((1 - e^{-t/1.0})^{1.3} e^{-t/0.27})}.$$

The peak conductance of the low threshold potassium current, in mS/cm^2, was dependent on distance from the soma centre according to:

$$G_{\mathrm{KLT}}(x) = 57(1 + 1.5e^{-x/22})$$

with x in μm . For the HCN current the peak conductance was uniform throughout the cell at 1.26 mS/cm^2. The conductance amplitudes were chosen to fit the physiological resting potential and input resistance as measured at the soma in MSO neurons. The reversal potential of potassium was taken as -90 mV, of the HCN current as -35 mV, of the leak current as -70 mV, and of excitatory synaptic input as 0 mV. Although there is evidence for high threshold potassium currents in MSO neurons, which can

influence membrane response properties (Nabel et al., 2019), the essential features of MSO membrane behaviour can be replicated with only low threshold potassium currents (Mathews et al., 2010; Winters et al., 2017).

Results

Propagation delay in MSO dendrites

To verify the presence of propagation delay, we performed dual somatic and dendritic patch clamp recordings of MSO neurons from Mongolian gerbils aged 45 to 65 days (Figure 1A). Dendritic electrodes were positioned up to 104 μm from the soma centre. Neurons were stimulated with a triangular current pulse to induce an EPSP-like membrane depolarisation. The propagated simulated EPSP was measured at both electrodes, and the difference in the timing of the waveform was measured at 60% of the peak amplitude. The notable variance in these measurements is most likely due to noise in the recordings, which can artificially shift the apparent 60% peak time of the EPSP-like waveform, and imperfect capacitance compensation, which can cause an artificial shift in the time course of the waveform.

We verified the presence of propagation delay in MSO neurons, with a delay of 100 μs for dendritic stimuli at approximately 60 μm from the soma, according to a linear fit of the data (Figure 1B). Based on the slope of the linear fit, we determined a propagation velocity of approximately 0.6 m/s, somewhat slower than the 0.8 m/s velocity determined by Winters et al. (2017). Note however that we measured the relative timing of EPSPs at 60% of maximum amplitude to avoid a stimulation artifact present in some recordings, whereas Winters et al. (2017) measured at 50% of maximum. Since we used direct current stimulation, we could repeat the experiments with somatic current stimulation. We found that the propagation velocity was not significantly different for simulated EPSPs propagating in the somato-dendritic direction (Figure 1B), which was also the case for EPSPs measured in younger animals (P16-25) by Winters et al. (2017).

To test if dendritic propagation delay might affect ITD tuning, we constructed a multi-compartmental model of an MSO neuron. We used a simplified dendritic geometry (see Methods, Figure 2A), which accurately reproduced propagation delays measured experimentally (Figure 2B). Propagation delay was measured in the model as the relative timing of

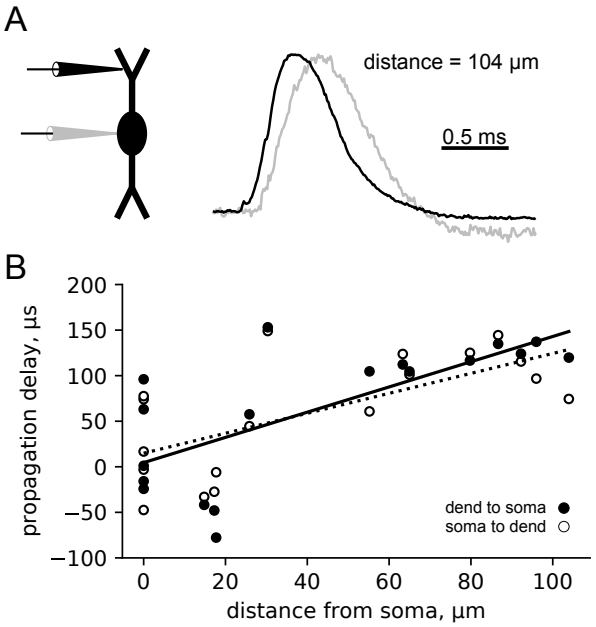

Figure 1. **A.** Whole cell patch clamp of MSO neurons shows a latency in response between stimulating electrode (black) and recording-only electrode (grey)—the propagation delay. Example trace magnitudes are normalised for comparison of timing. **B.** Propagation delay increased systematically with dendritic electrode recording distance from soma. Similar delays were observed with somatic stimulation and propagation towards distal dendrites.

50% maximum amplitude of the propagating EPSP between the stimulated compartment and the somatic compartment. We simulated trains of bilateral excitatory post-synaptic conductances with different positions on the dendrites, at a range of amplitudes and frequencies. We simulated synaptic input at the distal dendrites, at the proximal dendrites, or offset, with one distal and one proximal input (Figure 2A). The dual distal and dual proximal inputs varied only in amplitude, but when the inputs were spatially offset, the peak of the response function was shifted by up to 150 μs (Figure 2C & D). The magnitude and direction of the shift varied depending on the strength and the frequency of synaptic input (Figure 2D). These results suggest synaptic position could affect the ITD response function of MSO neurons.

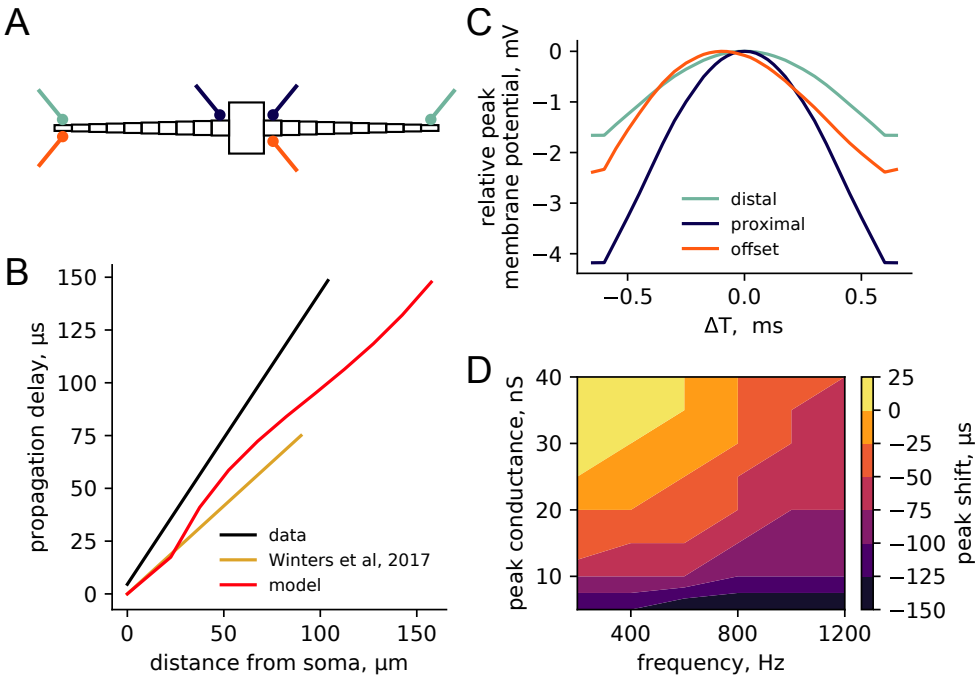

Figure 2. **A.** Schematic of model MSO neuron. Three synaptic input patterns indicated, coloured according to the legend in C. **B.** The model cell reproduced the propagation delay seen in MSO neurons in vitro. **C.** Model response to bilateral synaptic inputs for three different synaptic configurations. Peak conductance = 10 nS, frequency = 800 Hz. Peak shift = -100 μs. For offset inputs, ΔT is the time of the proximal input relative to the distal input (right dendrite relative to left dendrite according to A). **D.** The peak shift in the response function over the range of conductance amplitudes and input frequencies, i.e. the peak time of the orange curve in Panel C relative to zero.

Biocytin filling of excitatory inputs to MSO

Given the propagation delay, the precise arrangement of synaptic inputs would likely be important for ITD computations in MSO neurons. To determine this arrangement, we filled cells in the cochlear nucleus with biocytin and stained the filled cells with fluorophore-conjugated streptavidin. For these anatomical experiments we used gerbils aged 21 to 30 days. MSO neurons were visualised by staining for microtubule associated protein 2 (MAP2). Additionally, tissue slices were co-stained for vesicular glutamate transporter 1 (VGluT1) to visualise excitatory synaptic terminals. Low magnification images show axons projecting to the MSO (Figure 3A). Upon approaching the dendritic field of MSO neurons, axons form many branches, which do not continue past the MSO cell somata.

Our qualitative observations were reinforced by linescans of fluorescence levels parallel to the path of the axons (Figure 3B). The location of peak fluorescence was determined by fitting a Gaussian function to the data for each image. The peak of the MAP2 Gaussian fit was defined as zero.

Biocytin-associated fluorescence peaks earlier (i.e. more laterally) than MAP2-associated fluorescence and decreases past the peak of MAP2 (Figure 3C & D). This result suggests axons terminate on the nearer dendrite (i.e. the lateral dendrite for the ipsilateral MSO), which was also apparent in higher magnification images, and is expected from previous studies (Stotler, 1953). Some axons terminated past the somatic layer on the opposite dendrite (medial dendrite for the ipsilateral MSO), although these were the exception and were not considered further for detailed analysis. They may, however, contribute to the fluorescent signal that continues past the somatic layer into the medial dendritic feld of the MSO. This signal may also be partly caused by axons that cross the somatic layer then return to the lateral dendritic field, and thus ultimately form synapses on lateral dendrites. The convoluted route taken by some spherical bushy cell axons has been observed previously (Beckius et al., 1999). In addition, some axons could be observed passing through the MSO and continuing towards the midline (Figure 3A).

The position of VGluT1 fluorescence was similar to that of MAP2, with both having the same peak position (Figure 3D). The halfwidths of Gaussian fits were, however, somewhat wider for VGluT1 than for MAP2 (141 μm vs. 106 μm, Mann-Whitney U test p=0.03, Figure 3E), indicating a broad distribution of excitatory synapses to the distal dendrites.

The experimental approach we used unspecifically fills many cells in the cochlear nucleus (Seidl and Rubel, 2016). Many putative synaptic boutons were visible on these terminating axons in close apposition to MSO neurons. Bouton identification was based on size and shape. Distinct varicosities in the axon, which were clearly larger than the neighbouring axon, and were adjacent to a MAP2 stained MSO neuron, were assumed to be synaptic boutons. Orthogonal optical slies through the image stack were inspected to ensure a bouton could be unambiguously identified as an extension of a particular axon. Only axons where the axon and all of its associated synaptic boutons could be clearly separated from surrounding axons were used for measurements. Biocytin filled boutons commonly overlapped with VGluT1 staining (examples indicated in Figure 4A). Overlap of boutons with GlyT2

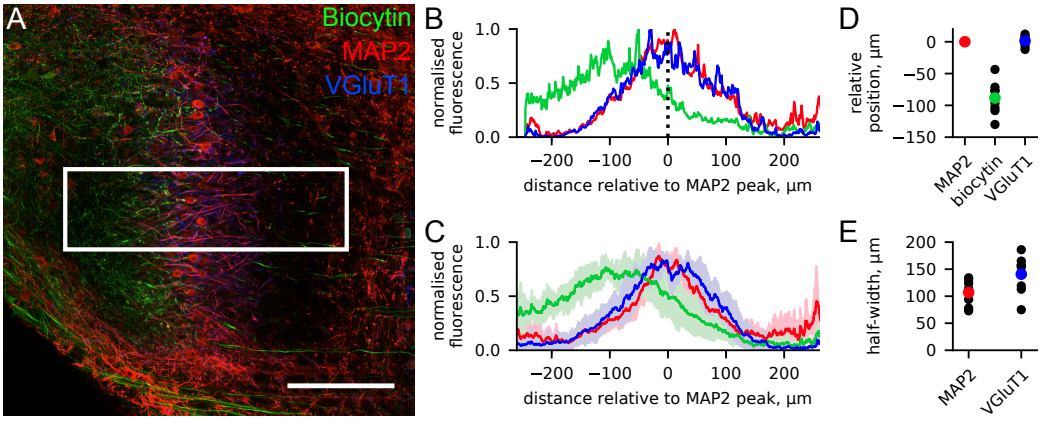

Figure 3. **A.** Single optical section showing the entire MSO, excitatory inputs from the cochlear nucleus and staining for VGluT1. The boxed area was used for linescans (left to right, averaged across the vertical axis). **B.** Normalised fluorescence values for MSO image shown in A. Colours correspond to those in A. **C.** Averaged values from 8 images from 4 animals. **D.** Peak fluorescence values relative to the MAP2 peak. Peaks are determined by fitting a Gaussian function to the fluorescence measurements. **E.** Halfwidths of Gaussian functions fit to measurements from each image.

staining was never observed, consistent with glycinergic inputs originating in the medial nucleus of the trapezoid body but not in the cochlear nucleus. Additionally, we never observed a pattern of somatic innervation like that seen in previous studies of glycinergic innervation of MSO neurons by the medial nucleus of the trapezoid body (Werthat et al., 2008; Couchman et al., 2010).

To further verify that we were correctly identifying excitatory synapses, we looked more closely at individual boutons. As immunohistochemical staining does not reliably stain all the target protein present in a tissue sample, we produced average images from 60 synaptic boutons from three gerbils. Regions of interest, centred on synaptic boutons, were selected from three channel images and the average pixel intensity of these 60 images was calculated to produce an "average" bouton. These tissue samples had been counterstained for VGluT1 and MAP2, and average images were also generated from these channels from the specified regions of interest. Many, but not all of the synaptic boutons showed overlapping VGluT1 staining (Figure 3B). The average VGluT1 stain was very similar to the average bouton, except for having more staining throughout the image because VGluT1 stains many more synaptic boutons than are filled with biocytin.

The average MAP2 staining showed a darker patch in the centre of the image due to boutons commonly appearing adjacent to dendrites and somata. Repeating the selection and averaging process with stretches of axon that did not include boutons showed a random pattern in the VGluT1 staining, with no correspondence to the averaged filled axon (Figure 3B). Repeating this process with tissue co-stained for GlyT2 showed no overlap between GlyT2 staining and boutons (Figure 3C). Instead, the average GlyT2 image shows a dark patch corresponding to the location of the average bouton. Overall, this analysis shows that we could correctly identify excitatory synaptic boutons terminating on MSO neurons.

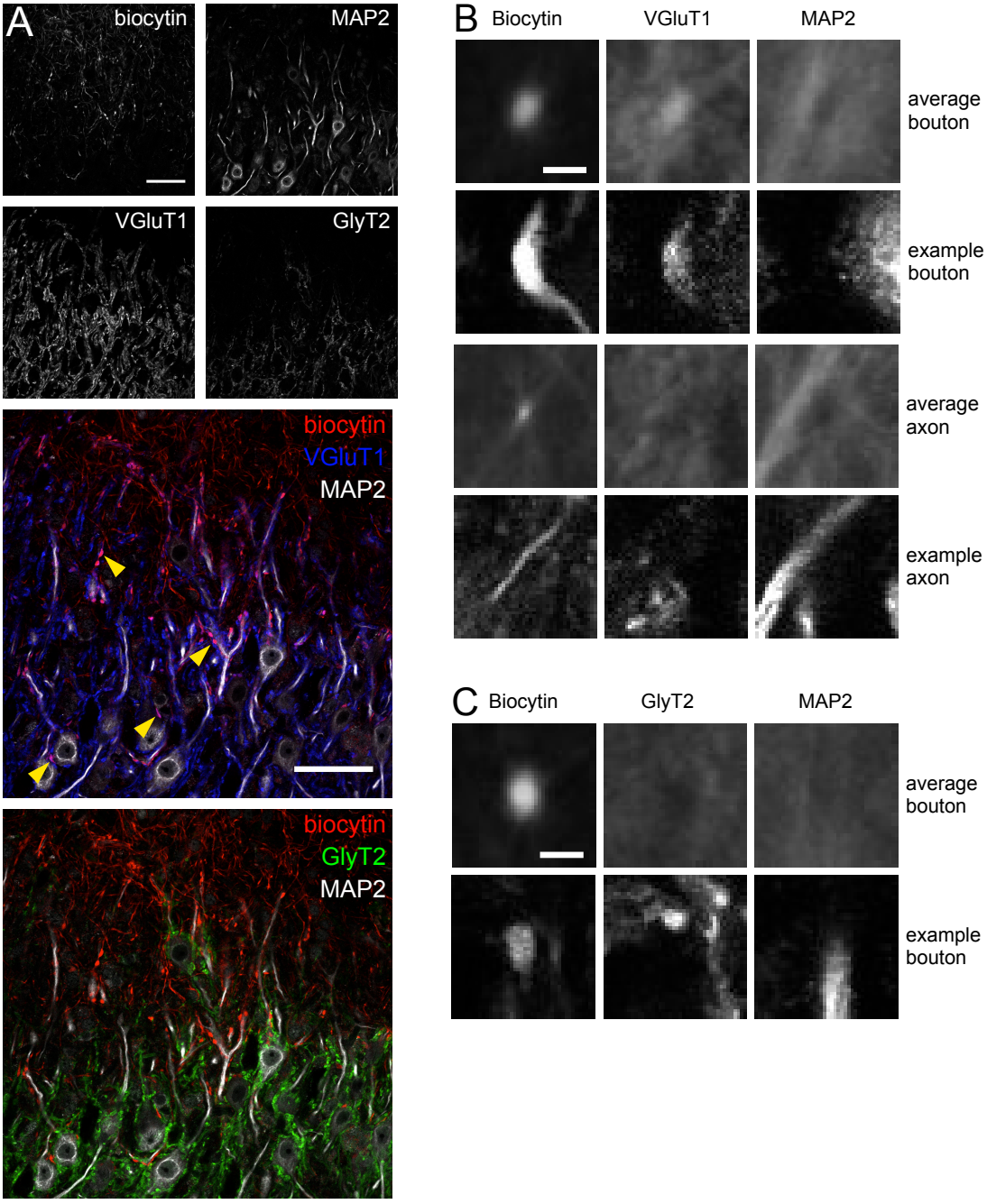

Figure 4. **A.** Slices from biocytin treated brains were counterstained with MAP2, VGluT1 and GlyT2. Overlay of biocytin and VGlut1 staining was visible at putative synaptic boutons (indicated by yellow arrowheads). No colocalisation of biocytin and GlyT2 was observed. Scale bars = 50 μm. **B.** Average images of 60 putative boutons indicates colocalisation with VGluT1 (1st row). Example bouton (2nd row) apposes the soma of an MSO neuron. Average images of bouton-free axon segments indicate no colocalisation with VGluT1 (3rd row, example in 4th row). Scale bar = 3 μm. **C.** Repeating with a separate set of 60 boutons indicates no colocalisation with GlyT2 (upper). Bouton is apposed to a dendrite (lower). Scale bar = 3 μm.

Pattern of excitatory input to MSO neurons

We next sought to quantify the pattern of synaptic boutons formed by individual axonal branches. We identified 55 terminal axon branches in tissue taken from 6 gerbils, each of which formed one or more synaptic boutons in apposition to MSO dendrites (Figure 5A & B). Each of the axons we identified approached the dendrite, then ran adjacent to it for some distance in the dendro-somatic direction before terminating with a terminal bouton closer to the soma. Only those axons where we could identify the point at which the axon first approached the dendrite were included in our measurements. Axons were only included if their associated dendritic branch could be followed to the limit allowed by the MAP2 staining. If a dendrite was cut off at the limit of the image stack, axons associated with that dendrite were not included in our measurements.

Most axons (49 out of 55) formed boutons along the dendrite in addition to the terminal bouton, with a median of 4 boutons for all 55 axons (Figure 5C). We measured the length of the MSO dendrite spanned by boutons from a single axon, that is, the distance along the dendrite between the terminal bouton and the most distally located bouton. This distance varied from the size of the bouton for single bouton axons, up to 120 μm. The proportion of the dendrite spanned by boutons from a single multi-bouton axon varied unsystematically, with no clear peak in the distribution of values (Figure 5D). Although boutons from single axons could span large portions of the dendrite, axons tended to terminate with a terminal bouton at the soma or proximal dendrite. The majority (39 out of 54, one unknown where soma was outside image) of terminal boutons occurred within 40 μm of the soma centre (Figure 5E). An overview of these data, showing normalised positions of all boutons, is given in Figure 6.

The length of dendrite spanned by boutons from a single axon was greater for axons with more boutons (Figure 7B, linear regression, $R^2 = 0.46$, $p = 9.2e^{-8}$). Boutons were not, however, evenly spaced throughout this length. Clusters of boutons were common (e.g. Figure 7A), as were long stretches of axon between clusters. The distribution of interbouton distances was skewed towards smaller values (Figure 7C). These data were not well modelled as a Poisson process (Kolmogorov-Smirnov test, comparison to

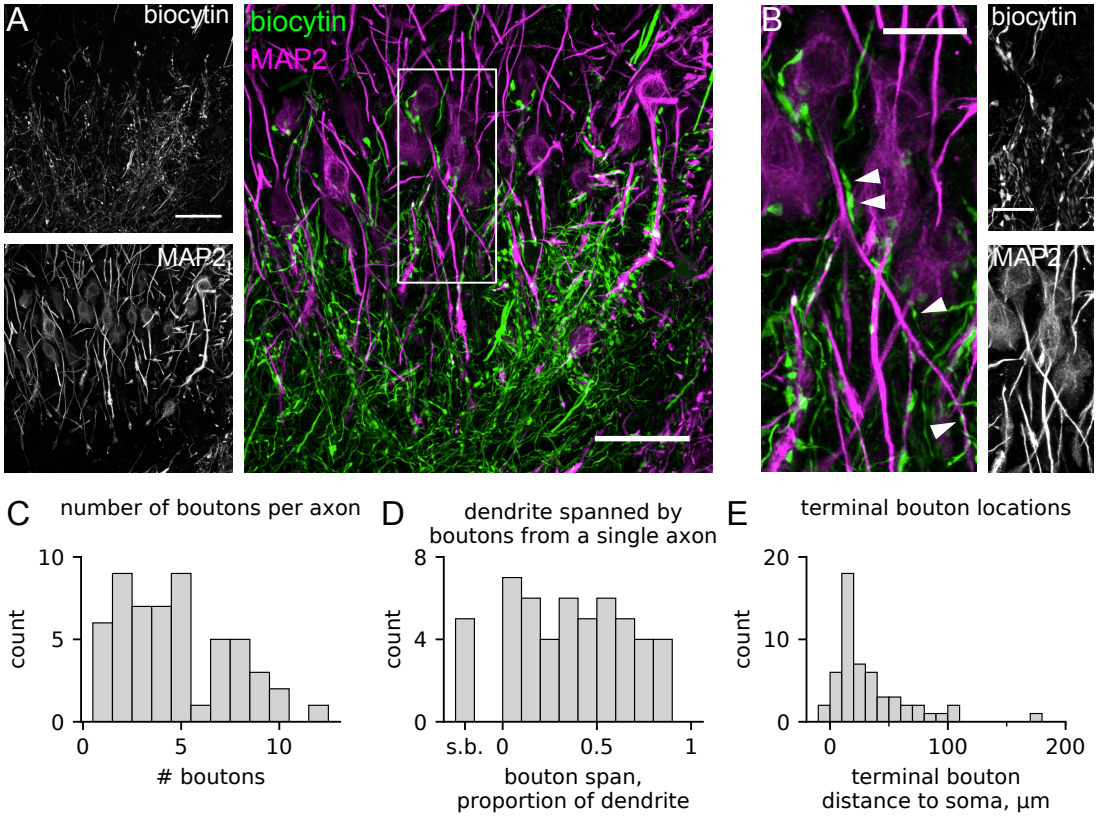

Figure 5. **A.** Low power image showing many MSO neurons and synaptic boutons. Scale bar = 50 μm **B.** Enlarged view of boxed area in A. Synaptic boutons along a single axon are idicated with arrowheadss. Scale bar = 20 μm. **C.** Number of boutons per axon. Median = 4. **D.** Proportion of dendrite spanned by boutons from each axon. "s.b". indicates axons with a single bouton. Median = 0.41 for axons with at least two boutons. **E.** Position of terminal bouton in absolute distance from soma centre. Median = 25 μm.

exponential cumulative density function, $p = 5.1e^{-5}$). This suggests that the distances between boutons are not random but instead depend on the locations of other boutons on the axon.

Axons innervating MSO neurons typically "followed" the dendrite. The terminal axonal branches we observed were positioned parallel to the dendrites they innervated and rarely made excursions away from the dendrite (example in Figure 8A). We compared the distance on the dendrite spanned by the boutons from one axon to the distance on the axon itself between the initial and terminal boutons. These values were statistically indistinguishable (Mann Whitney U test, $p = 0.45$). Least squares linear regression indicated the dendritic span was a good predictor of the axonal

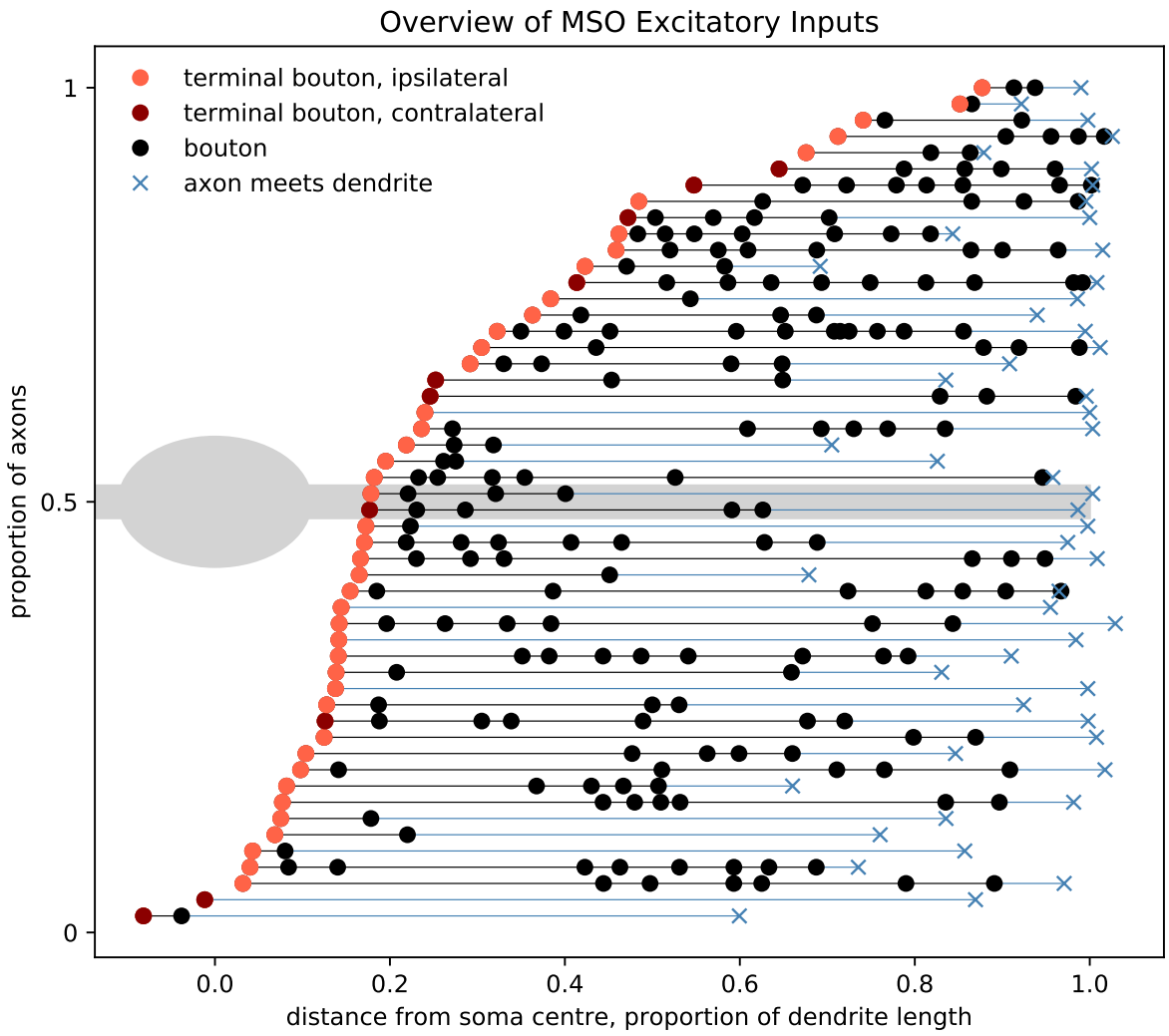

Figure 6. Overview of axon measurements, normalised to the denritic length, which is measured from the soma centre. For branching axons (see Figure 9), all boutons are shown on a single line.

span ($slope = 1.0, r^2 = 1.0, p = 1.5e^{-53}$, Figure 8B). Upon meeting the dendrite, axons typically ran adjacent to the dendrite for some distance before the first bouton. We determined the proportion of the remaining dendrite, distal to the most distal bouton of a particular axon, for which

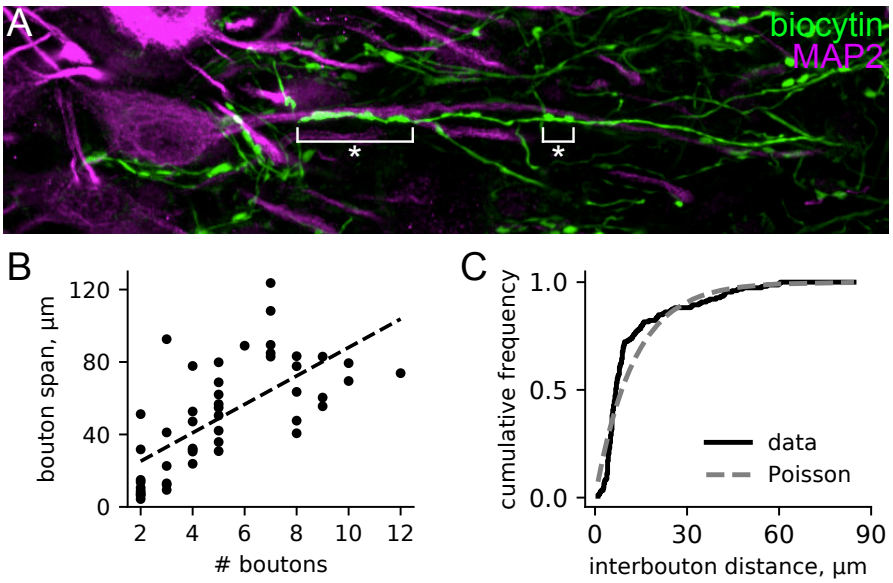

Figure 7. A. Synaptic boutons often occur in clusters. Examples are marked with *. **B.** The span of boutons along the dendrite can be explained to some extent by number of boutons. Least squares linear regression, $R^2 = 0.46, p = 9.2e^{-8}$. **C.** Cumulative frequency of distances between boutons could not be modelled as a Poisson process (Kolmogorov-Smirnov test, $P = 5.1e^{-5}$), suggesting boutons are not randomly spaced relative to other boutons.

that axon ran parallel to the dendrite, which we termed the "tail". Tails covered the full range of possible values, included some cases in which the axon formed a synaptic bouton immediately upon contacting the dendrite, with a median length of 76% of the remaining dendritic length (Figure 8C). The distribution of these values shows a tendency for axons to converge on dendrites at relatively distal dendritic positions, and then run parallel for some distance before forming the first bouton (see also Figure 6). Tail lengths did not vary systematically with the span of the corresponding axons' synaptic boutons on the dendrite (Figure 8D).

Terminal axonal branches exhibit minimal branching. Of the axons we identified, 13 out of 55 possessed additional branches, all of which exclusively targetted the same dendrite as the main branch of the axon (example in Figure 9A). In most cases (10 out of 13), only one additional branch was observed (Figure 9B). Branches also tended to be relatively short, with a median length of 9 μm, or 12% of the total length of axon adjacent to the dendrite. Branch lengths did not correlate with the overall length that axon

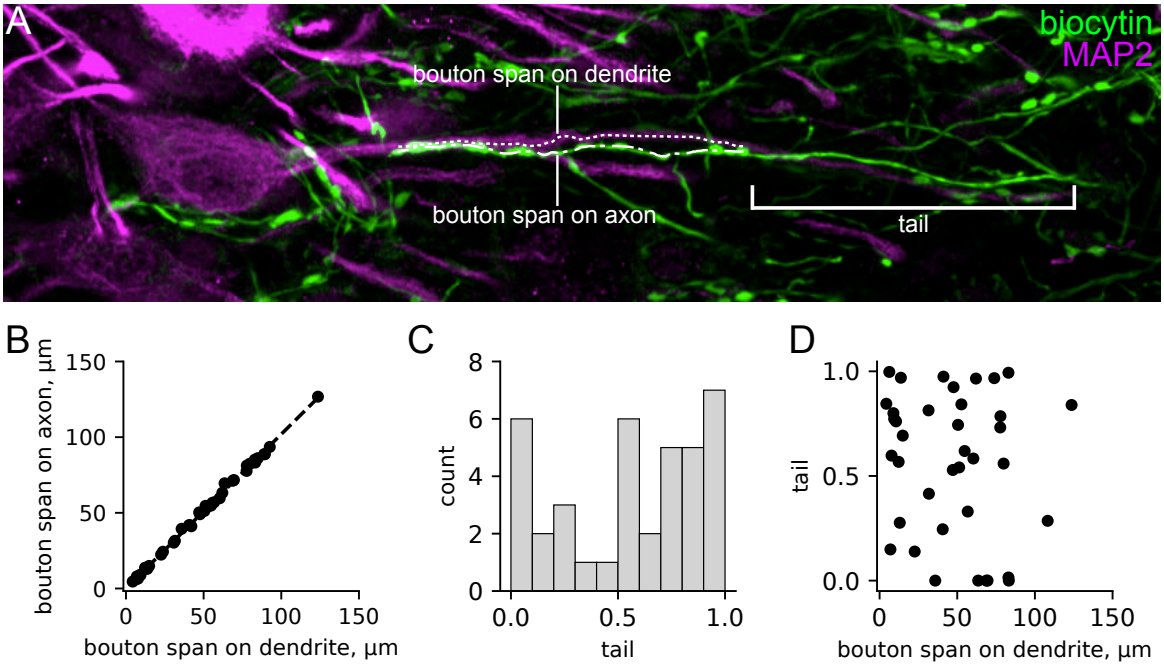

Figure 8. A. Axons tend to follow dendrites closely. The spans of boutons as measured on the dendrite and on the axon are indicated. The length of axon between the first axo-dendritic contact point and the first bouton is referred to as the "tail". **B.** The span of boutons as measured on the afferent axon was almost identical to the span on the dendrite. Least squares linear regression $slope = 1.0, r^2 = 1.0, p = 1.5e^{-53}$. **C.** Distribution of tail lengths as proportions of dendritic length that was distal to the first bouton. **D.** There was no relationship between tail length and bouton span. Least squares linear regression $p = 0.38$.

was adjacent to the dendrite (Figure 9C). We did observe axonal branches targetting other dendrites, as expected from previous studies (Smith et al., 1993; Beckius et al., 1999), but the branch points in these cases occurred prior to the axon innervating any dendrite with synaptic boutons.

We also sought to determine the overall distribution of boutons throughout the MSO dendrite. For this analysis, we identified MSO dendrites and measured the position of each bouton on that dendrite, regardless of whether we could follow the associated axons (e.g. in Figure 10A). We measured the positions of 241 boutons from 18 ipsilateral neurons and 164 boutons from nine contralateral neurons. The number of boutons per dendrite was between five and 29 (median = 15). This is almost certainly an underestimate of the true number of boutons for each dendrite, given the unlikelihood that all cochlear nucleus neurons were filled with

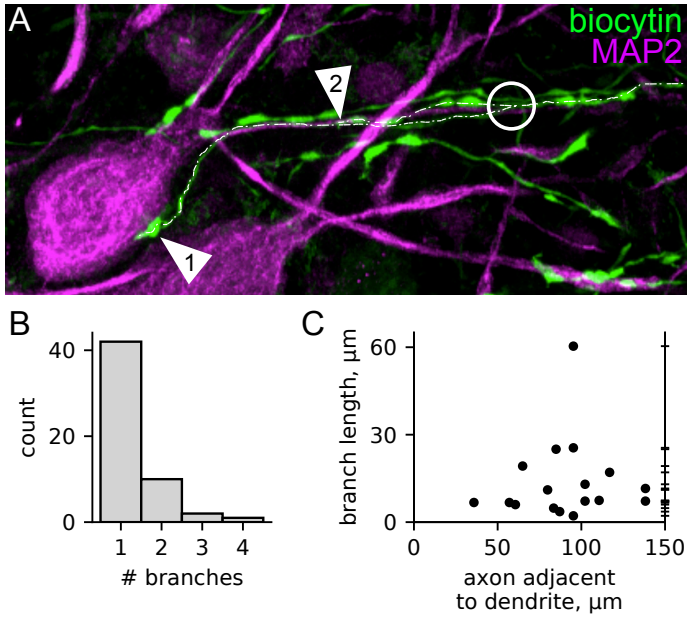

Figure 9. A. Example of a branching axon, which has been traced over with a dashed line. Terminal boutons of each branch are indicated with arrows 1 and 2, and the branch point is circled. **B.** Axon branching was visible in 20% of measured axons. # branches is total number of branches, so one branch means zero branch points. **C.** Distribution of branch lengths is visualised on the right axis. Branch lengths did not relate to the total length of axon adjacent to the dendrite. Least squares linear regression $p = 0.78$.

biocytin. Nevertheless, combining measurements from many dendrites should represent the distribution of all boutons on a single dendrite. Position was measured as distance from soma centre, and normalised to the length of the dendrite. Two boutons were included that were positioned on the opposite side the soma centre (and so have a negative position) because they were clearly associated with axons innervating the dendrite under inspection. For each neuron, only the boutons along the longest visible dendritic branch were included in the analysis, ignoring boutons on other branches. For these single dendritic branches, the distribution of boutons exhibits an approximately uniform distribution (Figure 10B). Additionally, the distribution did not differ between ipsilateral and contralateral MSO dendrites (Mann-Whitney U test, p = 0.44). Given that all MSO neurons exhibit some degree of dendritic branching (Rautenberg et al., 2009), we expect the overall number of boutons on the dendrite is greater distal to dendritic branch points.

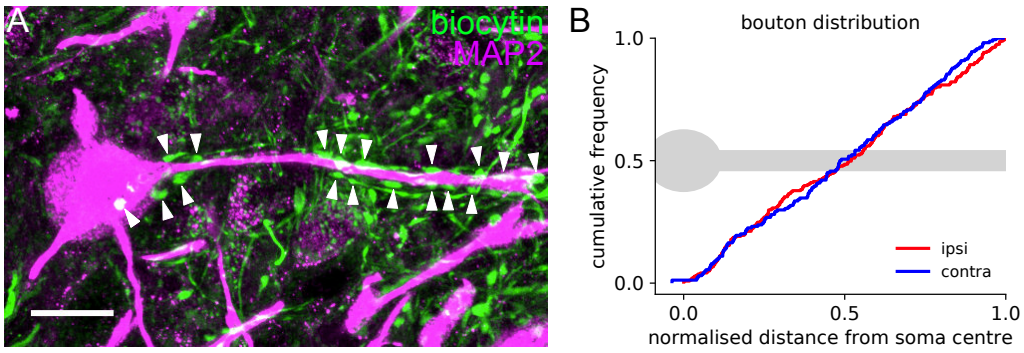

Figure 10. **A.** For some MSO neurons, the positions of all boutons were measured, indicated with white arrows in example given. **B.** Cumulative plot shows similar, uniform distributions of boutons along the MSO dendrite (indicated in grey) for both ipsilateral and contralateral inputs. Median = 0.52 and 0.50 respectively. Mann-Whitney U test, $p = 0.44$.

Functional significance of distributed excitatory inputs

We used our model MSO neuron to investigate how the excitatory input pattern might influence the physiological function of these neurons. We first looked at whether distributing synaptic input over a larger extent of the dendrite would affect the somatic response. We used two general configurations, one where the synaptic input was localised to just one compartment, and one where it was distributed across each compartment distal, and including that compartment (Figure 11A). The total synaptic conductance was identical between localised and distributed versions of the model at 37 nS (Couchman et al., 2010). For the distributed synaptic input, the conductance was divided equally between the compartments receiving synaptic stimulation. For both input configurations the model was simulated twice with different simulated axonal conduction velocities. A "fast" version with conduction velocity = 10 m/s was used to simulate the presence of myelin (Smith et al., 1993; Sinclair et al., 2017), while a "slow" version with conduction velocity = 1 m/s was used to simulate an unmyelinated axon (Weidner et al., 1999; Meeks and Mennerick, 2007). The onset timing of the synaptic conductance was the same for all versions of the model.

Distributing the synaptic conductance along the dendrite resulted in a distinctly different EPSP waveform at the soma (Figure 11A). Larger EPSPs were seen in every dendritic compartment for both fast and slow axonal conduction velocities (Figure 11B & C). Distributed synapses differed from

localised synapses according to three different EPSP properties. Distributed synapses tended to produce somatic EPSPs that were slightly larger (up to 1.7 mV) and briefer (up to 170 μs smaller halfwidth) compared to synaptic input localised to single compartments (Figure 11D1 & 2). Additionally, the peak of the somatic EPSP occurred up to 110 μs earlier for distributed synapses than for localised synapses (Figure 11D3), a physiologically relevant time difference for an MSO neuron. This difference was more pronounced for the slow axonal velocity condition. For the fast axonal velocity condition there was a maximum peak advance of only 65 μs relative to the single input, although this might still be a functionally relevant time difference for an MSO neuron. This result suggests myelin in terminal branches might play a role in tuning peak timing in the MSO.

The larger membrane depolarisation induced by distributed inputs generated larger low threshold potassium current (I_{KLT}). As I_{KLT} is known to sharpen EPSPs in the MSO (Mathews et al., 2010), it can explain why distributed inputs can have both higher amplitudes and shorter halfwidths, as well as earlier peak timing. We repeated our simulations using a static KLT model to test whether I_{KLT} plays a role in generating the differences we observed. In this model, the gating variables of the KLT conductance are frozen at their steady state resting values, eliminating dynamic changes in KLT conductance (Mathews et al., 2010). In this version of the model, somatic EPSPs were larger for all simulated synaptic inputs, and distributed inputs again elicited larger somatic EPSPs (Figure 11E1). Contrary to the normal, dynamic KLT model, however, the EPSP halfwidths were larger for distributed synapses, as expected given the reduced amount of I_{KLT} available to sharpen the large EPSPs (Figure 11E2). Static I_{KLT} also reversed the trend in peak timing, with EPSPs from distributed synapses peaking later than EPSPs from single synapses (Figure 11E3).

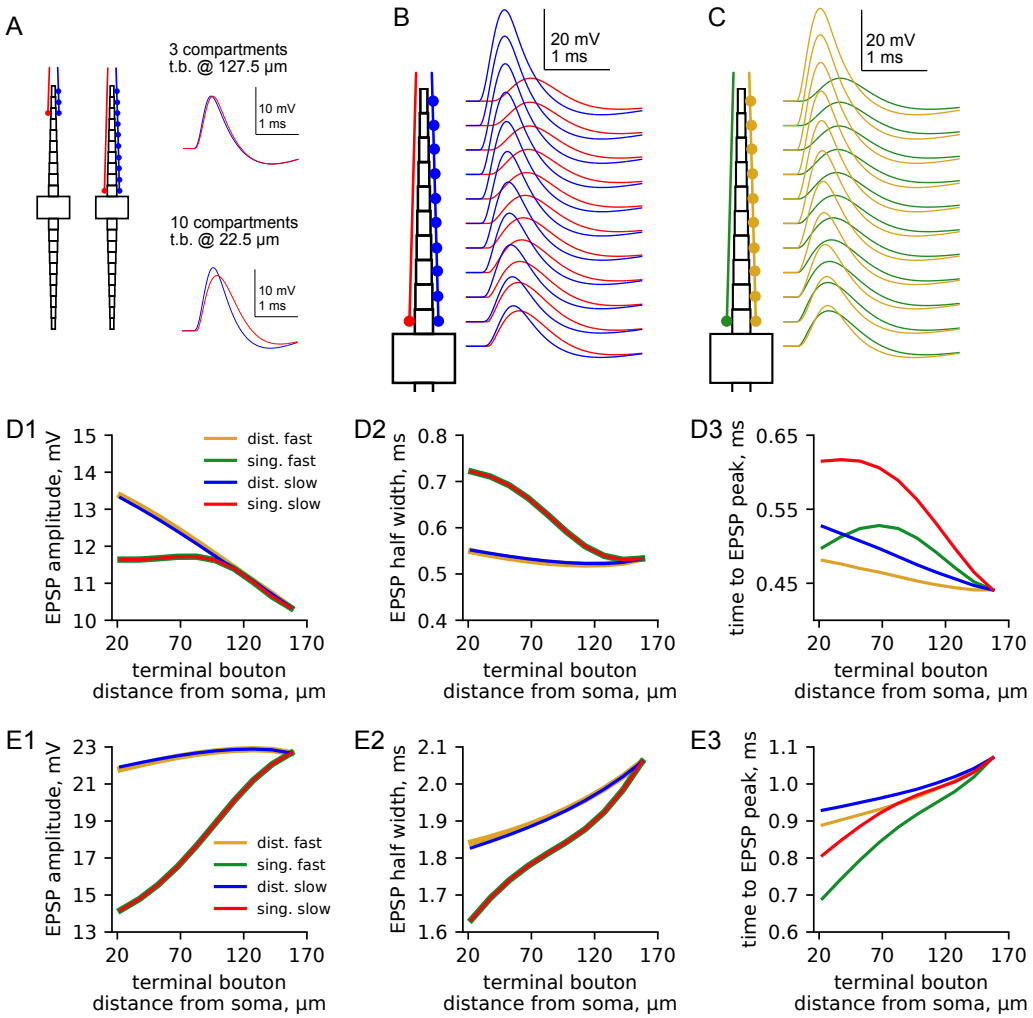

Figure 11. **A.** Two example configurations of synaptic input, shown on schematic of model geometry, with total conductance-matched single (red) and distributed (blue) synapses, and corresponding somatic membrane potential traces at right. Axonal conduction velocity = 1 m/s. t.b. = terminal bouton. **B.** Membrane potential for each compartment on the synaptically active dendrite plus soma. Traces correspond to the adjacent compartment in schematic. Axonal conduction velocity = 1 m/s. **C.** Same as B but with axonal conduction velocity = 10 m/s. **D.** Somatic EPSP properties relative to position of single or terminal synaptic bouton. **E.** Somatic EPSP properties for a version of the model with I_{KLT} frozen at resting conductance levels.

To see if the effects we observed in our simulations of single-dendrite stimulation might translate to an effect on ITD coding, we simulated the model with inputs to both dendrites. A 400 Hz train of EPSGs was simulated

(peak total conductance per dendrite = 17.5 nS) and the difference in input timing between dendrites was varied. We tested four different synaptic input configurations, each with a terminal bouton at the most proximal dendritic compartment. We compared a single site of synaptic input to distributed inputs over two, four, or six compartments (Figure 12A). The four compartment input configuration was designed to resemble our data and therefore simulated the median number of boutons, distributed over about half of the dendritic length, with a terminal bouton close to the soma. A trace of the simulated somatic membrane potential for this configuration shows both higher maximum and lower minimum values compared to the single synapse (Figure 12B). This idicates larger EPSPs recruiting more I_{KLT} in the distributed configuration. Varying the input timing between dendrites produces variations in peak somatic membrane potential similar to an ITD function recorded from MSO neurons in vivo (Figure 12C, Brand et al., 2002). The peak membrane potentials were larger for more distributed inputs but the overall range of values (maximum – minimum) was also larger, resulting in a steeper slope of the function (Figure 12D).

To determine whether the variations in binaural integration between single and distributed synaptic input might be physiologically relevant, we calculated Fisher information for the different input configurations. Assuming Poisson statistics of MSO spike counts, and given that subthreshold membrane potential corresponds well to spiking responses to ITDs (van der Heijden et al., 2013), Fisher information was calculated according to:

$$F(\Delta T) = \frac{f'(\Delta T)^2}{f(\Delta T)}$$

and normalised to the peak value for the single bouton simulation. As expected, information was maximum at the steepest part of the ΔT response function. Fisher information was greater for distributed synaptic input compared to a single localised synaptic site, and highest for the most distributed synapse we simulated (6 synaptic boutons). Distributed synapses could therefore be physiologically relevant features of the MSO circuit and contribute to ITD coding.

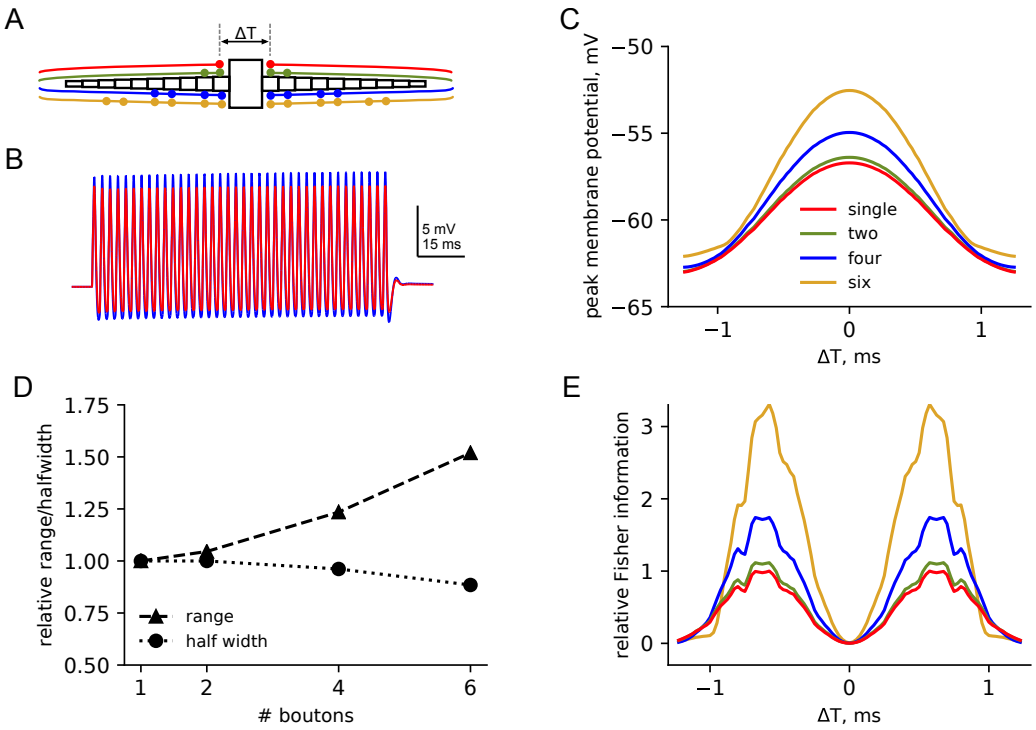

Figure 12. **A.** Different synaptic innervation patterns, with 1, 2, 4, or 6 synaptic boutons, tested with varying input timing between dendrites. **B.** Example traces of simulations with 1 (red) or 4 (blue) synapses per axon. Total synaptic conductance = 17.5 nS per dendrite, ITD = 0.4 ms. **C.** Peak somatic membrane potential generated during a 400 Hz train of EPSGs, with varying ΔT. **D.** Response function ranges and half widths relative to the values for a single bouton synapse. **E.** Fisher information across the ΔT response functions for each synaptic condition. Colours correspond to Panel C.

Discussion

We have shown that excitatory axons from the cochlear nucleus innervate MSO neurons with a variable but stereotyped pattern. Axons approach MSO neurons at relatively distal positions and run parallel to the dendrite, forming several synaptic boutons, before terminating with a bouton relatively close to the soma. They stay close to the dendrite and only occasionally form branches, which themselves run in parallel to the dendrite. Given the distribution of boutons along the dendrites, and the tendency of terminal boutons to be positioned close to the soma, it is unlikely that dendritic propagation delays have significant differential effects on excitatory inputs.

Using a computational model, we have shown that the pattern of synaptic input to the dendrites can affect the somatic voltage response. The somatic membrane response to distributed inputs was larger and briefer, and occurred earlier, when compared to the response to spatially restricted synaptic input. Distributed inputs in the model generated larger low threshold potassium currents, suggesting a mechanism by which distributed inputs could amplify incoming signals while maintaining temporal precision. A recent study provides evidence for functionally relevant high threshold potassium channels in MSO neurons (Nabel et al., 2019). As models with only low threshold potassium channels capture the essential features of MSO membrane resonses (Mathews et al., 2010; Winters et al., 2017), we decided to use a simpler model, which omitted high threshold channels. We therefore cannot rule out the possibility that an interplay between the distributions of excitatory synapses and different potassium channel subunits might contribute to voltage signalling in MSO neurons.

Simulating inputs to both dendrites and varying the time difference of inputs between dendrites showed that distributed synapses can affect the integration of dendritic signals at the soma, and therefore might play a role in ITD processing in MSO neurons. The arrangement of excitatory inputs that we observed in the gerbil might therefore be a meaningful adaptation to optimise sound localisation based on ITDs.

We provide complementary anatomical evidence that corroborates the physiological evidence from Couchman et al. (2010). They determined that excitatory (as well as inhibitory) inputs to MSO neurons are large, with activation of only two to four excitatory fibres per dendrite needed to stimulate action potential generation from rest. Given that we observe a median of four boutons per axon, and up to 30 boutons per dendrite (which is very likely an underestimate), MSO neurons most likely receive about twice this minimum amount of excitatory input per dendrite. Since inputs to the MSO also exhibit substantial short-term synaptic depression, especially at higher frequencies (Couchman et al., 2010), these additional (beyond the minimum) inputs could help maintain sufficient excitatory drive during prolonged stimuli.

Our results are also in accordance with previous anatomical studies. An electron microscopy study of the cat by Lindsey (1975) definitively showed at least one example of an axon innervating an MSO neuron with more

than one bouton (his Figure 9). Additionally, Beckius et al. (1999) provide anatomical hints of multiple synaptic boutons from a single axon innervating an MSO neuron (their Figure 7), although they did not stain MSO neurons in that study. We provide strong evidence that, in the gerbil, excitatory inputs form multiple synaptic sites along MSO dendrites.

Previous studies have shown that multiple neurotransmitter release sites can be present within a single synaptic bouton (Lindsey, 1975; Kiss and Majorossy, 1983) Excitatory axons therefore effectively form large, distributed synapses on MSO neurons. We have not shown, however, whether the various synaptic sites along a single axon have similar strengths. Nor could we show how many axons innervate a single dendrite. Further studies using electron microscopy would be essential to answer these questions.

Our results from modelling excitatory inputs to single MSO neuron dendrites suggests that myelin could affect EPSP timing. In the study by Lindsey (1975), the author observed myelin on the axon between two synaptic boutons. The axon itself ran parallel to the dendrite, like the axons observed in the present study. Several other electron microscopy studies have also shown myelinated sections of axons immediately adjacent to synaptic boutons in cat (Clark, 1969; Kiss and Majorossy, 1983). Electron micrographs of ferret MSO show many myelinated axons adjacent to MSO dendrites (Brunso-Bechtold et al., 1990). Although that study does not show that these axons are the same as those forming synaptic boutons, the lack of unmyelinated axons in their images, and the similarity in axonal arrangement to what we have observed in the present study suggest myelination might be the norm, at least in ferret.

Systematic variations in myelination might also represent a mechanism by which the ITD sensitivity of MSO neurons can be adjusted. Recent studies have shown that myelination in the auditory brainstem can be finely tuned to influence action potential timing (Ford et al., 2015; Stange-Marten et al., 2017). It is therefore possible that myelination of excitatory inputs to the MSO might also be optimised during development to subserve ITD sensitivity. Although we observed no differences between inputs to ipsilateral and contralateral dendrites, differing amounts of myelination between inputs remains a potential mechanism for controlling input timing.

The pattern of excitatory innervation that we observe is likely constrained by both functional and developmental factors. The MSO in gerbils has evolved to be sensitive to ITDs and possesses adaptations that subserve this function. Some aspects of the circuit might nevertheless be developmentally, rather than physiologically constrained. Axons growing from the cochlear nucleus towards the MSO would naturally approach the distal ends of MSO dendrites due to the relative positions of the two nuclei. Competition from contralateral axons appears to restrict innervation to the lateral dendritic field (Kitzes et al., 1995). Repetition of this study with young animals pre- and post-hearing could shed some light on developmental constraints, and whether our observed pattern of excitatory innervation might be physiologically constrained. The glycinergic inputs to MSO neurons set a strong precedent for physiologically constrained development of synaptic input patterns. The mature pattern of glycinergic inputs has been shown to have distinct functional relevance (Brand et al., 2002; Pecka et al., 2008) and its developmental is strongly modulated by the acoustic environment of the animal (Kapfer et al., 2002; Magnusson et al., 2005). An additional related factor, unexplored in this study, is the possibility of systematic variation of input patterns across the tonotopic axis of the MSO. Further histological studies will be necessary to determine if such systematic variation is present.

One argument in favour of physiological relevance of the observed input pattern is the contrast in synaptic strengths between MSO and lateral superior olive (LSO). While the MSO has strong excitatory synapses, with activation of only few needed for suprathreshold excitation (Couchman et al., 2010), the LSO has been shown to have many, weaker excitatory inputs (Gjoni et al., 2018). The MSO is believed to have evolved through duplication and subsequent alteration of the LSO circuitry (Grothe and Pecka, 2014), suggesting the pattern of large distributed synapses in the MSO is likely a specific adaptation to ITD detection.

References

Baumann VJ, Lehnert S, Leibold C, Koch U (2013) Tonotopic organization of the hyperpolarization-activated current (Ih) in the mammalian medial superior olive. *Front Neural Circuit* 7:117.

Beckius GE, Batra R, Oliver DL (1999) Axons from anteroventral cochlear nucleus that terminate in medial superior olive of cat: observations related to delay lines. *J Neurosci* 19:3146–61.

Brand A, Behrend O, Marquardt T, McAlpine D, Grothe B (2002) Precise inhibition is essential for microsecond interaural time difference coding. *Nature* 417:543–7.

Brunso-Bechtold JK, Henkel CK, Linville C (1990) Synaptic organization in the adult ferret medial superior olive. *J Comp Neurol* 294:389–398.

Clark GM (1969) The ultrastructure of nerve endings in the medial superior olive of the cat. *Brain Res* 14:293–305.

Couchman K, Grothe B, Felmy F (2010) Medial superior olivary neurons receive surprisingly few excitatory and inhibitory inputs with balanced strength and short-term dynamics. *J Neurosci* 30:17111–21.

Couchman K, Grothe B, Felmy F (2012) Functional localization of neurotransmitter receptors and synaptic inputs to mature neurons of the medial superior olive. *J Neurophysiol* 107:1186–98.

Ford MC, Alexandrova O, Cossell L, Stange-Marten A, Sinclair J, Kopp-Scheinpflug C, Pecka M, Attwell D, Grothe B (2015) Tuning of Ranvier node and internode properties in myelinated axons to adjust action potential timing. *Nat Commun* 6:8073.

Gentet LJ, Stuart GJ, Clements JD (2000) Direct measurement of specific membrane capacitance in neurons. *Biophys J* 79:314–20.

Gjoni E, Zenke F, Bouhours B, Schneggenburger R (2018) Specific synaptic input strengths determine the computational properties of excitation-inhibition integration in a sound localization circuit. *J Physiol* 596:4945–4967.

Goldberg JM, Brown PB (1969) Response of binaural neurons of dog superior olivary complex to dichotic tonal stimuli: some physiological mechanisms of sound localization. *J Neurophysiol* 32:613–636.

Grothe B, Pecka M (2014) The natural history of sound localization in mammals–a story of neuronal inhibition. *Front Neural Circuit* 8:116.

Grothe B, Pecka M, McAlpine D (2010) Mechanisms of sound localization in mammals. *Physiol Rev* 90:983–1012.

Kapfer C, Seidl AH, Schweizer H, Grothe B (2002) Experience-dependent refinement of inhibitory inputs to auditory coincidence-detector neurons. *Nat Neurosci* 5:247–53.

Kiss A, Majorossy K (1983) Neuron morphology and synaptic architecture in the medial superior olivary nucleus. *Exp Brain Res* 52:315–327.

Kitzes LM, Kageyama GH, Semple MN, Kil J (1995) Development of ectopic projections from the ventral cochlear nucleus to the superior olivary complex induced by neonatal ablation of the contralateral cochlea. *J Comp Neurol* 353:341–363.

Klumpp RG, Eady HR (1956) Some Measurements of Interaural Time Difference Thresholds. *J Acoust Soc Am* 28:859–860.

Lehnert S, Ford MC, Alexandrova O, Hellmundt F, Felmy F, Grothe B, Leibold C (2014) Action potential generation in an anatomically constrained model of medial superior olive axons. *J Neurosci* 34:5370–84.

Lindsey BG (1975) Fine structure and distribution of axon terminals from cochlear nucleus on neurons in the medial superior olivary nucleus of the cat. *J Comp Neurol* 160:81–103.

Magnusson AK, Kapfer C, Grothe B, Koch U (2005) Maturation of glycinergic inhibition in the gerbil medial superior olive after hearing onset. *J Physiol* 568:497–512.

Mathews PJ, Jercog PE, Rinzel J, Scott LL, Golding NL (2010) Control of submillisecond synaptic timing in binaural coincidence detectors by K(v)1 channels. *Nat Neurosci* 13:601–9.

Meeks JP, Mennerick S (2007) Action Potential Initiation and Propagation in CA3 Pyramidal Axons. *J Neurophysiol* 97:3460–3472.

Myoga MH, Lehnert S, Leibold C, Felmy F, Grothe B (2014) Glycinergic inhibition tunes coincidence detection in the auditory brainstem. *Nat Commun* 5:3790.

Nabel AL, Callan AR, Gleiss SA, Kladisios N, Leibold C, Felmy F (2019) Distinct Distribution Patterns of Potassium Channel Sub-Units in Somato-Dendritic Compartments of Neurons of the Medial Superior Olive. *Front Cell Neurosci* 13:38.

Pecka M, Brand A, Behrend O, Grothe B (2008) Interaural time difference processing in the mammalian medial superior olive: the role of glycinergic inhibition. *J Neurosci* 28:6914–25.

Rall W (1967) Distinguishing theoretical synaptic potentials computed for different soma-dendritic distributions of synaptic input. *Journal of neurophysiology* 30:1138–68.

Rautenberg PL, Grothe B, Felmy F (2009) Quantification of the three-dimensional morphology of coincidence detector neurons in the medial superior olive of gerbils during late postnatal development. *J Comp Neurol* 517:385–96.

Rinzel J, Rall W (1974) Transient Response in a Dendritic Neuron Model for Current Injected at One Branch. *Biophysical Journal* 14:759–790.

Seidl AH, Rubel EW (2016) Systematic and differential myelination of axon collaterals in the mammalian auditory brainstem. *Glia* 64:487–494.

Sinclair JL, Fischl MJ, Alexandrova O, Heβ M, Grothe B, Leibold C, Kopp-Scheinpflug C (2017) Sound-Evoked Activity Influences Myelination of Brainstem Axons in the Trapezoid Body. *J Neurosci* 37:8239–8255.

Smith PH, Joris PX, Yin TCT (1993) Projections of physiologically characterized spherical bushy cell axons from the cochlear nucleus of the cat: Evidence for delay lines to the medial superior olive. *J Comp Neurol* 331:245–260.

Spitzer MW, Semple MN (1995) Neurons sensitive to interaural phase disparity in gerbil superior olive: diverse monaural and temporal response properties. *J Neurophysiol* 73:1668–90.

Stange-Marten A, Nabel AL, Sinclair JL, Fischl M, Alexandrova O, Wohlfrom H, Kopp-Scheinpflug C, Pecka M, Grothe B (2017) Input timing for spatial processing is precisely tuned via constant synaptic delays and myelination patterns in the auditory brainstem. *P Natl Acad Sci USA* 114:E4851–E4858.

Stotler WA (1953) An experimental study of the cells and connections of the superior olivary complex of the cat. *J Comp Neurol* 98:401–431.

van der Heijden M, Lorteije JAM, Plauška A, Roberts MT, Golding NL, Borst JGG (2013) Directional hearing by linear summation of binaural inputs at the medial superior olive. *Neuron* 78:936–48.

Weidner C, Schmelz M, Schmidt R, Hansson B, Handwerker HO, Torebjörk HE (1999) Functional attributes discriminating mechano-insensitive and mechano-responsive C nociceptors in human skin. *J Neurosci* 19:10184–90.

Werthat F, Alexandrova O, Grothe B, Koch U (2008) Experience-dependent refinement of the inhibitory axons projecting to the medial superior olive. *Dev Neurobiol* 68:1454–62.

Winters BD, Jin SX, Ledford KR, Golding NL (2017) Amplitude Normalization of Dendritic EPSPs at the Soma of Binaural Coincidence Detector Neurons of the Medial Superior Olive. *J Neurosci* 37:3138–3149.

Yin TC, Chan JC (1990) Interaural time sensitivity in medial superior olive of cat. *J Neurophysiol* 64:465–88.

Chapter 4

Discussion

MSO neurons are exquisitely sensitive coincidence detectors, which are adapted for rapid membrane voltage signalling. Their position in the auditory brainstem circuitry affords them sensitivity to ITDs—sub-millisecond cues used for low frequency sound localisation. Specific adaptations include a set of voltage-gated ion channels which provide the fast membrane time constants necessary for precise coincidence detection. In Chapter 2, we have shown that the MSO's complement of ion channels is richer than previously thought, with implications for membrane voltage signalling. Computational modelling indicated that adding KHT to a KLT-only MSO model affects membrane signalling in a functionally relevant way. In Chapter 3, we have elucidated the pattern of excitatory synaptic inputs to MSO neuron dendrites. Afferent axons form distributed, multi-site synapses, which, according to our model, produce different membrane responses when compared to large, localised synapses, and which are also likely to influence ITD tuning in MSO neurons.

4.1 Potassium channels in the MSO

Studies of membrane voltage signalling in the MSO have focussed heavily on dendrotoxin sensitive KLT channels (Scott et al., 2005; Mathews et al., 2010; Franken et al., 2015). These channels belong to the Kv1 subfamily of potassium channels. In Chapter 2, we have provided histological and physiological evidence for Kv2 and Kv3 channels in MSO neurons. These are high-threshold channels and it is surprising to find them in cells whose membrane potential is believed to not deviate greatly from resting potential, and which show little action potential back propagation (Scott et al., 2007). Although somatic and proximal dendritic membrane potentials rarely deviate more than 20 mV from rest (Scott et al., 2005; Franken et al., 2015), EPSPs may reach relatively high amplitudes in the distal dendrites. Experiments have shown strong attenuation of forward propagating EPSPs (Mathews et al., 2010), necessitating relatively large dendritic EPSPs, which have been observed (Winters et al., 2017). The mechanism is most likely the geometry of the dendrites (Winters et al., 2017), which taper towards the distal end (Rautenberg et al., 2009). This leads to an increase in input resistance with increasing dendritic distance from the soma, as we observed experimentally and in a computational model (Chapter 2, Figure 7C). With sufficient synaptic input, MSO neuron dendrites are likely to reach membrane potentials sufficient to activate higher threshold potassium channels.

Regardless of the membrane potentials reached by MSO neurons, our recordings show that the combined dendrotoxin-insensitive potassium current (KHT) is active even around the resting potential, and thereby contributes to passive membrane properties. In our model, KHT made a substantial contribution to the resting membrane potential (Chapter 2). It was possible to construct a KHT-only model with identical membrane potential and input resistance to KLT-containing models although, as expected, this model did not recapitulate the behaviour of MSO neurons. The shallower activation curve of KHT compared to KLT resulted in qualitatively different membrane behaviour. In recordings conducted with DTX in the recording solution, washing in additional potassium channel blockers caused a further increase of the input resistance (Chapter 2, Figure 6F and G). Although KHT contributes to the resting potential of the cell, based on our modelling it does not play a role in maintaining isopotentiality throughout the cell. The KHT-only model was, in fact, the least isopotential, although the largest difference in resting potential between compartments of the model was less than the difference observed in dual recordings, which showed no distinct trend. Although we observed no statisitically significant variation in membrane potential throughout the cell, given the limited number of our paired recordings experiments, this possibility should not be ruled out entirely.

We observed a clear effect on EPSP timing and amplitude of adding KHT to our model MSO neuron. Adding KHT, and thereby reducing the total KLT conductance,

appears to increase the response amplitude at the expense of timing. EPSPs were larger but were delayed and had wider half widths (half width data not shown), which was reflected in the shallow response curve to temporally offset, bilateral synaptic inputs (Chapter 2, Figure 9D). KLT clearly dominated the dynamics of membrane signalling in the model, as shown by the greater qualitative similarity between KLT-only and mixed models. The KHT-only model exhibited a distinctly different trend in its responses to variations in input strength and timing. This result is expected given the steep activation curve of KLT, whose conductance rapidly increases just above resting potential (Mathews et al., 2010). KHT nevertheless has a quantitative effect on membrane signalling. Although the MSO is believed to be adapted for maximum precision (Golding and Oertel, 2012), it is not clear if the fastest possible EPSPs and shortest possible integration time window are, in fact, optimal for ITD detection by MSO neurons. Indeed, there are neurons in the auditory brainstem with even more extreme membrane properties than MSO cells, namely the octopus cells of the cochlear nucleus (discussed further below). Additionally, Myoga et al. (2014) showed that when EPSPs were slower (i.e. had longer half widths), inhibitory synaptic inputs were more effective in shifting peak time. Slowing down of membrane signalling with KHT might therefore represent a developmental mechanism to allow optimal modulation of internal delays in MSO neurons. This idea naturally leads to the possibility that KHT could be differentially modulated between neurons, and perhaps across the tonotopic axis of the MSO.

In our computational model we restricted our simulations to only one combination of peak KLT and KHT conductances, however a large range of combinations is likely compatible with MSO function. More extensive computational modelling might be able to distinguish the limit of this range—the maximum ratio of KHT to KLT at which MSO neurons remain effective as ITD detectors. Experiments with conductance clamp could be conducted to evaluate the effect on MSO neurons in vitro. Intrinsic potassium currents can be blocked pharmacologically, and voltage-gated potassium currents can be applied via conductance clamp (Mendonça et al., 2018) to determine how different amounts of KLT and KHT affect voltage signalling in vitro. Combined with bilateral synaptic stimulation, the effect of potassium currents on synaptic integration can be investigated and compared to our model results (Chapter 2, Figure 9).

Based on our histological data, different potassium channel subunits are differentially distributed throughout MSO neurons. Neither our modelling nor our electrophysiological recordings provide an explanation for the distribution patterns we observed. In general, we observed a tendency for high threshold channel subunits (Kv2.1, 2.2, and 3.1b) to be expressed even in the distal dendrites, while low threshold subunits (Kv1.1 and Kv1.6) were biased towards the soma. Although some sub-units showed the opposite trend (Kv3.2 and Kv1.2), the presence of higher threshold channels at the distal dendrites makes intuitive sense given the

presumed higher EPSP amplitudes in this part of the neuron. Further voltage clamp experiments could more specifically quantify the properties of potassium channels in the MSO neuron, while experiments using, for example, conductance clamp, could elucidate their function. Further computational modelling of different distributions of channels, including more realistic neuronal morphology, could help inform the design of experiments and suggest explanations for their results. Specifically, modelling different amounts (i.e. current densities) of different channels, could suggest the candidates for pharmacological or conductance clamp experimental interventions that are most likely to reveal meaningful and functional properties of the MSO cell membrane.

4.2 Excitatory synaptic inputs to the MSO

Previous physiological evidence has shown that MSO neurons receive large excitatory synaptic inputs, of which only one to two per side are required to evoke action potentials from the resting membrane potential (Couchman et al., 2010). Additionally, functional AMPA receptors have been identified along the full extent of MSO dendrites (Couchman et al., 2012). In Chapter 3, we corroborated these results with anatomical evidence showing large, distributed, glutamatergic synapses, each of which covers a large extent of the dendrite. We have also shown that there is a clear excess of excitatory input beyond what is required for action potential initiation. Given the short term synaptic depression observed by Couchman et al. (2010) and the presence of inhibition accompanying excitation (Grothe and Sanes, 1993; Brand et al., 2002; Roberts et al., 2013; Franken et al., 2015), the amount of excitatory input we observed is likely necessary for reliable responses in vivo, especially during ongoing stimulation.

From our measurements, we could not determine any significant difference between ipsilateral and contralateral inputs. It is important to note, however, that the biocytin filling procedure was less succesfull in filling contralateral axons, and they therefore only constituted 20% of our measurements (11 out of 55 axons). Given the large variation we saw, even when considering just the ipsilateral inputs, it is possible there are subtle differences between sides that we could not detect with our limited sample. Such differences, even if subtle, could be meaningful if a population response is important for ITD coding and sound localisation (McAlpine et al., 2001; Lesica et al., 2010).

From our anatomical data, we cannot identify the role of distributed excitatory synapses, although our data and model do suggest some potential advantages for such an arrangement. First, they likely solve the problem of propagation delay, which is theoretically large enough to affect ITD coding in MSO neurons (Winters et al., 2017; Chapter 3, Figure 2). Our measurements show that individual inputs to MSO neurons

are likely to cover a similar dendritic extent to inputs on the opposite dendrite. Additionally, the terminal boutons tend to cluster close to the soma. Second, they appear to increase the EPSP amplitude, while maintaining a brief EPSP half width. Our modelling suggests that distributed inputs can increase the dynamic range of the membrane response to temporally offset bilateral excitation. Given that action potential output appears to follow the same pattern as sub-threshold membrane response to ITDs in vivo (van der Heijden et al., 2013), we calculated an increase in Fisher information for distributed synapses. Such an arrangement of excitatory synapses may therefore be computationally advantageous for sound localisation.

A potentially important feature of the distributed excitatory inputs that we have observed is the strength of individual synaptic sites. Our approach did not allow us to accurately measure the size of synaptic boutons, nor could we observe the number of synaptic release sites per bouton. Previous studies indicate that multiple release sites can be present on single boutons (Lindsey, 1975; Kiss and Majorossy, 1983). Although we did not measure bouton dimensions, boutons clearly varied in size (see, for example, the axon depicted in Figures 7 and 8 of Chapter 3), which could relate to the number of release sites.

MSO neurons exhibit synaptic amplitude normalisation, which results in a minimal effect of synaptic position on the somatic EPSP amplitude (Winters et al., 2017), in spite of strong attenuation by low-threshold potassium channels (Mathews et al., 2010). The EPSPs elicited at the individual boutons should therefore reflect their impact on somatic EPSP amplitude. If bouton strengths were systematically weighted towards proximal or distal boutons, a distributed synapse would effectively behave like a more localised synapse. Our modelling suggests that distribution of synaptic conductance is computationally advantageous for ITD detection, so equal weighting of synaptic strength within a distributed synapse is more likely. This prediction requires testing with additional experiments (see methodological considerations, below).

4.3 Methodological considerations

4.3.1 Biases in neuronal morphometry

Although every effort was made to systematically scan each stack of images for measureable axons, there could still be some bias in the axons that were identified. As described in Chapter 3, axons were not measured if their associated dendrites were cut off at the limit of the image stack (which includes dendrites severed at the surface of the tissue section). Additionally, incomplete antibody penetration means that the full extent of dendrites that extend into the centre of the section might not be visible. If dendrites tend to follow paths that deviate significantly from the plane of the slice, there could be a bias to select neurons with shorter dendrites. Indeed, the estimated dendritic length for measured neurons in Chapter 3 was shorter than that

reported for neurons filled with biocytin (data not shown; Rautenberg et al., 2009). Nevertheless, even if there is a selection bias for more spatially compact neurons, the conclusions in Chapter 3 should still be valid, at least for MSO neurons of this type. It remains a possibility that neurons with more extensive dendritic trees exhibit different innervation patterns, although no systematic morphological variations have been observed in the gerbil MSO previously.

An alternative and likely explanation for the apparently shorter dendrites is failure of the MAP2 antibody to stain the full extent of the dendrites. This represents a more significant problem, as it can mean that axons that terminated near the distal ends of dendrites could be excluded from the measurements, even when other axons terminating more proximal to the soma are included in the data set. This could therefore introduce a bias into the measurements for axons terminating at more proximal dendritic positions. Although this does not explain the reduced incidence of terminal boutons at intermediate distances from the soma (see Chapter 3, figure 6), it nevertheless remains a significant concern. This concern would be most effectively addressed by use of an alternative method, such as electron microscopy, which is discussed below.

Biocytin only fills a subset of the spherical bushy cells in the cochlear nucleus, and we could therefore visualise only a subset of the excitatory inputs to each MSO neuron. We observed a range of values for all of the parameters we measured, but it is not clear how these parameters vary in or between neurons, as we could rarely measure multiple axons innervating a single dendrite. If many filled axons innervated a single dendrite, it was difficult to isolate individual axons, so typically no measurements were made in these cases. The selection of axons to measure was therefore biased to dendrites with fewer filled axons, although it is unclear if this would affect the validity of the measurements. Assuming the filling of spherical bushy cells was random, a systematic error on this basis is unlikely.

Full reconstruction of all the inputs to a dendrite using electron mircoscopy, although considerably more time-consuming, would complement some weaknesses of the biocytin method we used. Although paired recordings have been used in other parts of the brain to study the structure of synaptic connectivity (e.g. Buhl et al., 1997), the limited number of inputs from the cochlear nucleus to MSO neurons, as well as the relative positions of these nuclei, would limit the utility of this method. Electron microscopy would likely be a more reliable approach, and would also afford the ability to estimate the strength of individual synaptic terminals, as the size of each could be accurately measured. Finally, the total number of synaptic sites per dendrite could also be definitively determined, as even our largest measurements from single dendrites is certainly a significant underestimate.

An important, unresolved question in regards to the excitatory inputs is that of the role of myelin, as discussed in Chapter 3. Our modelling results show that myelin could influence the time to peak of EPSPs at the soma. The difference

between our slow and fast model variants was, however, least for the distributed inputs. Our data show that inputs to the MSO are typically distributed along the dendrite. Further anatomical studies are required to determine the pattern of myelination of these terminal axonal branches. There is some evidence for myelination of terminal branches, though none of it is definitive or comprehensive (gerbil, Kapfer et al., 2002; cat, Clark, 1969; Lindsey, 1975; Kiss and Majorossy, 1983; ferret, Brunso-Bechtold et al., 1990). Three dimensional reconstruction based on electron microscopy would answer the question of myelin in addition to clarifying the pattern and number of excitatory inputs. Ipsilateral and contralateral inputs should, of course, be compared, as myelin remains a potential means by which excitatory input timing is modulated in the MSO (Ford et al., 2015; Seidl and Rubel, 2016; Stange-Marten et al., 2017).

4.3.2 Conductance-based models of MSO neurons

The MSO neuron models used for simulations in this thesis are conductance-based models, in which the neuron is modelled as an electrical circuit consisting of a capacitance (representing the lipid bilayer) and a series of ionic conductances. Such models originate with the work of Hodgkin and Huxley (Hodgkin and Huxley, 1952) and many recent MSO neuron models consist of essentially the same mathematical represenation (Zhou et al., 2005; Mathews et al., 2010; Lehnert et al., 2014; Winters et al., 2017), or a simplification thereof (Agmon-Snir et al., 1998; note that a different model type, an integrate-and-fire model, was also used in this study).

The models in this thesis were based most directly on that of Lehnert et al. (2014), but with relevant changes to certain parameters. The most important of these relate to the geometry of the model cell and the inclusion of a high voltage-activated potassium conductance in the dendrites. The focus here was on dendritic integration of MSO inputs, whereas for Lehnert it was on action potential initiation. Therefore the models in this thesis consist of only a soma and dendrites. The lack of axon means the models in this thesis lack sodium channels, which were also excluded from the soma so that action potentials could not be generated. The somato-dendritic geometry of these models resembles those of Mathews et al. (2010) and Winters et al. (2017). In chapter 2, the dendritic geometry was constrained based on dual patch clamp recordings from MSO neurons. As a result, a taper was introduced to the dendrites, such that they were thinner more distally from the soma, as has been observed in real MSO neurons (Rautenberg et al., 2009). A tapered dendrite was also used as one model variant by Winters et al. (2017), where it was found to be the most effective of the parameters tested in reproducing amplitude normalisation of synaptic inputs in MSO cells. Given the success of tapered dendritic geometry in reproducing the behaviour of the MSO neuronal membrane, it was retained for the study in Chapter 3.

The inclusion of a high-threshold potassium conductance is the other major difference of the model in Chapter 2 from that of Lehnert et al. (2014) and other biophysical MSO models. Investigating the role of such a conductance was the specific goal of this model. The dynamics of the dendrotoxin insensitive potassium current was measured in vitro for the purpose of generating meaningful parameters for the model. In Chapter 3 this conductance was excluded for simplicity, as it was not the focus of the study, and the qualitative behaviour of MSO neurons can be reproduced without it.

4.4 Implications for ITD tuning

In Chapters 2 and 3, we have explored two additional means by which input timing and amplitude could be modulated in MSO neurons. We have shown that adding KHT to a computational model of an MSO neuron can cause a delay of EPSP peaks at the soma. When comparing large, localised synapses to distributed synapses, we found that distributed synapses resulted in earlier EPSP peaks. Although opposite effects, these are not obviously contradictory results. For both addition of KHT and distribution of synapses, we found an increase in somatic EPSP amplitude. Maintaining strong responses to synaptic inputs may be more important for the neuron, and the modest changes to EPSP peak timing might be relatively minor epiphenomena. Modulation of the shape of the ITD function could be more effectively achieved through factors such as inhibition (Pecka et al., 2008), cochlear delays (Benichoux et al., 2015), or differential axonal propagation times (Seidl and Rubel, 2016). Further investigation is clearly needed to clarify how these effects influence the function of MSO neurons.

We used computational models to explore the functional implications of both KHT currents and distributed synaptic inputs. It should be noted, however, that we performed a limited set of simulations and focussed on unitary EPSPs, or trains of EPSPs of fixed magnitude and frequency. MSO neurons respond differently to the onset and ongoing components of sound stimuli (Pecka et al., 2008; Franken et al., 2015). In previous modelling of action potential generation, more complex stimuli revealed different modes of action potential generation depending on stimulus parameters (Lehnert et al., 2014). Additionally, our simplified model did not include known physiological phenomena such as short term synaptic depression (Couchman et al., 2010), and modulation of presynaptic terminals by GABA (Stange et al., 2013). We can therefore not rule out additional effects of potassium channels or input patterns on MSO neuron responses to more complex stimuli. Many physiological processes interact to produce the behaviour of MSO neurons, and we have only made first steps in exploring how these particular factors contribute to the function of the system.

Previous modelling studies have explored how dendrites contribute to ITD sensitivity in the MSO and in the avian nucleus laminaris. Agmon-Snir et al. (1998) showed that models of single neurons were more sensitive to bilateral timing differences when dendrites were included in the morphology, compared to single compartment, spherical neuron models. One mechanism to explain this benefit is that segregation of inputs to different dendrites prevents the two sets of inputs from interfering with one another. A second synaptic event on the same dendrite produces a smaller EPSP than the first because the membrane moves closer to the reversal potential for postsynaptic glutamate receptors, resulting in reduced sensitivity to coincident inputs. Inputs on opposite dendrites only integrate at the soma, close to the action potential initiation site. Distribution of synapses on a single dendrite may represent an extension of this principle. Each synaptic bouton on an axon is activated sequentially as the action potential propagates, which may allow for maximum possible amplitude response for a given total synaptic strength.

The best relative conduction velocity between the axon and the dendrite to minimise interference is not clear, as newly initiated EPSPs could coincide with either forward- or back-propgating EPSPs. For the simulations in Chapter 3, the "slow" axonal conduction was nevertheless faster than the dendritic conduction velocity. Therefore, for both our fast and slow axonal conduction velocities, EPSPs initiated at each subsequent bouton would be "ahead" (i.e. more proximal to the soma) of the propagating EPSP initiated at the previous bouton. The practically identical EPSP amplitudes and half widths may be a consequence of this, and further simulations using a slower axonal conduction velocity may reveal some difference. Sufficiently slow axonal conduction velocities have been observed previously, for example by Meeks and Mennerick (2007) in the hippocampus.

Further simulations of different bouton arrangements could help identify the relevance of the arrangement we observed. A model with boutons arranged in the opposite direction, with the first bouton making contact close to the soma and the terminal bouton located distally, would effectively introduce a "negative" axonal conduction velocity. Intuitively, this would further eliminate the possibility for summation with forward propagting action potentials. On the other hand, the integration time window for inputs from a single axon would be increased, as action potentials in the axon must propagate distally before intitiating EPSPs that must then propagate towards the soma. This would effectively increase propagation delay. The observed arrangement of synaptic boutons might therefore be optimal for minimising the effect of propagation delay, with further fine tuning of synaptic integration achieved by modulation of axonal conduction velocity (with myelin, for example).

Modelling by Dasika et al. (2007) using single- and multi-compartmental models for dendrites suggests that the distribution of inputs along the dendrites is not essential for the cell to benefit from bilateral segregation of inputs. Our results

suggest that input distribution along a multi-compartmental dendrite might confer greater advantage than single, localised inputs. This apparent conflict may simply be a matter of magnitude of effect. Although Dasika et al. (2007) report that the qualitative effect is identical between models with different numbers of compartments per dendrite, they do not report whether there was a quantitative change in the results. Maximum benefit of dendrites to MSO cells might only be achieved with distributed inputs, even though just the presence of dendrites is sufficient to confer a computational advantage in coincidence detection.

4.5 Development of the MSO circuit

MSO neurons show strong developmental regulation around the age of hearing onset, which results in their final, mature morphology and phsyiology (Scott et al., 2005; Rautenberg et al., 2009). Given the profile of morphological development, whereby dendritic branching is drastically reduced, and membrane surface area decreases (Rautenberg et al., 2009), there is likely a concomitant development of afferent excitatory inputs. Experience dependent development of synaptic input in the MSO has already been shown for glycinergic inhibition (Kapfer et al., 2002). Additionally, the DTX-sensitive KLT current has been shown to increase significantly during development (Scott et al., 2005). It is possible that the KHT currents undergo a similar age- or experience-dependent development.

Excitatory inputs show a stereotypical pattern of innervation of MSO dendrites. Additionally, the path taken by the terminal axonal branches in close proximity to MSO dendrites, even in the absence of synaptic boutons, was consistent between examples. Axons always approached MSO neurons from a more distal position than the terminal bouton, which was always more proximal to the soma than the first point of contact between the two cells. This particular pattern of contact between the spherical bushy cell axons and MSO neurons could be functionally important, developmentally constrained, or a mix, as discussed in Chapter 3.

Large, distributed synapses might be a beneficial functional adaptation in the mammalian ITD detection circuit, as I have suggested above. Studies of cortical pyramidal neurons have shown that the direction in which synapses are activated along a dendrite affects the amplitude and timing of summated somatic EPSPs (Branco et al., 2010). Alternatively, the particular pattern we have observed could be the simple result of axons growing towards their targets from a particular relative location, and competition between axons from each side (Kitzes et al., 1995). This simple explanation does not match, however, with the circuitous route taken by many spherical bushy cell axons as they approach the MSO (cat, Smith et al., 1993; Beckius et al., 1999). Additionally, we observed that at least some axons run perpendicular to the dendrite, then bend at the point of contact to run along the

dendrite. Since we observed no cases where the axon then ran along the dendrite towards the distal end, there is likely some constraint on the interaction between the neurons. This could be a strong chemical cue for axons to grow towards the soma (or towards the contralateral brainstem hemisphere), or it could be that those axons running in the proximal to distal direction are pruned during development. Studies of the developing system are necessary to answer this question. Organotypic slice culture could be a technically challenging, though potentially profitable approach, as it allows for controlled intervention in the system (Lohmann et al., 1998; Kronander et al., 2017).

Given that MSO neurons drastically change their membrane properties during development, with major reductions in their input resistance and time constant, the roles of different potassium channels must necessarily change as well. Overshooting action potentials can be recorded in the soma of immature MSO neurons (Scott et al., 2005). Such large changes in membrane potential would be expected to activate a large fraction of the high threshold potassium current we recorded. KHT might therefore have a larger, or at least different, role in the immature system. Further electrophysiological studies of KHT in the developing MSO, before and after hearing onset, should help clarify the role of these ionic currents in both the immature and mature systems.

4.6 Comparison to other auditory nuclei

The MSO is believed to have evolved from the LSO through the processes of duplication and divergence (Grothe and Pecka, 2014; Nothwang, 2016). If MSO neurons subsequently adapted to ITD detection, we should expect to find some specific adaptations in voltage signalling to this computation. The clearest example is the duplication of the input pathways. While inputs to the LSO consist essentially of ipsilateral excitation and contralateral inhibition, the MSO receives bilateral excitation and inhibition. While the input pattern to LSO neurons allows the comparison of sound level (intensity) between ears (ILD), bilateral excitatory inputs are required for comparison of sound stimulus timing.

The pattern of synaptic inputs could be a specific adaptation to the demands of ITD detection. In contrast to the few large inputs to the MSO, excitatory synapses on LSO neurons are small and many (Gjoni et al., 2018). Graded responses to varying sound intensities could be afforded by many small inputs, which would allow effective comparison of stimulus intensity over a minimal time period. For ITD detection, MSO neurons might benefit from being relatively insensitive to stimulus intensity, as stimulus timing is the important factor. The large, distributed inputs described in Chapter 3, likely in excess of what is necessary to evoke an action potential (Couchman et al., 2010), might therefore be ideally suited to ITD detection.

Within the brainstem, octopus cells of the posteroventral cochlear nucleus exhibit similar adaptations to MSO neurons, and therefore also exhibit rapid membrane voltage signalling (Golding and Oertel, 2012). Octopus cells have been shown to have even lower input resistance (less than 3 MΩ) and time constants (approximately 200 μs) than MSO cells (Golding et al., 1999; Golding and Oertel, 2012). They also possess large KLT and Ih currents and show the same lack of back propagating action potentials, indicated by small spike amplitudes measured at the soma. Octopus cells also act as coincidence detectors, as they fire action potentials when stimulated by many auditory nerve fibres within a brief time interval, and thereby respond best to broadband sound stimuli (McGinley et al., 2012). With regard to excitatory synaptic inputs, octopus cells appear to differ from MSO cells in the size of synaptic inputs. Intracellular recordings in slices suggest octopus cells receive many small synaptic inputs, as indicated by a graded response to increasing electrical stimulation of the auditory nerve (Golding et al., 1995), as opposed to the larger inputs to MSO neurons (Couchman et al., 2010).

The speed of membrane signalling in Octopus cells appears even more extreme than in MSO cells. If octopus cells lack high threshold potassium channels, this would be an argument for a modulatory effect of KHT in the MSO. The function of MSO neurons might be better served by a mix of KLT and KHT that affords a somewhat reduced rate of membrane signalling than in octopus cells. Unfortunately, an explicit study of KHT in octopus cells is lacking, so this hypothesis, that octopus cells express less or no KHT to maximise the speed of membrane signalling, remains to be tested.

4.7 Conclusion

Both chapters in this thesis represent steps towards a more complete understanding of the MSO and sound localisation in mammals. In Chapter 2, we provided evidence for high threshold potassium channels in MSO neurons, and suggest how they can contribute to voltage signalling within these neurons. In Chapter 3, we described the pattern of excitatory synaptic innervation of MSO neurons, the anatomical basis for voltage signalling in response to chemical signals from other neurons. We have shown that the pattern of innervation can affect the membrane voltage response to inputs of the same magnitude. By focussing on a system of known function—sound localisation using ITDs—these studies provide further clues to how membrane voltage signalling underlies complex neuronal computations. They provide further steps into the ongoing study of the biophysical basis of the computations performed by single neurons and the networks they form.

Bibliography

Agmon-Snir H, Carr CE, Rinzel J (1998) The role of dendrites in auditory coincidence detection. *Nature* 393:268–72.

Baumann VJ, Lehnert S, Leibold C, Koch U (2013) Tonotopic organization of the hyperpolarization-activated current (Ih) in the mammalian medial superior olive. *Front Neural Circuit* 7:117.

Beckius GE, Batra R, Oliver DL (1999) Axons from anteroventral cochlear nucleus that terminate in medial superior olive of cat: observations related to delay lines. *J Neurosci* 19:3146–61.

Benichoux V, Fontaine B, Franken TP, Karino S, Joris PX, Brette R (2015) Neural tuning matches frequency-dependent time differences between the ears. *eLife* 4:e06072.

Benichoux V, Rébillat M, Brette R (2016) On the variation of interaural time differences with frequency. *J Acoust Soc Am* 139:1810–1821.

Branco T, Clark BA, Häusser M (2010) Dendritic discrimination of temporal input sequences in cortical neurons. *Science (New York, N.Y.)* 329:1671–5.

Brand A, Behrend O, Marquardt T, McAlpine D, Grothe B (2002) Precise inhibition is essential for microsecond interaural time difference coding. *Nature* 417:543–7.

Brunso-Bechtold JK, Henkel CK, Linville C (1990) Synaptic organization in the adult ferret medial superior olive. *J Comp Neurol* 294:389–398.

Buhl EH, Tamás G, Szilágyi T, Stricker C, Paulsen O, Somogyi P (1997) Effect, number and location of synapses made by single pyramidal cells onto aspiny interneurones of cat visual cortex. *The Journal of Physiology* 500:689–713.

Cant NB (2013) Patterns of convergence in the central nucleus of the inferior colliculus of the Mongolian gerbil: organization of inputs from the superior olivary complex in the low frequency representation. *Front Neural Circuit* 7:29.

Cant NB, Benson CG (2003) Parallel auditory pathways: projection patterns of the different neuronal populations in the dorsal and ventral cochlear nuclei. *Brain Res Bull* 60:457–474.

Cant NB, Hyson RL (1992) Projections from the lateral nucleus of the trapezoid body to the medial superior olivary nucleus in the gerbil. *Hearing Res* 58:26–34.

Carr CE, Konishi M (1988) Axonal delay lines for time measurement in the owl's brainstem. *P Natl Acad Sci USA* 85:8311–5.

Carr CE, Konishi M (1990) A circuit for detection of interaural time differences in the brain stem of the barn owl. *J Neurosci* 10:3227–46.

Carr CE, Soares D, Smolders J, Simon JZ (2009) Detection of interaural time differences in the alligator. *J Neurosci* 29:7978–90.

Clark GM (1969) The ultrastructure of nerve endings in the medial superior olive of the cat. *Brain Res* 14:293–305.

Couchman K, Grothe B, Felmy F (2010) Medial superior olivary neurons receive surprisingly few excitatory and inhibitory inputs with balanced strength and short-term dynamics. *J Neurosci* 30:17111–21.

Couchman K, Grothe B, Felmy F (2012) Functional localization of neurotransmitter receptors and synaptic inputs to mature neurons of the medial superior olive. *J Neurophysiol* 107:1186–98.

Dasika VK, White JA, Colburn HS (2007) Simple Models Show the General Advantages of Dendrites in Coincidence Detection. *J Neurophysiol* 97:3449–3459.

Fischl MJ, Burger RM, Schmidt-Pauly M, Alexandrova O, Sinclair JL, Grothe B, Forsythe ID, Kopp-Scheinpflug C (2016) Physiology and anatomy of neurons in the medial superior olive of the mouse. *J Neurophysiol* 116:2676–2688.

Fischl MJ, Combs TD, Klug A, Grothe B, Burger RM (2012) Modulation of synaptic input by GABA B receptors improves coincidence detection for computation of sound location. *J Physiol* 590:3047–3066.

Ford MC, Alexandrova O, Cossell L, Stange-Marten A, Sinclair J, Kopp-Scheinpflug C, Pecka M, Attwell D, Grothe B (2015) Tuning of Ranvier node and internode properties in myelinated axons to adjust action potential timing. *Nat Commun* 6:8073.

Franken TP, Roberts MT, Wei L, Golding NL, Joris PX (2015) In vivo coincidence detection in mammalian sound localization generates phase delays. *Nat Neurosci* 18:444–452.

Gjoni E, Zenke F, Bouhours B, Schneggenburger R (2018) Specific synaptic input strengths determine the computational properties of excitation-inhibition integration in a sound localization circuit. *J Physiol* 596:4945–4967.

Glendenning KK, Brusno-Bechtold JK, Thompson GC, Masterton RB (1981) Ascending auditory afferents to the nuclei of the lateral leminscus. *J Comp Neurol* 197:673–703.

Goldberg JM, Brown PB (1969) Response of binaural neurons of dog superior olivary complex to dichotic tonal stimuli: some physiological mechanisms of sound localization. *J Neurophysiol* 32:613–636.

Golding NL, Ferragamo MJ, Oertel D (1999) Role of intrinsic conductances underlying responses to transients in octopus cells of the cochlear nucleus. *J Neurosci* 19:2897–905.

Golding NL, Robertson D, Oertel D (1995) Recordings from slices indicate that octopus cells of the cochlear nucleus detect coincident firing of auditory nerve fibers with temporal precision. *J Neurosci* 15:3138–53.

Golding NL, Oertel D (2012) Synaptic integration in dendrites: exceptional need for speed. *J Physiol* 590:5563–9.

Grigg JJ, Brew HM, Tempel BL (2000) Differential expression of voltage-gated potassium channel genes in auditory nuclei of the mouse brainstem. *Hearing Res* 140:77–90.

Grothe B, Sanes DH (1993) Bilateral inhibition by glycinergic afferents in the medial superior olive. *J Neurophysiol* 69:1192–6.

Grothe B, Sanes DH (1994) Synaptic inhibition influences the temporal coding properties of medial superior olivary neurons: an in vitro study. *J Neurosci* 14:1701–9.

Grothe B (2000) The evolution of temporal processing in the medial superior olive, an auditory brainstem structure. *Prog Neurobiol* 61:581–610.

Grothe B, Leibold C, Pecka M (2018) The Medial Superior Olivary Nucleus In Kandler K, editor, *The Oxford Handbook of the Auditory Brainstem*. Oxford University Press.

Grothe B, Pecka M (2014) The natural history of sound localization in mammals–a story of neuronal inhibition. *Front Neural Circuit* 8:116.

Grothe B, Pecka M, McAlpine D (2010) Mechanisms of sound localization in mammals. *Physiol Rev* 90:983–1012.

Hassfurth B, Grothe B, Koch U (2010) The mammalian interaural time difference detection circuit is differentially controlled by GABAB receptors during development. *J Neurosci* 30:9715–27.

Hodgkin AL, Huxley AF (1952) A quantitative description of membrane current and its application to conduction and excitation in nerve. *The Journal of Physiology* 117:500–544.

Jeffress LA (1948) A place theory of sound localization. *J Comp Physiol Psych* 41:35–39.

Kapfer C, Seidl AH, Schweizer H, Grothe B (2002) Experience-dependent refinement of inhibitory inputs to auditory coincidence-detector neurons. *Nat Neurosci* 5:247–53.

Karino S, Smith PH, Yin TCT, Joris PX (2011) Axonal branching patterns as sources of delay in the mammalian auditory brainstem: a re-examination. *J Neurosci* 31:3016–31.

Khurana S, Liu Z, Lewis AS, Rosa K, Chetkovich D, Golding NL (2012) An essential role for modulation of hyperpolarization-activated current in the development of binaural temporal precision. *J Neurosci* 32:2814–23.

Kiss A, Majorossy K (1983) Neuron morphology and synaptic architecture in the medial superior olivary nucleus. *Exp Brain Res* 52:315–327.

Kitzes LM, Kageyama GH, Semple MN, Kil J (1995) Development of ectopic projections from the ventral cochlear nucleus to the superior olivary complex induced by neonatal ablation of the contralateral cochlea. *J Comp Neurol* 353:341–363.

Ko KW, Rasband MN, Meseguer V, Kramer RH, Golding NL (2016) Serotonin modulates spike probability in the axon initial segment through HCN channels. *Nat Neurosci* 19:826–834.

Köppl C, Carr CE (2008) Maps of interaural time difference in the chicken's brainstem nucleus laminaris. *Biol Cybern* 98:541–559.

Kronander E, Michalski N, Lebrand C, Hornung JP, Schneggenburger R (2017) An organotypic slice culture to study the formation of calyx of Held synapses in-vitro. *PLOS ONE* 12:e0175964.

Kuwabara N, Zook JM (1992) Projections to the medial superior olive from the medial and lateral nuclei of the trapezoid body in rodents and bats. *J Comp Neurol* 324:522–538.

Kuwabara N, Zook J (1999) Local collateral projections from the medial superior olive to the superior paraolivary nucleus in the gerbil. *Brain Res* 846:59–71.

Larkman AU (1991) Dendritic morphology of pyramidal neurones of the visual cortex of the rat: III. Spine distributions. *J Comp Neurol* 306:332–343.

Lay DM (1972) The anatomy, physiology, functional significance and evolution of specialized hearing organs of gerbilline rodents. *J Morphol* 138:41–120.

Lehnert S, Ford MC, Alexandrova O, Hellmundt F, Felmy F, Grothe B, Leibold C (2014) Action potential generation in an anatomically constrained model of medial superior olive axons. *J Neurosci* 34:5370–84.

Lesica NA, Lingner A, Grothe B (2010) Population coding of interaural time differences in gerbils and barn owls. *J Neurosci* 30:11696–11702.

Li W, Kaczmarek LK, Perney TM (2001) Localization of two high-threshold potassium channel subunits in the rat central auditory system. *J Comp Neurol* 437:196–218.

Lindsey BG (1975) Fine structure and distribution of axon terminals from cochlear nucleus on neurons in the medial superior olivary nucleus of the cat. *J Comp Neurol* 160:81–103.

Lohmann C, Ilic V, Friauf E (1998) Development of a topographically organized auditory network in slice culture is calcium dependent. *J Neurobiol* 34:97–112.

MacLeod KM, Soares D, Carr CE (2006) Interaural timing difference circuits in the auditory brainstem of the emu (Dromaius novaehollandiae). *J Comp Neurol* 495:185–201.

Magnusson AK, Kapfer C, Grothe B, Koch U (2005) Maturation of glycinergic inhibition in the gerbil medial superior olive after hearing onset. *J Physiol* 568:497–512.

Maki K, Furukawa S (2005) Acoustical cues for sound localization by the Mongolian gerbil, Meriones unguiculatus. *J Acoust Soc Am* 118:872–886.

Mathews PJ, Jercog PE, Rinzel J, Scott LL, Golding NL (2010) Control of submillisecond synaptic timing in binaural coincidence detectors by K(v)1 channels. *Nat Neurosci* 13:601–9.

McAlpine D, Jiang D, Shackleton TM, Palmer AR (1998) Convergent input from brainstem coincidence detectors onto delay-sensitive neurons in the inferior colliculus. *J Neurosci* 18:6026–39.

McAlpine D, Jiang D, Palmer AR (2001) A neural code for low-frequency sound localization in mammals. *Nat Neurosci* 4:396–401.

McGinley MJ, Liberman MC, Bal R, Oertel D (2012) Generating synchrony from the asynchronous: compensation for cochlear traveling wave delays by the dendrites of individual brainstem neurons. *J Neurosci* 32:9301–11.

Meeks JP, Mennerick S (2007) Action Potential Initiation and Propagation in CA3 Pyramidal Axons. *J Neurophysiol* 97:3460–3472.

Mendonça PRF, Kyle V, Yeo SH, Colledge WH, Robinson HPC (2018) Kv4.2 channel activity controls intrinsic firing dynamics of arcuate kisspeptin neurons. *J Physiol* 596:885–899.

Musicant AD, Chan JCK, Hind JE (1990) Direction-dependent spectral properties of cat external ear: New data and cross-species comparisons. *J Acoust Soc Am* 87:757–781.

Myoga MH, Lehnert S, Leibold C, Felmy F, Grothe B (2014) Glycinergic inhibition tunes coincidence detection in the auditory brainstem. *Nat Commun* 5:3790.

Nothwang HG (2016) Evolution of mammalian sound localization circuits: A developmental perspective. *Prog Neurobiol* 141:1–24.

Oertel D (1991) The role of intrinsic neuronal properties in the encoding of auditory information in the cochlear nuclei. *Curr Opin Neurobiol* 1:221–228.

Oertel D, Young ED (2004) What's a cerebellar circuit doing in the auditory system? *Trends Neurosci* 27:104–10.

Pecka M, Brand A, Behrend O, Grothe B (2008) Interaural time difference processing in the mammalian medial superior olive: the role of glycinergic inhibition. *J Neurosci* 28:6914–25.

Rautenberg PL (2012) Developmental alterations and electrophysiological properties: a morphological analysis of coincidence detector neurons in the medial superior olive Ph.D. diss., Ludwig-Maximilians-Universität München.

Rautenberg PL, Grothe B, Felmy F (2009) Quantification of the three-dimensional morphology of coincidence detector neurons in the medial superior olive of gerbils during late postnatal development. *J Comp Neurol* 517:385–96.

Rayleigh L (1907) On our perception of sound direction. *Philos Mag* 13:214–232.

Remme MWH, Donato R, Mikiel-Hunter J, Ballestero JA, Foster S, Rinzel J, McAlpine D (2014) Subthreshold resonance properties contribute to the efficient coding of auditory spatial cues. *P Natl Acad Sci USA* 111:E2339–E2348.

Rice JJ, May BJ, Spirou GA, Young ED (1992) Pinna-based spectral cues for sound localization in cat. *Hearing Res* 58:132–152.

Roberts M, Seeman S, Golding N (2013) A Mechanistic Understanding of the Role of Feedforward Inhibition in the Mammalian Sound Localization Circuitry. *Neuron* 78:923–935.

Rose JE, Gross NB, Geisler CD, Hind JE (1966) Some neural mechanisms in the inferior colliculus of the cat which may be relevant to localization of a sound source. *J Neurophysiol* 29:288–314.

Salling MC, Harrison NL (2014) Strychnine-sensitive glycine receptors on pyramidal neurons in layers II/III of the mouse prefrontal cortex are tonically activated. *J Neurophysiol* 112:1169–1178.

Schmid S, Guthmann A, Ruppersberg JP, Herbert H (2000) Expression of AMPA receptor subunit flip/flop splice variants in the rat auditory brainstem and inferior colliculus. *J Comp Neurol* 430:160–171.

Scott LL, Hage Ta, Golding NL (2007) Weak action potential backpropagation is associated with high-frequency axonal firing capability in principal neurons of the gerbil medial superior olive. *J Physiol* 583:647–61.

Scott LL, Mathews PJ, Golding NL (2005) Posthearing developmental refinement of temporal processing in principal neurons of the medial superior olive. *J Neurosci* 25:7887–95.

Scott LL, Mathews PJ, Golding NL (2010) Perisomatic voltage-gated sodium channels actively maintain linear synaptic integration in principal neurons of the medial superior olive. *J Neurosci* 30:2039–50.

Seidl AH, Rubel EW (2016) Systematic and differential myelination of axon collaterals in the mammalian auditory brainstem. *Glia* 64:487–494.

Siveke I, Pecka M, Seidl AH, Baudoux S, Grothe B (2006) Binaural Response Properties of Low-Frequency Neurons in the Gerbil Dorsal Nucleus of the Lateral Lemniscus. *J Neurophysiol* 96:1425–1440.

Smith AJ, Owens S, Forsythe ID (2000) Characterisation of inhibitory and excitatory postsynaptic currents of the rat medial superior olive. *J Physiol* 529:681–698.

Smith DJ, Rubel EW (1979) Organization and development of brain stem auditory nuclei of the chicken: Dendritic gradients in nucleus laminaris. *J Comp Neurol* 186:213–239.

Smith PH (1995) Structural and functional differences distinguish principal from nonprincipal cells in the guinea pig MSO slice. *J Neurophysiol* 73:1653–67.

Smith PH, Joris PX, Carney LH, Yin TCT (1991) Projections of physiologically characterized globular bushy cell axons from the cochlear nucleus of the cat. *J Comp Neurol* 304:387–407.

Smith PH, Joris PX, Yin TCT (1993) Projections of physiologically characterized spherical bushy cell axons from the cochlear nucleus of the cat: Evidence for delay lines to the medial superior olive. *J Comp Neurol* 331:245–260.

Spitzer MW, Semple MN (1995) Neurons sensitive to interaural phase disparity in gerbil superior olive: diverse monaural and temporal response properties. *J Neurophysiol* 73:1668–90.

Stange A, Myoga MH, Lingner A, Ford MC, Alexandrova O, Felmy F, Pecka M, Siveke I, Grothe B (2013) Adaptation in sound localization: from GABA(B) receptor-mediated synaptic modulation to perception. *Nat Neurosci* 16:1840–7.

Stange-Marten A, Nabel AL, Sinclair JL, Fischl M, Alexandrova O, Wohlfrom H, Kopp-Scheinpflug C, Pecka M, Grothe B (2017) Input timing for spatial processing is precisely tuned via constant synaptic delays and myelination patterns in the auditory brainstem. *P Natl Acad Sci USA* 114:E4851–E4858.

Stecker GC, Middlebrooks JC (2003) Distributed coding of sound locations in the auditory cortex. *Biol Cybern* 89:341–349.

Stotler WA (1953) An experimental study of the cells and connections of the superior olivary complex of the cat. *J Comp Neurol* 98:401–431.

Sullivan WE, Konishi M (1986) Neural map of interaural phase difference in the owl's brainstem. *P Natl Acad Sci USA* 83:8400–4.

van der Heijden M, Lorteije JAM, Plauška A, Roberts MT, Golding NL, Borst JGG (2013) Directional hearing by linear summation of binaural inputs at the medial superior olive. *Neuron* 78:936–48.

Webster DB, Plassman W (1992) Parallel evolution of low-frequency sensitivity in old world and new world rodents. In Webster DB, Popper AN, Fay RR, editors, *The Evolutionary Biology of Hearing*, chapter 30, pp. 633–636. Springer New York, New York, NY.

Werthat F, Alexandrova O, Grothe B, Koch U (2008) Experience-dependent refinement of the inhibitory axons projecting to the medial superior olive. *Dev Neurobiol* 68:1454–62.

Winters BD, Jin SX, Ledford KR, Golding NL (2017) Amplitude Normalization of Dendritic EPSPs at the Soma of Binaural Coincidence Detector Neurons of the Medial Superior Olive. *J Neurosci* 37:3138–3149.

Yin TC, Chan JC (1990) Interaural time sensitivity in medial superior olive of cat. *J Neurophysiol* 64:465–88.

Zhou YY, Carney LH, Colburn HS (2005) A model for interaural time difference sensitivity in the medial superior olive: interaction of excitatory and inhibitory synaptic inputs, channel dynamics, and cellular morphology. *J Neurosci* 25:3046–58.

Acknowledgements

Firstly I want to thank my supervisors: Felix, for welcoming me into his lab and supporting me in becoming an independent researcher, and Christian, for stepping in to supervise me and for taking the time to answer my many questions. Thank you also to Benedikt for insightful scientific advice in and out of TAC meetings, and also for providing, through the GSN, an invaluable scientific and social network. I also want to thank Lars and Conny for their feedback, suggestions and advice during TAC meetings.

Thank you to Alisha, Delwen, and Franzi, with whom I was very lucky to share an office. Thank you also to Julian and Sarah for helping me get started in the lab, and to the Felmy lab in Hannover for making me feel welcome when I visited. And thank you to my colleagues in the Neurobiology Department for all the entertaining lunches and tea breaks and for being a fantastic group of people to work with.

Thank you to Olga and Hilde for their crucial guidance in all things histological, to Mike for scientific advice, spontaneous lessons, and endless entertainment, as well as to Alex Loebel, a neverending source of advice on all matters.

Thank you to the GSN team for always being there to help with problems big and small.

Finally, I want to thank my family and friends, whose support was invaluable throughout my PhD. I couldn't have done it without you.

Eidesstattliche Versicherung
Affidavit

Hiermit versichere ich an Eides statt, dass ich die vorliegende Dissertation *Voltage signalling in the medial superior olive* selbstständig angefertigt habe, mich außer der angegebenen keiner weiteren Hilfsmittel bedient und alle Erkenntnisse, die aus dem Schrifttum ganz oder annähernd übernommen sind, als solche kenntlich gemacht und nach ihrer Herkunft unter Bezeichnung der Fundstelle einzeln nachgewiesen habe.

I hereby confirm that the dissertation *Voltage signalling in the medial superior olive* is the result of my own work and that I have only used sources or materials listed and specified in the dissertation.

München, den 7. März 2019
Munich, 7$^{\text{th}}$ March 2019

Alexander R. Callan